Generation of Supersaturated Total Dissolved Gas at Submerged Hydropower Low-level Outlets

by

Pengcheng Li

A thesis submitted in partial fulfillment of the requirements for the degree of

Doctor of Philosophy

in

Water Resources Engineering

Department of Civil and Environmental Engineering
University of Alberta

# Abstract

Supersaturation of total dissolved gasses (TDG) downstream of hydropower dams and their consequences for fish have been identified as one of the key potential impacts of hydropower operations on fish biodiversity and fishery productivity. It has been recorded that fish exposed to high TDG levels may suffer gas-bubble disease. The generation of high level TDG has been mostly studied downstream of spillways with very little attention to its generation related to low-level outlets, which is typically considered to be free from air entrainment and TDG issues. This research aims at developing prediction models that can have a full understanding of the processes of TDG generation at low-level outlets, including the mass transfer of rising bubbles, air demand of a hydraulic jump in a closed conduit with a submerged outlet, and the TDG generation of low-level outlets and its influencing factors.

Dissolution of gases from air bubbles to water (mass transfer from air bubbles to water) directly leads to the generation of TDG. To have a good understanding of bubble-water mass transfer, a model for bubble–water mass transfer was established and validated using the experimental measurements from rising carbon dioxide bubbles. The effects of bubble horizontal velocity, bubble release depth, initial bubble size, background dissolved gas concentration in the water, and bubble swarms on the bubble–water mass transfer were examined. The bubble size changed along the rising path in response to both the mass transfer and the local hydrostatic pressure, whereas their relative importance varied under different conditions. Compared with previous models, the proposed model improved the prediction accuracy by including the influence of changing dissolved gas concentration in the water and mass transfer across the water surface.

Air demand of a hydraulic jump in a closed conduit is the source of the dissolved gas and TDG

generation at low-level outlets. Physical experiments were conducted to study flow regimes and the air demand of a hydraulic jump in a closed conduit with various submerged outlet depths. Flow regimes with a submerged outlet were defined following previous studies based on the outlet depth. In a closed conduit, free surface supercritical flow without a hydraulic jump can induce a relative air demand (air flow rate to water flow rate) of about 36 - 90% when the Froude number is between 4 and 10, which decreases to about 3 - 14% for a free surface flow with a hydraulic jump. If the hydraulic jump is followed by pressurized pipe flow, the air demand decreases with the increasing submerged outlet depth. If the hydraulic jump is partially submerged, the relative air demand is significantly reduced to less than 1%. Field measurements of the air demand were consistent with the experimental measurements when the hydraulic jump was partially submerged. When the air supply was constrained by a nozzle of various sizes placed on the top of the air vent, the air pressure in the closed conduit deceased and the hydraulic jump moved upstream.

Supersaturated TDG was observed and evaluated through field measurements at Hugh Keenleyside Dam, B.C, Canada focusing on two groups of the low-level outlets (south and north low-level outlets). With an air entrainment amount of as small as 1%, a TDG level as high as 130% could be generated in the south low-level outlets. Numerical modelling was also adopted to obtain turbulence and flow field details downstream of the low-level outlets. Good agreement between model results and field data is found in the tailrace of the low-level outlet. Stronger turbulence in the stilling basin can result in larger mass transfer coefficient across bubbles and produce smaller bubbles, which will substantially enhance gas transfer and TDG generation. Due to the shallower water depth, the south low-level outlet can generate stronger turbulence flow, with more efficient gas transfer and TDG generation compared with the deeper north low-level outlet (110% TDG).

# Preface

This thesis is an original work by Pengcheng Li under the supervision from Dr. David Z. Zhu. This study is a part of a collaborative research project by Natural Sciences and Engineering Research Council of Canada (NSERC) and BC Hydro involving Carleton University, the University of Alberta, the University of Waterloo and the University of British Columbia. It is presented in a paper format and consists of six chapters.

Chapter 1 is a general introduction on the background, scope, and objectives of this study.

Chapter 2 is the literature review with special focuses on the fundamentals of the air entrainment and total dissolved gas generation.

Chapter 3 to 5 are the main contents of this thesis.

Chapter 3 was published as: Li, P., Ma, Y., and Zhu, D. Z. (2020). "Mass Transfer of Gas Bubble Rising in Stagnant Water." ASCE *Journal of Environmental Engineering*, 146(8), 10.1061/(ASCE)EE.1943-7870.0001760.

Chapter 4 has been submitted as a journal manuscript: Li, P., Zhu, D. Z., Xu, T., and Zhang, J. (2021). "Air Demand of a Hydraulic Jump in a Closed Conduit." ASCE *Journal of Hydraulic Engineering*, under review.

Chapter 5 is currently being prepared as a journal manuscript.

Chapter 6 contains the general conclusions of this thesis, and suggestions for the future research on total dissolved gas generation.

I was responsible for the experimental design, data collection and analysis as well as the manuscript composition. Dr. David Z. Zhu was the supervisory author and was involved with concept formation, data analysis and manuscript composition. Dr. Y. Ma assisted with the experimental design and contributed to manuscript edits of Chapter 3. Ms. T. Xu and Dr. J. Zhang assisted with the experimental design and data analysis of Chapter 4. Mr. A. Leake and Dr. J. Crossman facilitated data collection, provided recommendations in the hydropower operation, and contributed to manuscript edits of Chapter 6.

I also contributed the following publications:

Li, P., and Zhu, D. Z., Krywiak, D., and Yue, D. (2019). "Flow characteristics and energy dissipation of an offset jet in a rectangular stormwater pond", *Canadian Water Resources Journal*, 44(3). doi: 10.1080/07011784.2019.1623078.

Li, P., Zhang, W., Burnett, N. J., Zhu, D. Z., Casselman, M., and Hinch, S. G. (2021). "Evaluating dam water release strategies for migrating adult salmon using computational fluid dynamic modeling and biotelemetry." *Water Resources Research*. 57(8). doi: 10.1029/2020WR028981

Li, P., and Zhu, D. Z. (2018) "Field Study of Total Dissolved Gas Concentration Downstream of the Seven Mile Dam in British Columbia." *Proceedings of the World Environmental & Water Resources Congress*, Minneapolis, MN, the U.S.

Li, P., Ma, Y., and Zhu, D. Z. (2019). "Mass Transfer of a Single Oxygen-Bubble Rising in Stagnant Water." *Proceedings of the International Symposium on Sustainable Urban Drainage (SUD)*, Ningbo, China.

Ma, Y., Li, P., and Zhu, D. Z. (2019). "Air Flow inside a Vertical Pipe Induced by a Free-falling

Water Jet." *Proceedings of the International Symposium on Sustainable Urban Drainage (SUD)*, Ningbo, China.

*Dedicated to:*



*My dearest parents Mrs. Lizhen Wang and Mr. Guojie Li*



*Thanks for your unselfish love and unconditional support*

# Acknowledgements

# Table of Contents

# List of Tables

# List of Figures

# 1. General Introduction

## 1.1. Research Background

In Canada, approximately 60% of electricity generation is from hydroelectric sources. As such, this renewable energy source is incredibly important to all Canadians. In the meantime, the development of hydropower facilities greatly affects the morphology of regional water resources. Supersaturated total dissolved gasses (TDG) have been identified as one of the key potential impacts of hydropower operations on the biodiversity of fish. It has been recorded that fish exposed to supersaturated TDG may suffer gas-bubble disease (Ebel 1969; Beiningen et al. 1970; Dawley and Ebel 1975; Arntzen et al. 2009). The tolerance of supersaturated TDG for fish is relevant with water TDG saturation concentration, depth, exposure duration, water temperature and species of fish (Colt 1984; Weitkamp 2008; Smiley et al. 2011). Recognizing the harm to fish, the US Environmental Protection Agency (EPA) established a TDG criterion of 110 percent (USEPA 1986), but saturation percentage could reach as much as 140 percent downstream of many dams (Weitkamp and Katz 1980). The assessment and prediction of TDG at a plunge pool or stilling basin is an important issue for hydropower industry, as environmental regulations and approval requirements are becoming more stringent.

When flows pass through spillways, a large amount of atmospheric gases can be forced to be dissolved in the plunge pool and stilling basin as shown in Figure 1-1. In this case, air entrainment in water is an important factor for the generation of TDGs. If the partial pressure of these gases in water exceeds their atmospheric pressure, water becomes supersaturated with more than 100 percent of the atmospheric pressure saturation, which would cause gas bubble disease to fish (Figure 1-2). In a deeper region, the solubility increases and the air is transferred from bubbles into

water. The mass transfer rate from bubbles to ambient water is determined by bubble sizes, turbulent intensity, local pressure, etc. All these parameters depend on the operation conditions of hydraulics facilities and geometry of stilling basins. Therefore, understanding the process of TDG generation, including rising bubble mass transfer and air entrainment, is crucial for hydro-environmental perspective and habitat protection.

Mass transfer from gas bubbles to water is a key process in TDG generation, as well as in nature and industrial applications. For instance, artificial aeration is commonly used for water and wastewater treatment, as well as water quality improvement in lakes and reservoirs, by introducing air/oxygen bubbles into water using devices like a bubble-plume diffuser (McGinnis and Little 1998). Mass transfer from methane or carbon dioxide bubbles to water is also related to the amount of these greenhouse gases emitted from lakes, reservoirs, tailings ponds, etc., which has received increasing attention due to their significant contribution to global warming (St. Louis et al. 2000). Therefore, a good understanding of bubble-water mass transfer is important in a wide range of environmental issues and engineering applications.

Air demand of a hydraulic jump inside a closed conduit of a dam low-level outlet is the main source of air-bubble mass transfer and TDG generation in a stilling basin. Negative pressure, blowback, and other problems can be caused by entrained air in pipes or closed conduits in hydropower facilities. Air entrainment and transport are also important in municipal engineering applications as in ventilation and sewer odor related issues (Edwini-Bonsu and Steffler, 2004; Qian et al. 2021). Thus, it is crucial to predict the air demand in a closed conduit under different outlet conditions to ensure proper design and operations of these hydraulic structures.

The generation of high level TDG has been mostly studied downstream of spillways with very

little attention given to its generation related to submerged low-level outlets, which are typically considered to be free from air entrainment and TDG issues. In this study, supersaturated TDG was observed at Hugh Keenleyside Dam, B.C, Canada focusing on two groups of low-level outlets. Typically, deeper bubbles in a stilling basin experience higher hydrostatic pressure and thus more air is forced into solution. However, the dam frequently generates higher TDG in the shallower low-level outlets than that generated in the deeper low-level outlets (Kamal et al. 2019). Previous studies lack the understanding and prediction of such phenomenon, which has been investigated in this research.

## 1.2. Thesis Outline

The structure of this thesis is organized as follows:

Chapter 2 is a comprehensive literature review on the physical mechanisms of bubble movement and mass transfer, air demand and entrainment of a hydraulic jump, and TDG prediction at hydropower facilities. The knowledge gaps are identified.

Chapter 3 presents an analytical and experimental study on mass transfer from a single bubble rising in stagnant water and its size variation, including the effects of bubble horizontal velocity, bubble release depth, initial bubble size, background dissolved gas concentration in the water, and bubble swarms on the bubble-water mass transfer.

Chapter 4 investigates flow regimes and air demand of a hydraulic jump in a closed conduit with various submerged outlet depths. The dynamics of the air pocket upstream of the hydraulic jump and characteristics of the hydraulic jump with limited air supply under a submerged outlet are also studied.

Chapter 5 proposes a physically based model for TDG generation at submerged low-level outlets, which is calibrated and validated with a series of field measurements, to investigate various influencing factors. The mechanisms of TDG generation at low-level outlets, and the source and amount of the air entrainment in the low-level outlet are also investigated.

Chapter 7 concludes the thesis and discusses the future directions of this research.
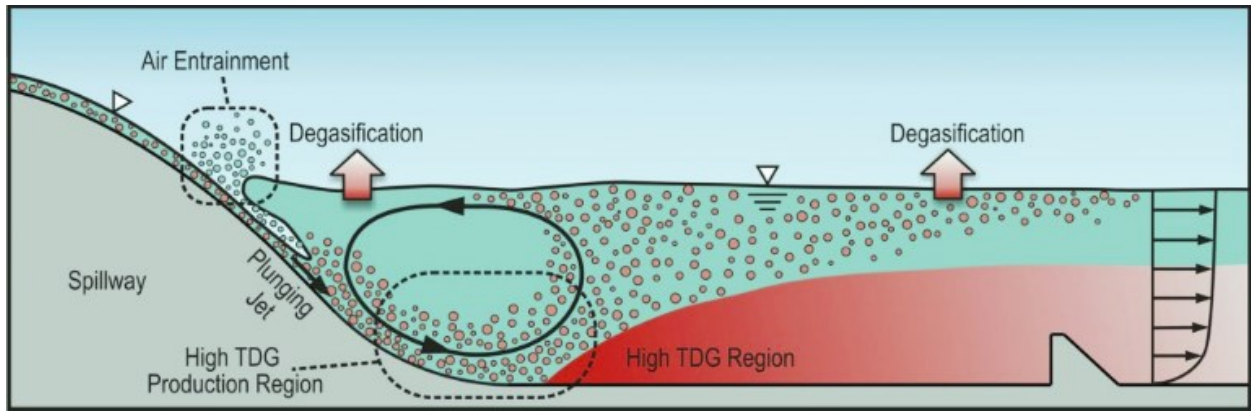
Figure 1-1 Gas transfer process downstream of a spillway

(from http://www.iihr.uiowa.edu/totaldissolvedgas/)

Figure 1-2 Bulging eyes due to bubble formation caused by supersaturation

(https://pentairaes.com/media/docs/Point-Four-Tracker-PortableTGP-Meter-Manual)

# 2. Literature Review

During spillway discharge events, a large amount of atmospheric gases can be entrained and dissolved in the plunge pools and stilling basins. The generated TDG level is therefore determined by the amount of entrained air, and the efficiency of air-bubble dissolution (e.g. bubble size, residence time, water depth, etc.). Air can also be entrained into flowing water through turbulent shear layers generated by hydraulic jumps at the air-water interface, which may impact gas transfer (Hager 2010, Colt 2012). The process of air-water mass transfer is that air molecules diffuse to water driven by a concentration difference. As water depth increases, air solubility increases due to the higher ambient pressure, and more air bubbles are dissolved into water. The mass transfer rate from bubble to water is affected by bubble size, turbulent intensity, pressure, etc. (Politano et al. 2009). All of these parameters are influenced by the operating conditions of hydropower facilities and geometry of stilling basins. This chapter provides a comprehensive review on TDG generation process, including the physical process of air entrainment, air demand in a closed conduit, mass transfer and movement of air bubbles, and TDG predictions.

## 2.1. Gas Dissolution and Mass Transfer of Air Bubbles

The sources of dissolved gases are from the atmosphere which involves oxygen, nitrogen, argon, and carbon dioxide, and total dissolved gases (TDG) in water represents the summation of these different gas components dissolved in water. Typically, TDG concentration is represented by the ratio of total gas pressure (TGP) to the local barometric pressure (BP). TGP is the absolute pressure of the sum of the partial pressures plus water vapor. TDG can be calculated in a percent of local barometric pressure:

$$TDG(\%) = \frac{TGP}{BP} \times 100\% \quad (2-1)$$

Three conditions could occur for TDG (%) concentration: when TDG (%) is less than 100%, the water is undersaturated; when TDG (%) is 100%, the TDG in water is equilibrium; when TDG (%) is larger than 100%, the water is supersaturated (Colt 2012). Additionally, the percentage of TDG can also be calculated as an absolute concentration (mg/L):

$$TDG(\%) = \frac{C}{C_s} \times 100\% \quad (2-2)$$

where $C$ = dissolved gas concentration(mg/L) in water, and $C_s$ = liquid-phase equilibrium concentration (mg/L) of the air at the local atmospheric pressure (air saturation concentration), which can be calculated by Henry's law (Gulliver et al. 1997). When TDG concentration ($C$) is more than $C_s$, the water is supersaturated.

Mass transfer between air bubbles and water is typically characterized by a first-order process where its rate is determined by the bubble-water interfacial area, bubble residence time, mass transfer coefficient, and the difference between the local concentration of the gas and its effective saturation concentration (Gulliver et al. 1997). The rate of mass transfer can be written as

$$dC/dt = -K_L a(C_{se} - C) \quad (2-3)$$

where $t$ = the time over which mass transfer takes place (s), $K_L$ = mass transfer coefficient (m/s), $a$ = the specific bubble-water interfacial area and $C_{se}$ is the effective saturation concentration (mg/L). The concentration difference between bubbles ($C_{se}$) and water ($C$) drives mass transfer across bubble-water interface. According to Henry's law, the effective saturation concentration ($C_{se}$) of the air in water is directly proportional to the partial pressure of air. Thus, $C_{se}$ increases

with water depth, and the mass transfer flux is larger in deeper water.

Gulliver et al. (1990) proposed a method for estimating the effective depth ($H_{eff}$), which is the depth in stilling basin/plunge pool that the hydrostatic pressure acting on bubbles can bring them into equilibrium with the saturation concentration. In the continuous study, Gulliver et al. (1997) found that the effective saturation concentration increases with bubble penetration depth and they developed an equation for determining $C_{se}$:

$$C_{se} = C_s \left( 1 + \frac{H_{eff}\gamma}{P_{atm}} \right) \quad (2-4)$$

where $P_{atm}$ is the local atmospheric pressure (Pa). Based on field measurements, the approximation of the effective depth $H_{eff}$ is estimated to be 2/3 of the bubble penetration depth by assuming a triangular-shaped bubble swarm (Johnson and King 1975). An empirical equation for the bubble penetration depth was developed by Hibbs and Gulliver (1997):

$$\frac{1}{\left(\frac{H_{eff}}{H}\right)} = \frac{1}{\alpha_1 \left(\frac{H_p}{H}\right)} + \frac{1}{\left(\frac{H_{eff}}{H}\right)_{max}} \quad (2-5)$$

where $(H_{eff}/H)_{max} = 2/3$, $H_p$ is the maximum bubble penetration depth, and $\alpha_1$ is the fraction of the distance from the water surface to the centroid of the bubble swarm and is approximately 0.32 based on an empirical fit of field observations. When the value for the maximum plunging depth of a bubble is greater than the stilling basin depth the effective depth approaches 2/3 of the water depth.

The impact of temperature on mass transfer is nonlinear and quite gas specific, especially for noble gases (Colt 2012). The air solubility decreases with increasing water temperature when pressure is

constant. In this case, the TDG would be supersaturated when water temperature increased due to the decreasing solubility. In addition to the pressure and temperature in stilling basin, some other factors would also influent gas supersaturation such as initial air saturation concentration, residence time, and air entrainment concentration, etc. Qu et al. (2011) did some experiments with a water column and found that pressure (water depth), aeration intensity, and bubble dissolution time are important factors that would affect the supersaturated TDG generation.

## 2.2. Physical Process of Air Entrainment

As pointed out by Ervine et al. (1980), air entrainment would happen if the turbulence level can overcome surface tension and buoyancy effects. The significant turbulent level can cause free-surface aeration downstream of the inception point (the location where turbulent boundary layer reaches the free surface), where the white water occurs and just downstream of the smooth free surface (Chanson 1995; Wood 1997). The physical process of free surface aeration along the spillway and entrained air bubble transportation are shown in Figure 2-1.

The air entrainment process along a spillway could be divided into three parts based on the mechanism or process: pre-entrainment, air boundary layer entrainment, and trumpet suction (Huang 2002). Typically, the free surface of the upstream in the spill flow appears smooth. However, the boundary layer grows thicker along the spillway, and air entrainment happens when the inception point occurs where the boundary layer reaches the free surface. This is a non-aerated developing flow region or pre-entrainment region. Downstream of the inception point or pre-entrainment region, the turbulence is larger enough to induce free-surface aeration. Along the spill flow surface, the contacted air can be dragged into movement, which composes an air boundary layer. Some of the air will eventually be released along the surface, whereas the rest will be trapped

into the water in the stilling basin. This is air boundary layer entrainment or self-aerated air entrainment.

Chanson (1993a, 1995, 2007) measured the entrained air concentration distribution, air bubble size and distribution, water velocity profile, fluctuation characteristics of the free surface, turbulent characteristic length and time along with self-aerated open channel flow with a small slope, and proposed an equation for entrained air concentration distribution. Additionally, Chanson (1993b, 2003) studied the effects of flow velocity, energy dissipation rate and channel roughness on air concentration along stepped spillways, and analyzed the characteristics of flow turbulence and free surface fluctuation. When the spill jet plunges into the stilling basin, the air entrainment will be caused by the backflow waves and the upcoming high speed spill flow, which is called trumped suction. The whole process of air entrainment in spillway or free surface flows can also be classified into two basic types, one is local or singular aeration and the other is interfacial aeration as shown in Figure 2-2 (Chanson 2004).

Along the spillway, the strong shear force will reduce or break the entrained bubbles into smaller sizes, which is the turbulent shear region (Rajaratnam 1976). Due to the high buoyancy force, these entrained small air bubbles will rise upward and merge into larger size bubbles. In the meantime, strong backflows and turbulent eddies occur. This region is called boiling region. Around the surface of stilling basin, amounts of air bubbles form a foam region, where some entrained air bubbles and dissolved gas escape into the atmosphere (Chanson and Cummings 1992). In this case, mass transfer from air bubbles into water mainly occurs in the lower part of boiling region and turbulent shear region. And the air volume fraction will be smaller around the water surface than deeper part of the water. Orlins and Gulliver (2000) demonstrated that the probability of entrained air bubbles can be approximated by an exponential equation, and the probability of bubble could

be regarded as air volume fraction in a specific position.

Sene (1988) and Geldert et al. (1998) made an assumption that there is no air entrainment on the spillway face and suggested a simple relation for the specific air discharge ($q_a = V_j \lambda$), and entrained air concentration or initial air volume fraction($\alpha_a$) could be estimated as:

$$\alpha_a = \frac{q_a}{q_a + q} = \frac{V_j \lambda}{V_j \lambda + q} \quad (2-6)$$

where $q_a$ and $q$ are the specific air discharge and water discharge respectively; $V_j$ is the velocity of the jet; $\lambda$ is an air layer thickness, which can be determined by fitting of predicted and measured TDG value downstream. Note that the pre-aeration (air entrainment on spillway face) typically occurred in spill event, which cannot be neglected in some cases. Therefore, Eq. (2-6) might underestimate the entrained air volume fraction. As Chanson et al. (2004) proposed that scale issue has obvious effects on air entrainment and bubble dispersion, the previous measurement data could not be directly used in other studies with different scales. In the last decade, TDG was predicted by applying numerical model, the air demand and bubble sizes were calculated as a fitting number through the measured data (Dvorak 2013; Politano et al. 2008, 2009, 2011, 2014). Due to the complexity of air-water flow along spillway and plunging point, measurements and estimation of gas volume fraction and bubble size in a spillway of a dam at a prototype scale are very difficult.

Chanson (1996) found that the interaction between air bubbles and turbulent shear layers has little influence on mean velocity distribution, and he proposed that air and water flow is a homogeneous bubbly flow mixture. This provides an important conception for the numerical model, in other words, the continuity, momentum, and energy equations could be applied as the homogenous mixture for a control volume.

## 2.3. Air Demand in a Closed Conduit

Air can be entrained into flowing water by a hydraulic jump in a closed conduit. Hydraulic jumps have different flow regimes in a closed conduit or pipe. Sharma (1976) identified six types of flow regimes in the low-level outlet (spray flow, free flow, foamy flow, hydraulic jump followed by free-surface flow or pressurized flow, and fully pressurized flow) as a function of the inlet and the downstream boundary conditions, which are shown in Figure 2-3. Stahl and Hager (1999) identified four different types of hydraulic jumps (undular hydraulic jump, direct hydraulic jump, hydraulic jump with a flow recirculation, and hydraulic jump with a transition to pressurized pipe flow) based on the approach Froude number and gate opening. However, hydraulic jump followed by pressurized pipe flow was not studied. Hager (2010) also distinguished six regimes for horizontal gas-liquid flow without a hydraulic jump, such as slug flow, bubbly flow, etc. The flow conditions and hydraulic jump types have been widely discussed in a closed conduit or pipe, limited attention has been devoted to flow regimes of a hydraulic jump in a closed conduit with various submerged outlet depths.

Modeling the airflow induced by subcritical flows in a single pipe has been extensively studied for the past 40 years (Pescod and Price, 1982; Park and Ryan 2001; Bentzen et al. 2016;  Qian et al. 2020). Air entrainment in a closed conduit with supercritical flow with or without a hydraulic jump has also been widely investigated. Wunderlich (1963) proposed air demand from the air velocity profile above the mixture surface in a free-surface flow. The US Army Corps of Engineers (1964) proposed an equation for calculating air demand for supercritical free surface flow based on prototypes from several dams. Wisner (1967) and Sharma (1976) proposed prediction equations of air demand for supercritical free-surface flow through experimental measurements and they

found that air demand was dependent on the Froude number.

Kalinske and Robertson (1943) conducted some very first experiments of air entrainment of hydraulic jumps and showed that regardless of pipe length and slope, air demand was only determined by the Froude number upstream of the jump. Rajaratnam (1967) proposed that the air entrainment of the hydraulic jump was mainly from the drag of the surface of the supercritical flow and turbulent mixing generated by the hydraulic jump. Sharma (1976), Wisner et al. (1975) and Rabben et al. (1983) also developed air demand relationships for hydraulic jumps in different cross-sectional geometries, which suggested that air demand in rectangular and circular pipes was quite different. There were some large differences between various experiments as outlined by Escarameia (2007), who indicated different cross-sections and the downstream outlet conditions can substantially affect air demand, but the detailed analysis was not conducted. Tullis and Lachar (2011) and Wright and Tullis (2014) extensively studied the air demand of low-level outlets for small- to medium-sized dams. However, the effects of the outlet conditions on air demand were not systematically assessed. Mortensen et al. (2012) investigated the influence of hydraulic jump location within closed conduits on air demand. It was found that the air demand would increase when the roller length of the hydraulic jump was truncated. Recently, Hohermuth et al. (2020) proposed that the air vent characteristic, such as the air vent loss coefficient and diameter, can influence the air demand in the closed conduit with a free surface outlet.

Though hydraulic jump characteristics and air entrainment prediction within closed conduits have been studied in the literature (Falvey 1980; Chanson 1996; Unsal et al. 2008; Vos 2011; Ozkan et al. 2014), no specific attention has been paid to the effects of flow regimes with a submerged outlet. Therefore, the submergence influences on hydraulic jump characteristics and air entrainment need to be investigated.

## 2.4. Total Dissolved Gas Prediction

In order to protect water environment, it is necessary to calculate or predict TDG value downstream of dams under different operational conditions. According to previous studies, air bubbles are responsible for more than 95% of the mass transfer (Nakasone 1987; Gulliver et al. 1997). The coalescence, breakup, and rise of bubbles in turbulent flow would make it difficult to forecast the size and flow pattern of entrained bubbles, which would also affect the accuracy of predicting the mass transfer rate between air bubbles and water.

At present, there are two main models for predicting TDG downstream of dams. One approach to predicting TDG was based on laboratory/field works and data fitting (Klohn-Crippen Integ 1994; Bruce and Plate 2013). Although these models are reasonably effective, the physical process and mechanism of TDG generation are not analyzed. Additionally, laboratory models could not reproduce turbulence, temperature, and TDG due to much smaller model scale. Overall, this approach neither reflects the mechanism of TDG generation nor provides a quantifiable prediction.

The other model is based on mechanism and physical process of TDG generation, it physically describes gas transfer downstream of the spillway and has been developed to quantitatively predict TDG. Roesner and Norton (1971) proposed an early analytical model for predicting TDG, the equation is:

$$C_d = C_{se} - (C_{se} - C_u) \exp(-K_L t) \quad (2-7)$$

where $C_d$, $C_u$, and $C_{se}$ are downstream TDG concentration, upstream TDG concentration, $K_L$ is mass transfer coefficient, $t$ is bubble residence time in the stilling basin. However, this model highly relied on the field data and could not reflect the influence of flow conditions. Roesner and

Norton defined 2/3 of tailwater depth as effective depth to calculate effective saturation concentration. Johnson and King (1975) improved $K_L$ and $t$ based on field data.

Typically, air bubble mass transfer is the predominant process of TDG generation in a stilling basin, which can be illustrated in the predictive equations as $(K_La)_{bubble}$. However, bubbles that remain in water can rise to the free surface where most of the mass transfer takes place across the water surface (mass of dissolved gases in water is transferred to the atmosphere). This gives rise to the importance of free surface mass transfer $(K_La)_{surface}$. In this case, Geldert et al. (1998) and Orlins and Gulliver (2000) made an important improvement on Roesner and Norton's model by incorporating the mass transfer in both gas bubbles and water free surface, the predicting equation is shown below:

$$\frac{dC}{dt} = (K_La)_{bubble}(C_{se} - C) + (K_La)_{surface}(C_s - C) \quad (2-8)$$

where $(K_La)_{bubble}$ is the transfer rate coefficient $(t^{-1})$ across the bubble interface; $(K_La)_{surface}$ is the transfer rate coefficient $(t^{-1})$ across the water surface, $K$ and $a$ are calculated separately in later studies (Ma et al. 2016; Politano et al. 2009); Roesner and Norton (1971) and later models defined effective depth as two-thirds of the tailwater depth. This value is based on the triangular geometry formed by the bubble distribution in a stilling basin, which was assumed that the jet penetrated to the bottom of stilling basin and spread to the whole basin before the tail end of the basin. The centroid of this triangular was regarded as the effective depth. However, this model can only be used on some specific spillways and highly depended on field data.

US Army Corps of Engineers proposed the TDG mechanistic models based on the physical process of spilling water and dissolving TDG in the tailrace (Anderson et al. 2000). The mechanistic model

with TDG concentration is:

$$G_{sb} = G_{eq} \cdot \bar{P} - \left(G_{eq} \cdot \bar{P} - G_{fb}\right) \cdot \exp\left(-\frac{K_e}{Q_s} WL\Delta\right) \quad (2-9)$$

where $Q_s$ = spill flow in kcfs; $G_{sb}$ = TDG concentration exiting the stilling basin in mg/l; $G_{fb}$ = TDG concentration in the forebay in mg/l; $G_{eq}$ = TDG equilibrium concentration as a function of temperature at one atmosphere of pressure; $\bar{P}$ = average hydrostatic pressure in the stilling basin; $K_e$ = bubble entrainment coefficient; $W$ = spillway width; $L$ = length of stilling basin; $\Delta$ = differential pressure factor. However, this model relies on temperature for calculating TDG equilibrium concentration and does not show good prediction in other facilities (Kamal et al. 2017).

Li et al. (2009) proposed a prediction model for supersaturated total dissolved gas in high dams based on the USACE's model. They developed two TDG prediction models for the scour hole and the plunge pool with the method of theoretical analysis and field observation. The model is similar to that of USACE but with the unit of percentage rather than concentration of TDG. Following Li et al. (2009), Qu et al. (2011) and Ma et al. (2016) simulated supersaturated TDG in plunge pools of high dams with a consideration of different bubble size distributions. However, these models require the correction factor which will be variant with different hydraulic facilities.

Except for TDG generation, degasification in a ski-jump spillway was also observed by Kamal et al. (2020). In their study, gas transfer in the spillway face, free jet, and plunge pool were tested separately through a simplified mathematical formulation. Additionally, it has been found that the dissipation rate of TDG is very small and can be neglected in predicting TDG generation (Kamal et al. 2019; Wang et al. 2019). As the development of computational fluid mechanics (CFD) model, TDG prediction model developed by using numerical method was then widely applied. There are

two basic classifications of numerical approach on air bubbles dynamic studies, they are microscopic and macroscopic models (Harlow 1985). The microscopic approach is modeling detailed interaction between air bubbles and water, and interface tracking of different fluids. The macroscopic approach simulates the average properties and regards air bubbles and water as a mixture, which is a simplified and computational low-cost model compared to microscopic model, but does not calculate specific information of individual air bubbles. Macroscopic model has the robust ability for predicting TDG since the detailed information of individual bubbles is not important and it is not time-consuming for numerical calculation (Deen et al. 2004). Orlins and Gulliver (2000) developed a forecasting model to estimate depth-averaged TDG generation and transport downstream Wanapum Dam in the Columbia River based on hydrodynamic data and air bubble distribution from the physical model. This model is based on a two-dimensional, laterally averaged mass transport equation, which accounts for convection, turbulent diffusion, and mass transfer across interfaces. However, the reduced-scale physical model cannot simulate air entrainment and mass transfer, and it is a limitation to rely on physical model and field data.

Weber et al. (2004) improved the model into three-dimensional and predict TDG generation and transport downstream of the spillway. They applied two-equation $k$-$\varepsilon$ turbulence model to predict hydrodynamics, which could decrease the reliance on experimental/field data. Convection-diffusion transport equation was applied in the model, and the source term considered the mass transfer between bubble-water and atmosphere-water. Additionally, the TDG production parameter and the surface exchange parameter were calibrated and fitted measurements. Results showed good prediction downstream of Wanapum Dam and Hell's Canyon Dam.

Urban et al. (2008) developed a more robust TDG prediction model and specified three flow regions downstream a spillway: the plunging and expanding jet region, return roller region, and

tailwater region. Different governing equations were applied to these regions to calculate turbulent kinetic energy, water velocity, air volume fraction, air bubble size and velocity. Therefore, effective saturation concentration and mass transfer coefficient could be calculated and the TDG in each region would also be predicted, the results showed good agreement with field data. However, bubble distribution was still based on empirical correlation, the authors noted that TDG downstream spillway is minimally dependent on entrained air on the spillway face.

In order to predict hydrodynamics and TDG distribution in tailrace and stilling basins, Politano et al. (2007) developed a 2D modified two-phase $k$-$\varepsilon$ turbulence model to predict TDG concentration downstream a spillway with a bubble/liquid mass transfer equation involving the gas volume fraction and bubble size. The authors used bubble number density transport equation to predict bubble size variation due to mass transfer and pressure change. They also divided bubbles into different groups according to their diameter, and the mass transfer was calculated in each group separately. This model has shown good agreement with field data for TDG concentration measured downstream Wanapum Dam on Columbia River. However, the effects of bubbles on the flow field (one-way coupling), such as bubble breakup and coalescence, were neglected.

The limitation of the above model was discussed in Politano et al. (2009). They build a two-phase two-way coupling TDG prediction model assuming the entrainment air volume fraction and bubble size distribution are known before running the model. This model focused on air-water mass transfer and transport process in the stilling basin/tailrace considering bubble size change based on bubble number density equation proposed in their study. In their study, a rigid lid approach enforcing zero normal fluctuation is implemented in the water free surface. Although this method has proved to be good in predicting TDG distribution in engineering applications, it only could be applicable for the moderate or mild free surface. Typically, the free surface downstream of a

spillway is complex and unsteady, and the tailrace flow field is highly dynamic and turbulent. Despite the disadvantages, the model provides a good base for TDG generation and transportation simulation, such as optimizing operational strategies to minimize TDG (Politano et al. 2012) and designing spillway deflectors (Politano et al. 2014). The deflector would force the spillway jet horizontally which would change the plunging flow into a skimming flow, preventing spillway flow from plunging deep into the stilling basin and reduce supersaturated TDG generation (Nielsen et al. 2000; USACE 2005).

## 2.5. Knowledge Gaps

In general, knowledge gaps about a rising bubble mass transfer, air demand in a closed conduit, and TDG generations of low-level outlets were identified as follows:

1). Bubble size variation along a bubble rising trajectory was seldom discussed in the previous studies, which can significantly affect the bubble-water mass transfer process; mass transfer from dissolved nitrogen and dissolved oxygen to the gas bubble along its rising trajectory needs to be considered;

2). While the characteristics of a hydraulic jump and the air entrainment prediction within closed conduits or sewer systems have been studied, the knowledge on air flow demand under various submerged outlet depths is still limited;

3). TDG generation from the submerged low-level gate or close conduit has rarely been studied; field measurements need to be conducted downstream of low-level outlets for model development and calibration; previous studies lack the understanding of higher level TDG is generated with shallower water depth in the low-level outlets; impacts of turbulence on bubble size and TDG

generation need to be investigated.
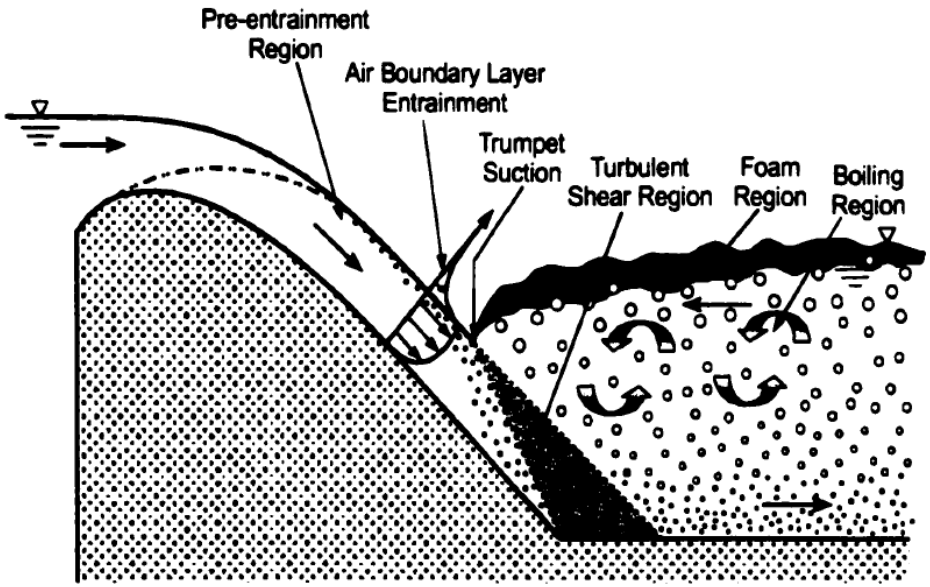
Figure 2-1 Air entrainment along a spillway and stilling basin (Huang 2002)
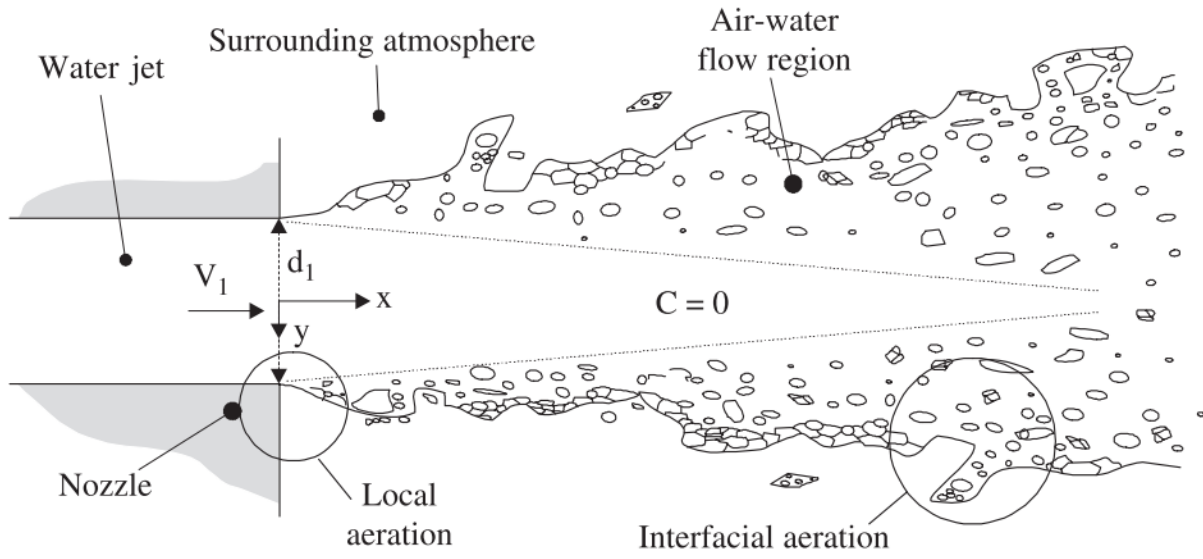
Figure 2-2 Sketch of basic free-surface aeration processes (Chanson 2004)
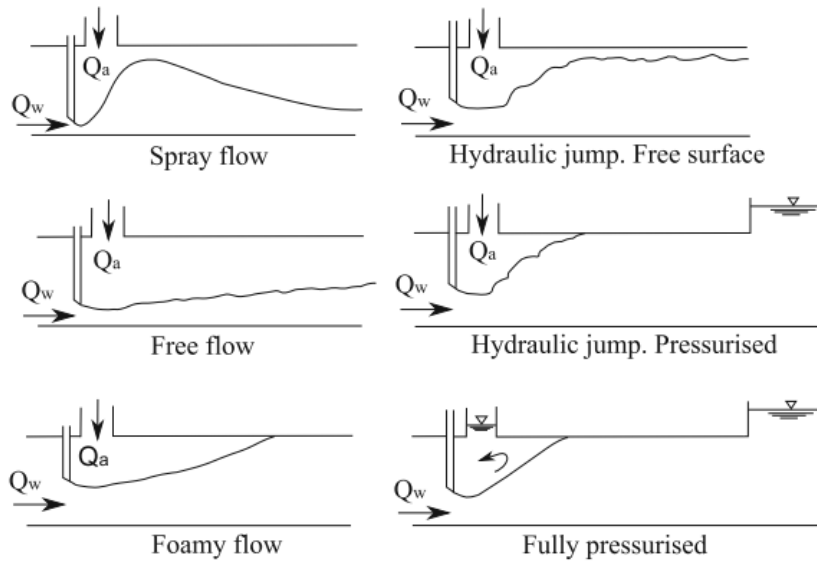
Figure 2-3 Type of flow regimes in gated conduits (Sharma 1976)

# 3. Mass Transfer of Gas Bubbles Rising in Stagnant Water[*]

## 3.1. Introduction

Mass transfer from gas bubbles to a liquid is an important process in nature and industrial applications. For instance, artificial aeration is commonly used for water and wastewater treatment, as well as water quality improvement in lakes and reservoirs, by introducing air/oxygen bubbles into water using devices like bubble-plume diffuser, the Speece Cone, etc. (McGinnis and Little 1998, Huang et al. 2009). In this case, mass transfer during the aeration process improves the dissolved oxygen level and the water quality (Khan et al. 2011, Tzvi and Paz 2019). Mass transfer from methane or carbon dioxide bubbles to water is also related to the amount of these greenhouse gases emitted from lakes, reservoirs, tailings pond, etc., which has received increasing attention due to their significant contribution to global warming (St. Louis et al. 2000). Additionally, mass transfer from air bubbles entrained by spilled water at hydroelectric projects can lead to high-level total dissolved gas concentration, and cause gas bubble disease in fish (Weitkamp and Katz 1980). Therefore, a good understanding of bubble-water mass transfer is important in a wide range of environmental issues and engineering applications.

It is commonly recognized that the mass transfer between a bubble and water is determined by the bubble-water interfacial area, bubble residence time, mass transfer coefficient and gas concentration difference. The rate of mass transfer can be written as $dM/dt = -K_L A(C_s - C)$,

where $M$ = mass of the gas inside the bubble; $t$ = time, $K_L$ = mass transfer coefficient, $A$ = bubble-water interfacial area, $C$ = dissolved gas concentration in water, and $C_s$ = liquid-phase equilibrium concentration under the local partial pressure of the gas, which can be calculated by Henry's law (Gulliver et al. 1997). The mass transfer rate of a rising bubble in water varies with bubble size and rising velocity, which was observed from experimental measurements (Schulze and Schlünder 1985). The bubble terminal velocity is determined by the balance of buoyancy force and drag force, and usually calculated using drag equation (Maneri and Vassallo 2000). Bubble size is another important parameter in the mass transfer process, because it determines the bubble-water interfacial area, mass transfer coefficient and bubble rising velocity (Alves et al. 2005). Mass transfer rate, in turn, can also affect bubble sizes. Therefore, the two-way coupled interaction between bubble size and mass transfer needs to be considered in predicting mass transfer across the bubble-water interface.

Extensive experimental studies have been conducted on mass transfer of a single bubble rising in water columns, including those for carbon dioxide bubbles (Takemura and Yabe 1999; Hanyu and Saito 2010) and oxygen bubbles (Francois et al. 2011; Jimenez et al. 2014), with the bubble diameter ranging from 0.1 to 10 mm. Following early work of Epstein and Plesset (1950), a number of studies improved the prediction model of mass transfer from bubbles to water (Takemura and Yabe, 1999; McGinnis et al. 2002; Singleton et al. 2007). The main differences among these models are the methods for calculating mass transfer coefficient, bubble velocity, diffusivity, etc. However, these models were only applicable for a single bubble rising in the water with a constant background dissolved gas concentration, which are not suitable for predicting continuous bubble dissolution with changing dissolved gas concentration in the water. Furthermore, bubble size variation along a bubble rising trajectory was seldom discussed in the previous studies, which can

significantly affect the bubble-water mass transfer process (Nock et al. 2016; Wang et al. 2019). Additionally, although the mass transfer at the water free-surface can change the background dissolved gas concentration, it has been typically ignored in the previous studies, e.g. McGinnis and Little (2002). Schierholz et al. (2006) developed two empirical characterization equations for bubble and surface volumetric mass transfer coefficient. However, the method was applied to bubble plumes without considering the mass transfer coefficient and bubble-water interfacial area of the single bubble.

In this paper, a model for mass transfer from a single bubble rising in stagnant water was established which includes the effects of changing bubble size and background dissolved gas concentration, mass transfer from dissolved nitrogen and oxygen in the water, and mass transfer at the water surface. Experimental measurements from a rising carbon dioxide gas bubble were conducted to validate the model predictions. Bubble size variation and mass transfer efficiency along the bubble rising path were investigated with the model under different conditions of bubble release depth, initial bubble diameter and dissolved gas concentration in the water. The applicability of the model for predicting the mass transfer of continuously injected bubble swarms in deep water, as well as bubble dissolution, were also verified. The effect of air bubble flow rate, water depth and bubble size on the mass transfer from continuously injected bubbles to the water was then analyzed.

## 3.2. Experimental Program

The experiments of bubble movement and mass transfer with injected $CO_2$ bubbles were conducted in the T. Blench Hydraulic Lab at the University of Alberta. The experimental setup consisted of a Perspex square tank of 0.4 m × 0.4 m × 0.4 m, a gas cylinder filled with pure carbon dioxide,

and a pressure regulator, as shown in Figure 3-1. The tank was covered at the top and filled with untreated tap water with gas bubbles released from the bottom of the tank. To obtain an evident size change of the rising bubble in such a small-scale setup, pure carbon dioxide gas was used for the experiments. The pressurized pure $CO_2$ was stored in a gas cylinder and adjusted by a pressure regulator and a valve. During the experiments, the pressure regulator was always kept at 25 $kPa$, and the bubble injection frequency was controlled by adjusting the valve. Nozzles of 0.90 mm and 2.55 mm diameter were used to produce different bubble sizes. Bubbles were injected continuously from the nozzle located 3 cm above the base of the tank, which had a bubble release depth of 0.3 - 0.35 m.

The pH of the untreated tap water used in the experiments was around 7.4. The concentration of the total dissolved gases (TDG) of the water was measured before the experiments by PT4 Smart TGP probe (Pentair Aquatic Eco-System, Apopka, Florida). It was 100% - 101%, which indicated that the water was fully saturated with air. The water temperature was kept about 22 °C during the experiments. The $CO_2$ gas was injected at a bubble number flux $F = 28$ - 105 per minute, with the initial diameter ranging between 3.0 and 3.8 mm. The corresponding gas flow rate was 0.396 - 3.017 mL/min. The injected $CO_2$ gas bubbles rose through the water column and eventually released into the tank headspace, which was filled with the ambient air initially with a $CO_2$ concentration of 0.95 – 1.09 mg/L. The intial gas in the tank headspace was sampled with a syringe and the $CO_2$ concentration was measured using Gas Chromatograph (GC-TCD/ECD, Agilent Technologies 7890B GC System). Note that the unit of gas concentration used in this study is *mg/L*, which can be converted to *ppm* (parts per million) using the relationship: 1 ppm = $\rho_g$/1000 (mg/L), where the unit of $\rho_g$ is in kg/m$^3$.

A vent tube was placed on the top of the tank to equalize the air pressure, which could lead to a

small amount of gas exchange and dilute the concentration of $CO_2$ in the tank headspace. The chamber and measurement method used in this study were similar to those in Longdoz et al. (2000) and, where the error due to $CO_2$ leakage was reported to be less than 3% of the mean flux. Therefore, the $CO_2$ leakage was neglected here.

The motion and size change of the rising bubble were recorded by a high-speed camera (Phantom v211, Vision Research, Wayne, New Jersey) at a speed of 200 frames per second and a resolution of $1280 \times 800$ pixels. Images were then extracted and analyzed using MATLAB image analysis toolbox. Firstly, the background of the image was subtracted by the image without bubble injection. After that, the processed image was converted from grayscale to black-and-white. The edge of the bubble was detected and the interior gaps inside the edge were filled. The bubble in the image was then fitted with an ellipse. The bubble shape was considered to be ellipsoidal, of which the major axis ($a$) in the horizontal direction and minor axis ($b$) in the vertical direction can be measured directly from the image (Figure 3-2). The third axis perpendicular to the image plane (also in the horizontal direction) was assumed to equal the major axis ($a$), as the difference between the two horizontal axes is less than 10% (Liu et al. 2015). The bubble equivalent diameter was defined as the diameter of a sphere volume-equivalent to such a spheroid: $D = \sqrt[3]{a^2 b}$. Note that using the equivalent diameter $D$ would underestimate the surface area of an ellipsoidal bubble. This estimation for the bubble equivalent diameter based on two-dimensional images was widely used in previous studies (Sam et al. 1996; Botello-Álvarez et al. 2011). This method was validated using two glass beads with diameters of 3 mm and 15.85 mm falling in the water tank. The predicted diameters of small and large glass beads were 3.15 mm and 16.16, showing a decent agreement with their actual sizes.

## 3.3. Mathematical Formulation

An analytical model for the mass transfer of a single bubble rising in stagnant water is developed here. The bubble release depth (defined as the distance from where the bubble is released to the water surface) is $H$, the bubble diameter is $D$ and its rising velocity is $U$, as illustrated in Figure 3-1. Although the bubble rising path can be oscillatory for relatively large bubbles, it is simplified to be a straight line in the model. The rising bubble is also assumed to have a spherical shape. The water temperature is considered constant. After a rising distance of $dz$ ($z$ is the vertical distance from the release point, as illustrated in Figure 3-1), the mass transferred from the bubble to the water is:

$$dM = -\sum_{j=1}^{N} K_{L_j} \pi D^2 \left( C_{s_j} - C_j \right) \frac{dz}{U} X_j \text{ (kg)} \quad (3-1)$$

where $X_j$ = molar fraction of a specific gas in the bubble ($X_j$ = 100% when there is only a single component of gas in the bubble, e.g. pure $CO_2$ bubble), subscript $j$ = the specific gas species, and $N$ = number of gas species, including nitrogen, oxygen, and other important gases ($N \geq 2$). The equilibrium concentration of a specific gas ($C_{s_j}$) in the bubble is

$$C_{s_j} = \frac{P X_j}{He_j} \text{ (kg m}^{-3}) \quad (3-2)$$

where $He$ is Henry's law constant of the specific gas, and $P$ is the pressure inside the bubble.

For dissolved gas saturation concentration at the atmospheric pressure in the water ($Ceq_j$), it can be calculated as $C_{eqj} = P_{atm} X_j / He_j$, $P_{atm}$ is the atmospheric pressure. In tap water, the dissolved nitrogen and dissolved oxygen are the main components of the total dissolved gas in water. The

mass transfer of the dissolved nitrogen and oxygen can be important to bubble size and thus, it is included in the model. The molar fraction of dissolved nitrogen and oxygen in water with saturated dissolved air are assumed to be 78% and 21%, respectively.

Takemura and Yabe (1998) developed an empirical equation for the mass transfer coefficient of a gas bubble at Reynolds number below 100 (or bubble diameter less than 0.8 mm), and Lochiel and Calderbank (1964) proposed an equation for bubble Reynolds number more than 100. Both equations show that the mass transfer coefficient is affected by the molecular diffusivity ($D_m$), bubble Peclet number ($P_e = UD/D_m$), bubble diameter, and bubble Reynolds number ($Re = \rho_w DU/\mu_w$, $\mu_w$ = water dynamic viscosity):

$$K_L = \begin{cases} \dfrac{2D_m}{D\sqrt{\pi}}\left[1 - \dfrac{2}{3}\dfrac{1}{(1 + 0.09Re^{2/3})^{3/4}}\right]Pe^{1/2} \text{ (m s}^{-1}) & \text{for } D \leq 0.8mm \\[4mm] \dfrac{1.13D_m}{D}\sqrt{(1 - \dfrac{2.96}{Re^{1/2}})}Pe^{1/2} \text{ (m s}^{-1}) & \text{for } D > 0.8mm \end{cases} \qquad (3-3)$$

The mass transfer coefficients used in this study have been proved to be able to accurately predict the bubble-water mass transfer (Politano et al. 2009; Nock et al. 2016). However, these mass transfer coefficients can only be applied for bubbles under conditions where the Reynolds number is less than 100.

Untreated tap water used in the experiments was likely to contain some surfactants, which could affect the bubble rising velocity (Haberman and Morton 1953). Surfactants in water could increase the drag force and therefore decrease the bubble rise velocity. Fan and Tsuchiya (1990) reported that the bubble rising velocity in distilled water was higher than that in tap water, especially when the bubble diameter was $1 - 3$ mm. Huang and Saito (2017) also found that the surfactants (500

ppm 1-pentanol) reduced the bubble rising velocity by about 15% with the bubble diameter of 2.9 mm. In this study, bubble rising velocities were measured in the de-ironized water and the untreated tap water. Only 1% difference of the bubble rising velocities was observed, which indicated a minor influence of the surfactants in the untreated tap water in this study.

In the current study, the bubble rising velocity was assumed to be its terminal velocity, since that a bubble accelerates from zero velocity to the terminal velocity in about 0.2 second (Sam et al. 1996). The terminal velocity can be calculated based on the balance of forces acting on the bubble:

$$(\rho_w - \rho_g)gV = \pi \frac{D^2}{4} \frac{\rho_w U^2}{2} C_D \quad (3-4)$$

where $V = \pi D^3/6$ is the bubble volume, $\rho_g$ is the gas density, and $C_D$ is the drag coefficient. Neglecting the gas density, the bubble terminal velocity can be written as:

$$U^2 = \frac{4}{3} \frac{gD}{C_D} \quad (3-5)$$

In tap water, for bubbles with a diameter smaller than 2.6 mm and bubble Reynolds number less than 650, the drag coefficient can be estimated as (McGinnis and Little 2002):

$$C_D = \frac{24}{Re} + \frac{3}{\sqrt{Re}} + 0.34 \quad (3-6)$$

This method has also been used in predicting rising velocity of carbon dioxide bubbles in water (Nock et al. 2016). The bubble rising velocity then can be solved from Equations (3-5) and (3-6). For bubbles larger than 2.6 mm, the rising velocity in tap water can be calculated as (Jamialahmadi et al. 1994):

$$U = \sqrt{\frac{2\sigma}{D(\rho_w + \rho_g)} + \frac{gD}{2}} \quad (\text{m s}^{-1}) \quad (3-7)$$

where $\sigma$ is the surface tension.

The gas inside the bubble is assumed to follow the ideal gas law:

$$PV = P\pi D^3/6 = nRT \quad (3-8)$$

where $n$ is the number of moles, $R$ is the gas constant, and $T$ is the temperature. From Equation (3-8), the bubble volume changes with both hydrostatic pressure and mass transfer. The amount of gas transferred from the bubble to the water is:

$$dn = -dM/M_m \quad (\text{mol}) \quad (3-9)$$

where $M_m$ is the molar mass of the gas. Combining Equations (3-1) to (3-9), the bubble-water mass transfer along $dz$ can be calculated. The mass transfer efficiency $E$ is defined as the ratio of the total gas mass transferred from the bubble to the initial mass ($M_0$):

$$E = \frac{M_0 - M}{M_0} \quad (3-10)$$

Equations (3-1) to (3-10) were solved with MATLAB code using upwind scheme, where $dz$ was set to be 0.005 m to obtain a good accuracy for this model. The temperature was set to be 20 °C for all the model predictions in this study. Note that the model is generally applicable for a single bubble of any gas species.

## 3.4. Results and Discussion

The proposed model was first validated using the current experimental measurements of the bubble size variation along the rising path, as shown in Figure 3-3(a-d). Bubble diameter decreases during the rising under all the test conditions due to the mass transfer from the bubble to the water. Significant scatterness in the experimental data and large differences between measured bubble sizes and predicted bubble sizes were observed. The main reason was that bubbles were only filmed on a single plane, leading to the overestimation or underestimation of the bubble size. Additionally, resolutions of bubbles in the photos were between 9 and 16 pixels, thus the measurement error could also contribute to the scatterness in the measured bubble sizes. Overall, the model predictions compare well with the mean measured bubble sizes, indicating the reliability of the model. The model prediction was also compared with the experiments reported by Nock (2015). The predictions for the bubble diameter and the amount of gas in the bubble are plotted along with the experimental data in Figure 3-3(e-f). The current model reduces the deviation between the experimental data and predictions from about 19% to 4% compared with Nock's model. The difference of the two models mainly lies in the selections of equations for mass transfer coefficient and drag coefficient.

The mass transfer of dissolved nitrogen and oxygen in the water to the rising bubble can be important to bubble size variation. This was tested by running the model both with and without considering the dissolved gas mass transfer, for a pure $CO_2$ bubble with an initial diameter of $D_0$ = 3 mm released at a water depth of 0.6 m. The final bubble size, i.e., the size when the bubble reaches the water surface, is 23.1% larger after including the mass transfer from dissolved nitrogen and oxygen. However, the dissolved nitrogen and oxygen have little influence on the mass transfer efficiency of $CO_2$ along the rising trajectory, with no more than 3% difference for $CO_2$ bubble released at a water depth of 0.6 m. When the dissolved nitrogen and oxygen is transferred into the

bubble along its rising path, the bubble-water interfacial area increases while in the meantime, the molar fraction and the partial pressure of the $CO_2$ in the bubble decreases. These two factors tend to neutralize their net effect on $CO_2$ mass transfer.

By adjusting the gas physical properties, the model developed in this study was used to evaluate the bubble-water mass transfer for different gases. The diameter and mass transfer efficiency of air, oxygen, carbon dioxide and methane bubbles with $D_0 = 3$ mm were predicted, as illustrated in Figure 3-4. The mass transfer efficiency of the pure $CO_2$ bubble reaches 100% in about 0.75 m, but the bubble does not disappear due to the mass transfer of the dissolved nitrogen and oxygen into the bubble. The terminal mass transfer efficiencies $E_t$ (the mass transfer efficiency when a bubble reaches the water surface) of the methane and oxygen bubbles are similar, which are about 4 times that of the air bubble. In the following sections, the effects of bubble horizontal velocity, bubble release depth, initial bubble size, and dissolved gas concentration in water on bubble mass transfer are evaluated using the current model.

### 3.4.1. Effects of Bubble Horizontal Velocity

It was observed from the experiments that bubbles rose in an oscillating path, similar to the zigzag trajectory of rising bubbles reported in Tsuge and Hibino (1971) and Tripathi et al. (2015). The horizontal velocity of the bubble was induced by bubble surface oscillation and wake vortices (Shew and Pinton 2006). Although the types of bubble oscillating paths (e.g. zigzag and helical) have been widely discussed, no theoretical method for predicting the oscillating path or bubble horizontal velocity has been established (Aybers and Tapucu 1969; Clift et al. 1978; Tripathi et al. 2015).

For the current experiments, the bubble velocities in vertical and horizontal directions were

measured from the images taken by the high-speed camera, as plotted in Figure 3-5. The bubble horizontal velocity was approximately in a harmonic mode with an amplitude of about 60% of the bubble vertical velocity for $CO_2$ bubbles of $D_0 = 3$ mm. Due to the limitation of the two-dimensional image, the velocity component perpendicular to the image plane was assumed to be the same as the horizontal velocity measured from the image. The resultant bubble velocity was then calculated based on the velocities in these three directions, which was then used to compute the bubble Reynolds number and mass transfer coefficient in Equation (3-3). In the previous studies, the bubble horizontal velocity was typically ignored when estimating the mass transfer coefficient (Lochiel and Calderbank, 1964; Takemura and Yabe, 1998). The effect of bubble horizontal velocity on the bubble-water mass transfer was analyzed based on the predictions with the proposed model.

For a single $CO_2$ bubble of $D_0 = 3$ mm rising through a 0.3 m water column with fully saturated air, the predicted mass transfer efficiency was increased from 61.9% to 64.7% when including the horizontal velocity. Additionally, Ellingsen and Risso (2001) reported that the horizontal velocity of an air bubble ($D_0 = 2.5$ mm) was about 55% of the vertical velocity. If this air bubble was released at a water depth of 20 m, the inclusion of the horizontal velocity only increased the mass transfer efficiency by 2.9%, when the water is fully saturated with air. The inclusion of horizontal velocity increases the mass transfer coefficient and thus promotes the mass transfer rate. Note that the bubble size becomes smaller when including the horizontal velocity, the mass transfer rate would be constrained due to the less bubble-water interfacial area though it has a higher mass transfer coefficient. This indicates the influence of horizontal velocity on mass transfer efficiency is not expected to significantly increase with bubble release depth. The results show that the bubble horizontal velocity has a limited effect on the bubble-water mass transfer and thus, it is not

considered in the subsequent model predictions.

### 3.4.2. Effects of Bubble Release Depth

The influence of bubble release depth on bubble-water mass transfer was also examined with the proposed model. In the model, the target gas was set to be pure oxygen. The oxygen bubble had an initial diameter of 3 mm and the water was saturated with dissolved air under atmospheric pressure, i.e., the background DO concentration in water was the dissolved oxygen saturation concentration at the atmospheric pressure with a molar fraction of 21% ($C_{eqO2}$). The model predictions for the bubble size and mass transfer efficiency along the rising path with different bubble release depths are presented in Figure 3-6(a, b). From Figure 3-6(a), the bubble size at the water surface decreases with the release depth, which indicates a higher mass transfer rate in deeper water. The sizes of bubbles released from different water depths all keep decreasing until reaching the depth of 6 m. Above this depth, the bubbles expand along the rising path. A critical depth (the distance from the free surface) then can be defined for measuring the bubble size change as bubble rising. The variation of the bubble volume along the rising trajectory is:

$$\frac{V_{i+1}}{V_i} = \frac{n_{i+1}P_i}{n_i P_{i+1}} = \frac{n_i P_i - P_i \frac{dM_i}{M_m}}{n_i P_i - n_i \rho_w g dz} \quad (3-11)$$

where the subscripts $i$ and $i + 1$ represent sequent time steps.

The critical depth $h_c$ occurs when $V_{i+1}/V_i = 1$, i.e., $P_i \frac{dM_i}{M_m} = n_i \rho_w g dz$. Substituting Equations (3-1) into this equation, the critical depth can be expressed with

$$h_c = \frac{U_i D_i \rho_{gi}}{6K_{L_i}(C_{s_i} - C)} - \frac{P_{atm}}{\rho_w g} \text{ (m) } (3-12)$$

For a bubble of a specific gas, the values of $C_{s_i}$, $\rho_{gi}$, and $P_i$ are only dependent on its vertical location in the water. The term $U_i D_i / K_{L_i}$ monotonously increases with the bubble diameter based on the model calculation, as shown in Figure 3-7, which also compares well with the experimental data from Motarjemi and Jameson (1978). From Figure 3-6(b), the mass transfer efficiency increases as the bubble rises. For the bubbles of $D_0 = 3$ mm in Figure 3-6(b), only 42% of oxygen dissolves in the water column of 6 m deep while 68% in that of 12 m deep, which shows that the terminal mass transfer efficiency increases with the bubble release depth owing to the longer bubble residence time and larger concentration difference $(C_{si} - C)$ in deeper water.

### 3.4.3. Effects of Bubble Diameter and Background Dissolved Oxygen Level

For the oxygen bubbles with different initial diameters of $D_0 = 1, 2, 3,$ and 4 mm, their diameter change and mass transfer efficiency along the rising path were predicted with the model, as shown in Figure 3-6(c, d). The water was set to be fully saturated with dissolved air under atmospheric pressure. From Figure 3-6(c), the bubble with a small initial diameter of $D_0 = 1$ mm keeps shrinking during its rising, and the diameter is reduced by about 40% when it reaches the water surface. The bubble with a larger initial diameter of $D_0 = 4$ mm, on the other hand, inflates along the rising trajectory. This shows that for the larger bubble, the hydrostatic pressure plays a more important role in bubble size than the mass transfer. According to Equation (3-12) and the variation of the term $U_i D_i / K_{L_i}$ with bubble diameter in Figure 3-7, when the bubble release depth is the same, smaller bubbles always have a smaller $h_c$, which explains the bubble size change in Figure 3-6(c). From Figure 3-6(d), the bubble of $D_0 = 1$ mm performs the highest terminal mass transfer efficiency of 96%, whereas that for the bubble of $D_0 = 4$ mm is only 38%. Oxygen bubbles with a smaller diameter have a larger specific surface area, which leads to a more significant bubble-

water mass transfer.

The effect of dissolved oxygen concentration in water on bubble-water mass transfer was also analyzed with the model. The bubble size and mass transfer efficiency along the bubble rising trajectory predicted with different background DO levels are presented in Figure 3-6(e, f). From Figure 3-6(e), when the conditions of initial bubble size, water temperature, gas species, and bubble release depth are the same, a lower background DO level in the water leads to a smaller bubble size, i.e., more oxygen is dissolved in the water from the bubble. Correspondingly, a higher mass transfer efficiency is achieved with a lower background DO level, as shown in Figure 3-6(f).

### 3.4.4. *Mass Transfer Model for Bubble Swarms*

Different from a single rising bubble, bubble dynamics and mass transfer rate are affected by bubble interactions in a bubble swarm. Wakes will be generated behind rising bubbles greater than approximately 0.5 mm. Nock (2015) found that for bubbles with a diameter of about 2 mm, the average rising velocity within a bubble swarm was about 10% higher than that of a single bubble. Tomiyama (1998) proposed an equation for the average drag coefficient of bubbles within a bubble swarm in tap water ($D_0 \leq 10$ mm):

$$C_D = \max[\min\left[\frac{16}{Re}(1 + 0.15Re^{0.687}), \frac{48}{Re}\right], \frac{8}{3}\frac{E_O}{E_O + 4}] \quad (3-13)$$

where $E_O = \frac{g(\rho_w - \rho_g)D^2}{\sigma}$ is the Eotvos number. Higbie (1935) and Calderbank and Moo-Young (1961) proposed equations for estimating the mass transfer coefficient in a bubble swarm, which are applicable for bubbles of various sizes:

$$K_L = \begin{cases} 1.13\sqrt{\dfrac{U}{D}}\sqrt{D_m} & \text{for } D \leq 3mm \\[4mm] 0.42\left[\dfrac{(\rho_w - \rho_g)\mu_w g}{\rho_w{}^2}\right]^{1/3}\left(\dfrac{\mu_w}{\rho_w D_m}\right)^{-1/2} & \text{for } D > 3mm \end{cases} \qquad (3-14)$$

Applying Equations (3-13) and (3-14) to the model, the model was run for the experiments in Nock (2015). The average bubble diameters along the rising path within a bubble swarm with 50% and 100% $CO_2$ input concentration were predicted in the water with fully saturated air. The model predictions were plotted in Figure 3-8, together with the measured data reported by Nock (2015).

### 3.4.5.  *Prediction of Dissolved Gas Concentration in Water*

For continuously injected bubble swarms, the wake vortex generated by the preceding bubbles leads to an acceleration of those that follow (Koynov et al. 2005). Applying the bubble swarms model, the mass transfer efficiency of an air bubble within a bubble swarm with various initial diameters are computed, as shown in Figure 3-9, together with that of a single air bubble for comparison. The mass transfer efficiencies of the two types of bubbles are close, with a difference up to 1.5% under all the test conditions. The small difference is due to the lower residence time and larger mass transfer coefficient for the bubble in a bubble swarm compared to a single bubble. This indicates the mass transfer of continuously injected bubble swarms may also be predicted by the single bubble model.

Under the condition of continuous bubble injection, the mass transfer across the water surface can be important and in this case, the background dissolved gas concentration with bubbles released in *dt* varies as:

$$C_{i+1} = \frac{C_i V_w + M_0 E_t F dt - K_S A_w (C_i - C_{eq})dt}{V_w} \qquad (3-15)$$

where $K_S$ is the mass transfer coefficient for a specific gas across the water surface; $dt = 1$ s; $C_{eq} =$ gas saturation concentration at the atmospheric pressure; $V_w = A_w H$ is the volume of water body, and $A_w =$ the water surface area for mass transfer. In the current experiments, the bubble plume can induce circulation in the waterbody and promote the mixing of the dissolved gas. For simplification, it is assumed that the dissolved gas in the water is fully mixed and $A_w$ equals the entire water surface area in the tank. Note that the mass transfer at the water surface can be either from the atmosphere to the water or in the opposite direction if the water is supersaturated (DeMoyer et al. 2003).

The model including the surface mass transfer was validated with the air-bubble dissolution in a 14-m-deep tank filled with tap water, as reported in McGinnis and Little (2002). In the experiments, the dissolved oxygen was measured under the number flux of bubble $F = 57560 - 91030$ per hour through a 1.5-m length diffuser with 6.4-mm diameter porous hoses, which was located at 0.6 m above the tank bottom. Wilhelms and Martin (1992) determined a surface mass transfer coefficient value of 0.00011 m/s in a similar experiment, which was used in the model. The predictions by the proposed model including the mass transfer across the water surface and those by the model in McGinnis and Little (2002) are both plotted in Figure 3-10, together with the experimental data for comparison. The predicted DO by the proposed model shows a better agreement with the measured data, which reduces the deviation from about 15% to 4%.

The proposed model can be applied to a wide range of engineering applications. Its application in water aeration systems is presented in the following. The variations of DO level under different conditions of bubble sizes, air flow rate, and bubble release depths were calculated with the model. In the model, the total air-bubble injection duration was 180 minutes. The water was undersaturated with an initial DO concentration of 2 mg/L. The bubble injection density was

uniformly distributed and set to be 1100 nozzles per square meter. The generated DO was assumed to be fully mixed in a short time, and the temperature was kept 20 °C. The model predictions are shown in Figure 3-11. From Figure 3-11(a), with the same bubble release depth, the DO concentration generally increases with the initial bubble diameter and the number flux of bubbles. When the air bubble flow rate is constant, the effect of bubble release depth on the DO concentration is less substantial, especially when the initial bubble diameter is less than 3 mm, as shown in Figure 3-11(b). Based on the model predictions, the design and operation of water aeration system can be optimized for a desired aeration efficiency with a reduced cost.

## 3.5. Conclusions

The mass transfer and size change of a single bubble rising in stagnant water was investigated with an analytical model, along with experimental measurements for model validation. A good agreement was achieved between the model predictions and the experimental data. The bubble size change and mass transfer efficiency along the bubble rising trajectory under different conditions were calculated. Based on the model predictions, the bubble horizontal velocity had a limited effect on the bubble-water mass transfer. The terminal mass transfer efficiency increased with the bubble release depth, which was due to the longer bubble residence time and the larger gas concentration gradient between inside and outside of the bubble. The critical depth was proposed to measure the bubble size change as rising. The bubble size kept decreasing when it was beneath the critical depth, where the effect of the mass transfer on the bubble size was more significant than the hydrostatic pressure. Additionally, the mass transfer efficiency decreased with the initial bubble size. A high dissolved gas concentration in water constrained the bubble-water mass transfer. The mass transfer of a bubble within bubble swarms was similar to a single bubble.

The model established in the current study is generally applicable for different gases. It reduces the deviation between the experimental data and predictions from about 15% to 4% by including the influence of changing dissolved concentration and mass transfer across the water surface, in comparison with previous model predictions. The model is meaningful in a wide range of engineering applications, one of which is to be used in water aeration systems to optimize the device operation and its design for a desired aeration efficiency with a reduced cost. Although the developed model is only applicable to laminar flow, it can be applied in turbulent flow if mass transfer coefficients are changed correspondingly. In the future study, bubble imaged can be filmed on two planes to obtain more accurate bubble size along the rising trajectory.

## Notation

The following symbols are used in this paper:

$a$ = major axis of the bubble, mm;

$b$ = minor axis of the bubble, mm;

$A$ = bubble-water interfacial area, m$^2$;

$A_w$ = specific water surface area, m$^2$;

$C$ = dissolved gas concentration, kg m$^{-3}$;

$C_D$ = drag coefficient, dimensionless;

$C_{eq}$ = gas saturation concentration at atmospheric pressure, kg m$^{-3}$;

$C_s$ = liquid-phase equilibrium concentration under the local partial pressure, kg m$^{-3}$;

$D$ = bubble diameter, mm, m;

$D_0$ = initial bubble diameter, mm, m;

$D_m$ = molecular diffusivity of a specific gas in water, $m^2\ s^{-1}$;

$E$ = mass transfer efficiency, dimensionless;

$E_t$ = terminal mass transfer efficiency, dimensionless;

$F$ = number flux of bubble entering water, $min^{-1}$;

$g$ = gravity acceleration $m\ s^{-2}$;

$H$ = total bubble release depth, m;

$H_c$ = critical depth, m;

$He$ = Henry's law constant, $m^3\ Pa\ kg^{-1}$;

$K_L$ = mass transfer coefficient across the bubble interface in stagnant water, $m\ s^{-1}$;

$K_S$ = mass transfer coefficient across water surface, $m\ s^{-1}$;

$M_0$ = initial gas-bubble mass at the bottom of the water column, kg;

$M$ = local mass of the gas inside the bubble, kg;

$M_m$ = molar mass of the gas, $kg\ mol^{-1}$;

$M_s$ = gas mass transferred through water surface, kg;

$n$ = mole number of the gas, mol;

$N$ = number of gas species, dimensionless;

$P$ = total pressure of the gas, Pa;

$P_{atm}$ = atmospheric pressure, Pa;

$P_e$ = bubble Peclet number, dimensionless;

$R$ = gas constant, m$^3$ Pa K$^{-1}$ mol$^{-1}$;

$Re$ = bubble Reynolds number, dimensionless;

$T$ = temperature, K;

$t$ = time, s;

$U$ = bubble rising velocity, m s$^{-1}$;

$V$ = bubble volume, m$^3$;

$V_w$ = the specific volume of water column, m$^3$;

$X$ = mole fraction of a specific gas, dimensionless;

*Greek letters*

$\rho_g$ = gas density, kg m$^{-3}$;

$\rho_w$ = water density, kg m$^{-3}$;

$\mu_w$ = dynamic viscosity of water, Pa s;

$\sigma$ = surface tension, N m$^{-1}$;

*Superscripts and subscripts*

$i$ = local time step;

$j$ = gas species index;
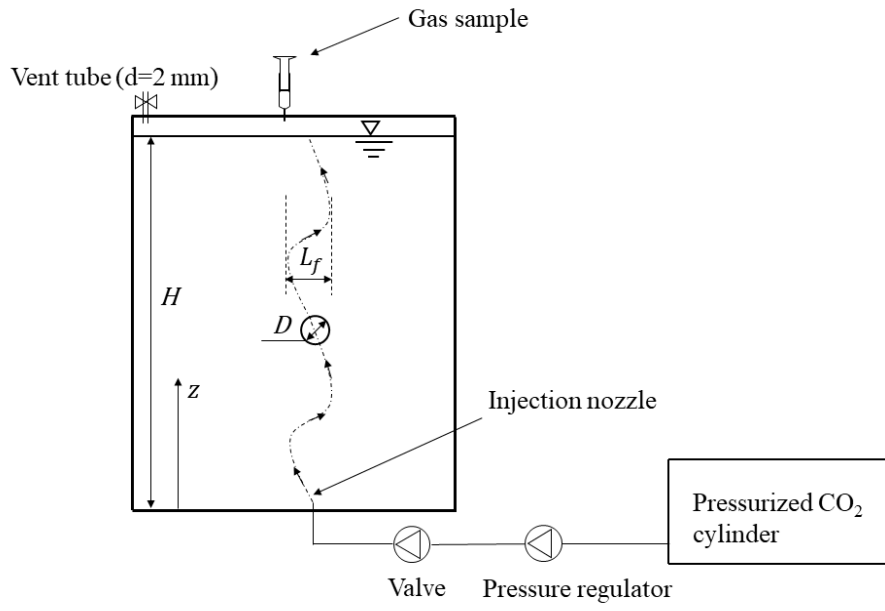
Figure 3-1 Schematic of the experimental setup.
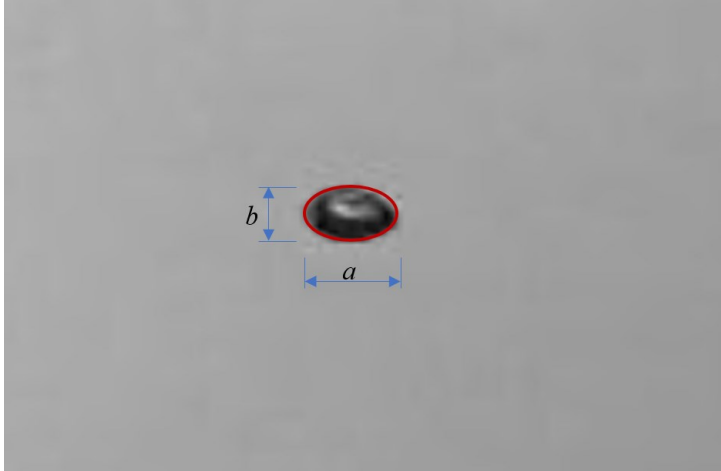
Figure 3-2 Major axis (*a*) and minor axis (*b*) of a bubble with an equivalent diameter of 3.1 mm.
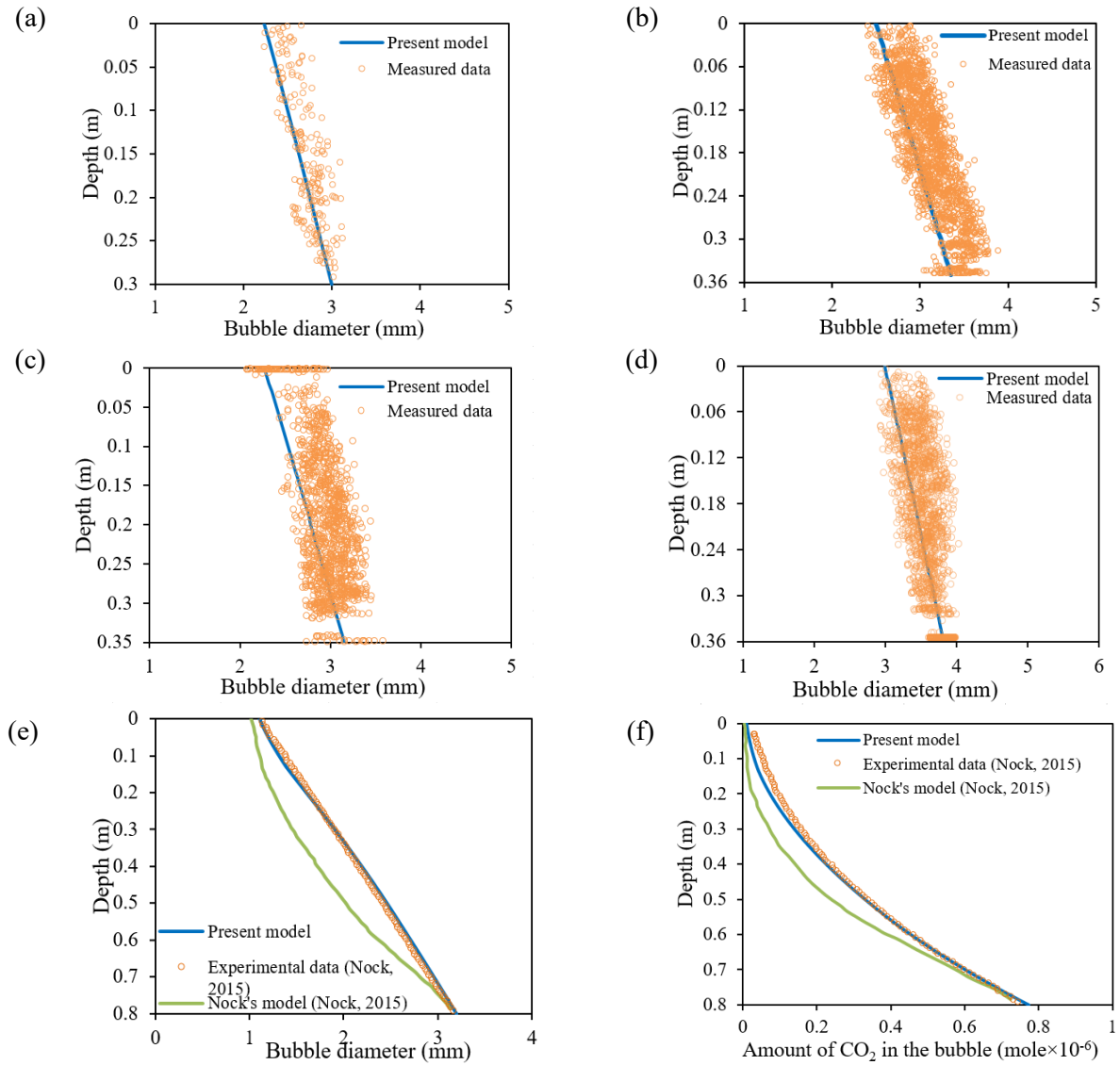
Figure 3-3 Predicted and measured $CO_2$ bubble diameter along the rising trajectory: (a) $F = 28$ min$^{-1}$, (b) $F = 105$ min$^{-1}$ and (c) $F = 44$ min$^{-1}$ released from the 0.9 mm diameter orifice; (d) $F = 46$ min$^{-1}$ released from the 2.5 mm diameter orifice; predicted and measured (e) bubble diameter and (f) amount of $CO_2$ in the bubble in the case reported by Nock (2015).

(a)



(b)
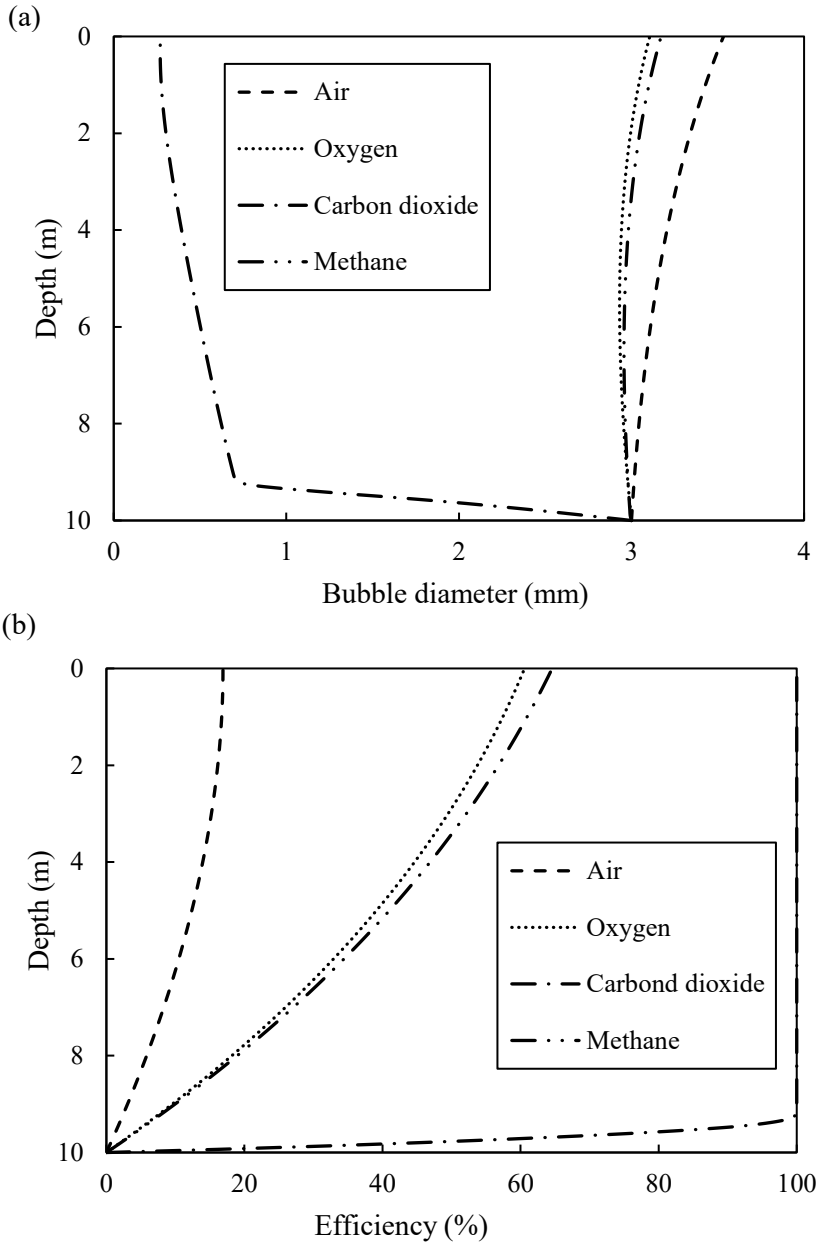


Figure 3-4 Variation of (a) bubble diameter and (b) mass transfer efficiency along the rising

trajectory for the bubbles of air, oxygen, carbon dioxide, and methane with an initial diameter

of $D_0 = 3$ mm.
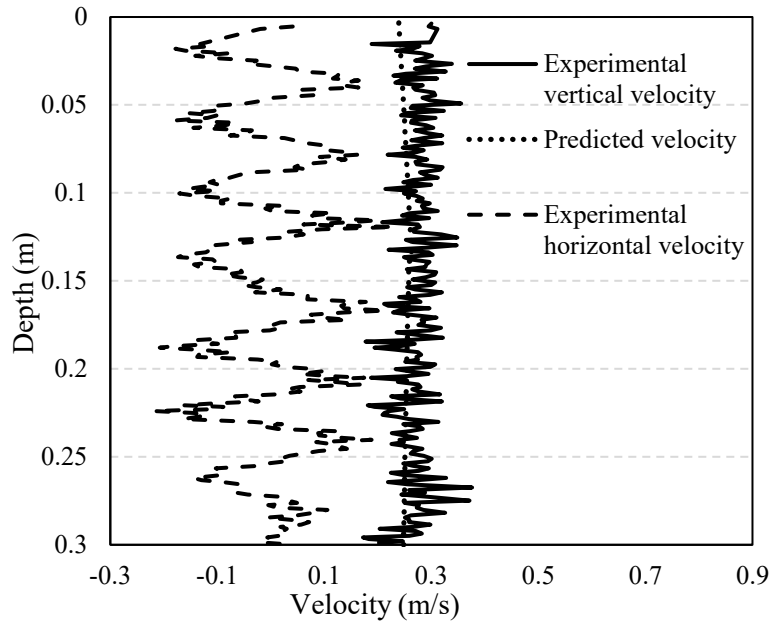
Figure 3-5 Predicted and measured bubble velocity in the 0.3-m-deep water tank ($CO_2$ bubble was released from the 0.9 mm diameter orifice).
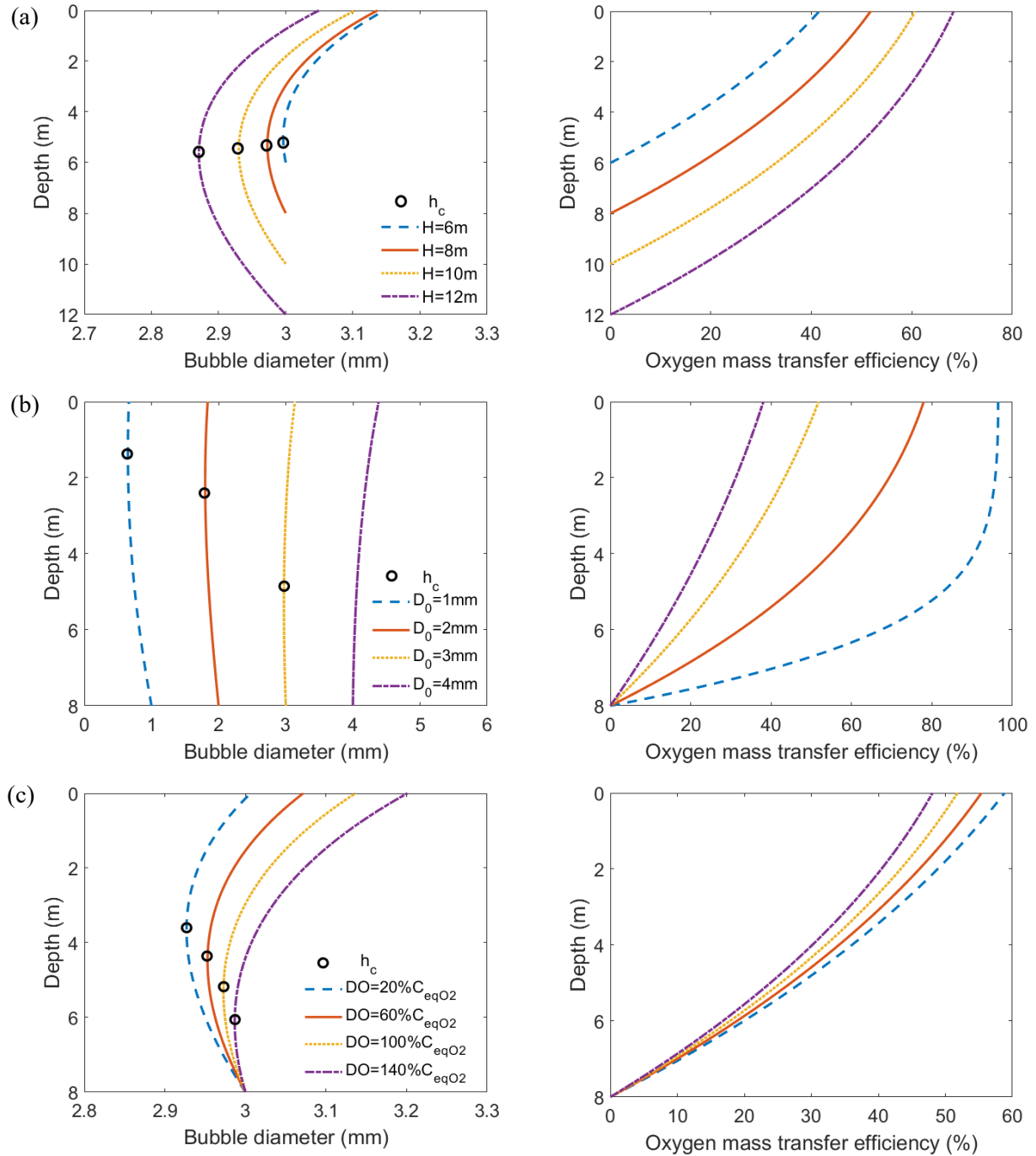
Figure 3-6 Oxygen bubble diameter change (left) and mass transfer efficiency (right) along the rising trajectory with: (a) bubble release depths of $H = 6$, 8, 10 and 12 m ($D_0 = 3$ mm, $DO = 100\% \, C_{eqO2}$); (b) $D_0 = 1$, 2, 3 and 4 mm ($H = 8$ m, $DO = 100\% \, C_{eqO2}$); (c) $DO = 20\%$, 60%, 100% and 140% $C_{eqO2}$ ($H = 8$ m, $D_0 = 3$ mm). The critical depth is marked with '○'.

52
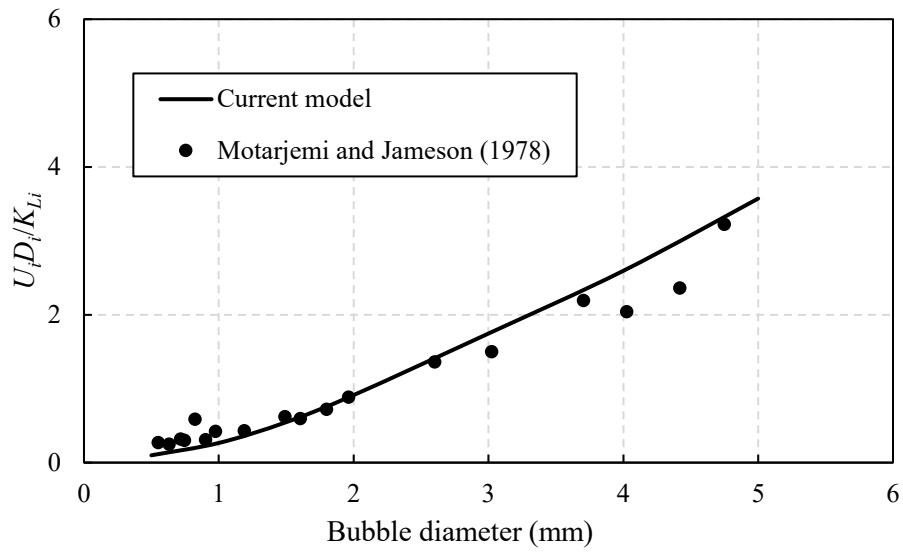
Figure 3-7 Variation of $U_i D_i / K_{Li}$ with the bubble diameter.
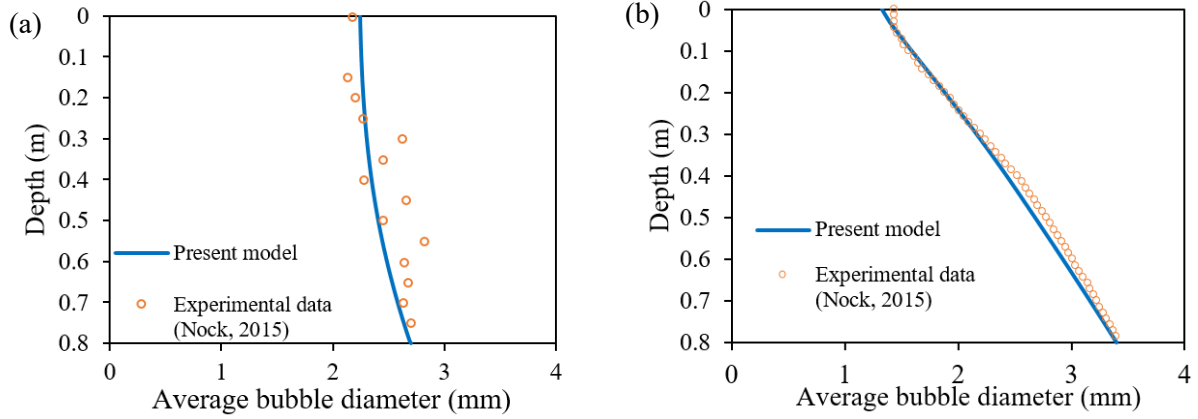
Figure 3-8 Change in average bubble diameter within bubble swarms with (a) 50% $CO_2$ input concentration and (b) 100% $CO_2$ input concentration (water is assumed to be fully saturated with air under atmospheric pressure).
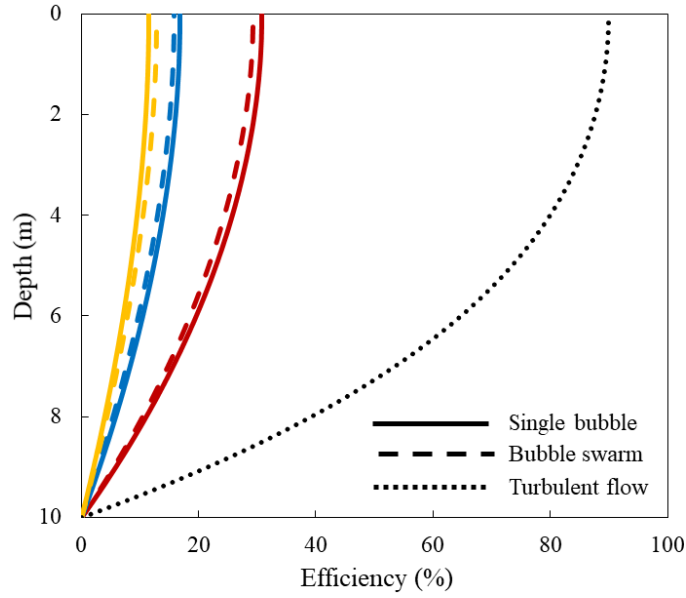
Figure 3-9 Variation of mass transfer efficiency along the bubble rising trajectory for a single bubble and bubble swarms with various initial diameters of $D_0 = 2$ mm (red lines), 3 mm (blue lines) and 4 mm (yellow lines).
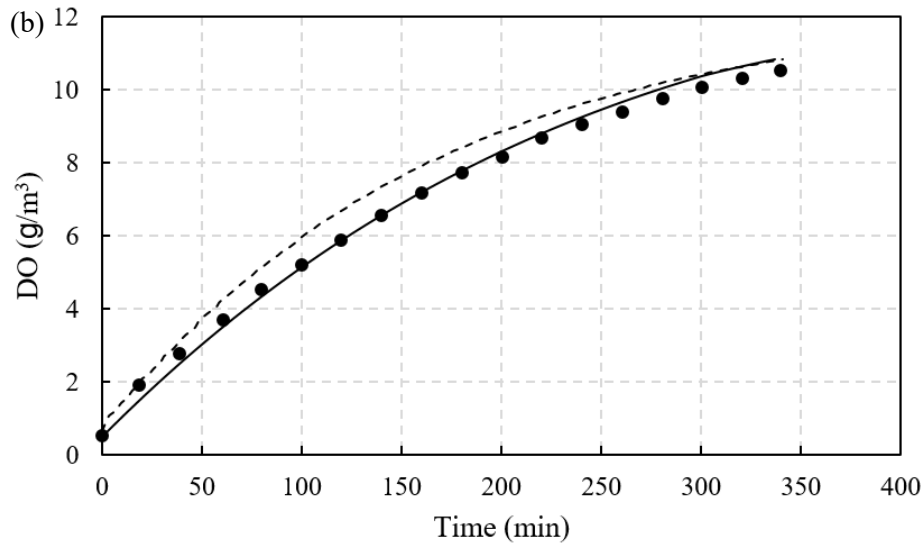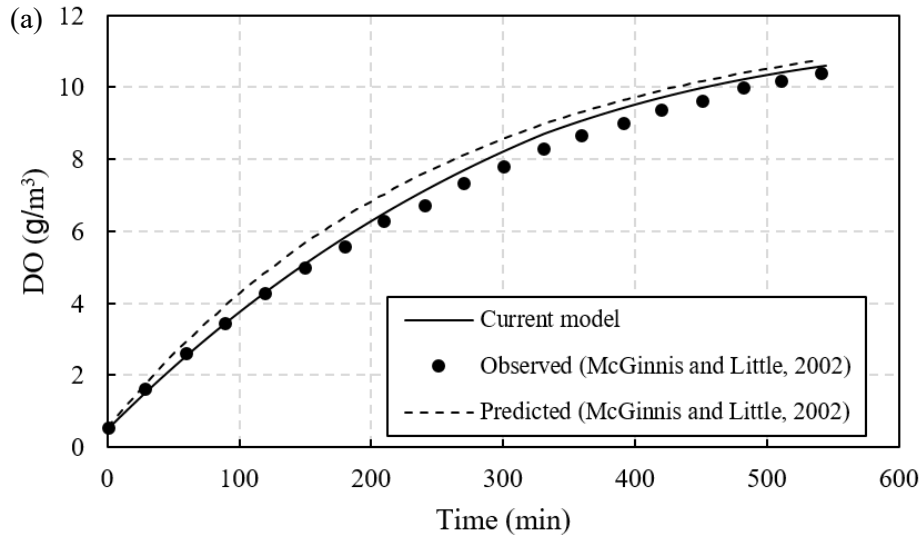
Figure 3-10 Predictions for the DO concentrations with the proposed model and the model in McGinnis and Little (2002), under the condition of (a) $F = 57560$ h$^{-1}$ and (b) $F = 91030$ h$^{-1}$ (experimental data was from McGinnis and Little 2002).
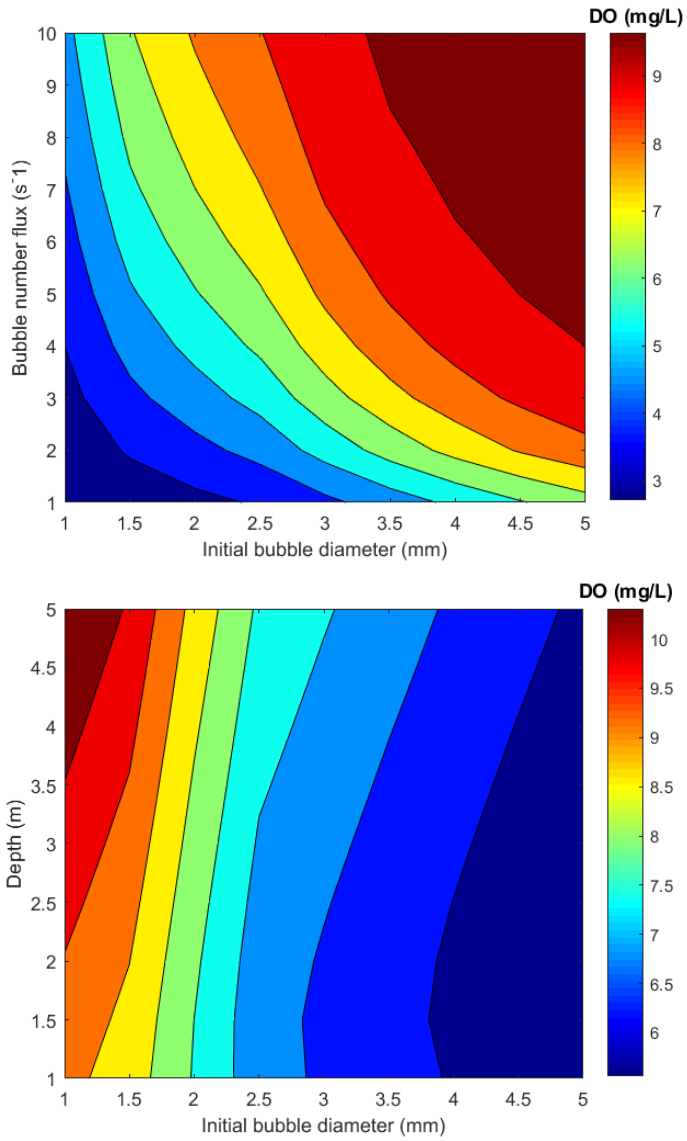
Figure 3-11 Variation of DO level with various (a) air bubble injection frequencies ($H$ = 2 m) and (b) release depths (air flow rate is 0.38 m³/h), after a bubble injection duration of 180 minutes.

# 4. Air Demand of a Hydraulic Jump in a Closed Conduit [*]

## 4.1. Introduction

Air can be entrained into flowing water by a hydraulic jump. Understanding the air demand and proper ventilation of a hydraulic jump inside a closed conduit are important in hydropower operations and urban sewer designs. For instance, negative pressure, blowback, and other problems can be caused by entrained air in pipes or closed conduits in hydropower facilities (Bosman et al. 2016). Air entrainment and transport are also important in municipal engineering applications as in ventilation and sewer odor related issues (Edwini-Bonsu and Steffler, 2004; Qian et al. 2017). Additionally, the entrained air bubbles can be dissolved into water in the tailrace of hydropower plants and cause gas bubble disease to fish due to supersaturated total dissolved gases or dissolved oxygen (Weitkamp and Katz 1980; Chapman 1986; Stefan and Fang 1994). Thus it is crucial to predict the air demand in a closed conduit under different outlet conditions to ensure proper design and operations of these hydraulic structures.

Flow in closed conduits can have different flow patterns and flow regimes, some of which involve hydraulic jumps in different forms. Hewitt and Hall-Taylor (1970) distinguished six regimes for horizontal gas-liquid flow without a hydraulic jump, such as slug flow, bubbly flow, etc. Sharma (1976) classified six types in the study of air entrainment downstream of a sluice gate in a low-level outlet for various gate openings and the downstream submergence. Stahl and Hager (1999) identified four different types of hydraulic jumps, from undular hydraulic jump to hydraulic jump

---

[*] The content of this chapter has been submitted as a journal manuscript: Li, P., Zhu, D. Z., Xu, T., and Zhang, J. (2021). "Air Demand of a Hydraulic Jump in a Closed Conduit." *Journal of Hydraulic Engineering*, ASCE, Manuscript ID HYENG-12849, under review

with a near full pipe flow, based on the approach flow Froude number and the gate opening.

The characteristics of a hydraulic jump and its return roller have been systematically investigated by Rajaratnam (1967) and Long et al. (1991), and the air entrainment and transport are affected by the hydraulic jump (Chanson 1996; Mortensen et al. 2012; Takahashi and Ohtsu 2017). Additionally, airflow induced by flowing water in pipes has received significant attention in the past several decades (e.g., Qian et al. 2021). Air entrainment in a closed conduit with supercritical flow with or without a hydraulic jump has also been widely investigated. Kalinske and Robertson (1943) conducted the very first experiments on air entrainment of hydraulic jumps within circular pipes. The measured air entrainment rate was correlated to the Froude number upstream of the jump and found to be independent of pipe length and slope. Rajaratnam (1967) proposed that the air entrainment of a hydraulic jump originates mainly from the drag of the surface of the supercritical flow and the turbulent mixing generated by the hydraulic jump. Wisner (1967) correlated the air demand induced by supercritical free-surface flow to the Froude number based on experimental measurements. Sharma (1976) conducted a series of experiments in a rectangular conduit with a vertical gate to investigate the air demand for free surface flow with a hydraulic jump. Wisner et al. (1975) and Rabben et al. (1983) also developed air demand relations for hydraulic jumps in different cross-sections, which suggested that air demand in rectangular and circular pipes was quite different. Escarameia (2007) compared these existing data and indicated the downstream outlet conditions can substantially affect the air demand, but no detailed analysis was conducted, i.e. the effects of the outlet conditions on air demand were not systematically assessed. Even though the flow conditions and hydraulic jump types have been widely discussed in closed conduit flow, our knowledge on air flow demand under various submerged outlet depths is still limited.

Air vents allow air to enter a structure to ensure proper air supply and prevent structural damages or cavitation. Thus, the size of air vents must be sufficient to meet the air demand. The air vent design, such as its size and the loss coefficient, can influence the air demand in the closed conduit (Hohermuth et al. 2020). Currently, literature studies are limited regarding the relation between the size of air vent, the air demand, and the hydraulic jump behaviors (Falvey 1980; Tullis and Larchar 2011; Hohermuth et al. 2020). Hohermuth et al. (2020) also found that air demand increased with pipe length and decreased with pipe slope. Additionally, while the characteristics of a hydraulic jump and the air entrainment prediction within closed conduits or sewer systems have been studied (Chanson 1996; Unsal et al. 2008; Vos 2011; Ozkan et al. 2014), no specific attention has been paid to the effects of a submerged outlet. In this study, the influences of the submergence on the hydraulic jump characteristics and the air demand are investigated. Additionally, the characteristics of the hydraulic jump with limited air supply under a submerged outlet is also studied. This study will aid to predict the air demand and ensure the proper operation of hydraulic structures with a hydraulic jump in a closed conduit under various outlet conditions.

## 4.2. Experimental Program

Experiments of a hydraulic jump in a closed conduit with various outlet submergence levels were conducted in the T. Blench Hydraulics Lab at the University of Alberta. The experimental setup consisted of a 2 m long ($L$) horizontal perspex pipe with a diameter ($D$) of 0.20 m, a rectangular control gate with adjustable linear travel distance ($a$), and a water tank downstream of the pipe with an adjustable gate to control the outlet depth ($H$), as shown in Figure 4-1. To vary the Froude number, the size of the control gate opening ($a/D$) was varied. Note that the percentage of gate opening is the percent of gate linear travel distance rather than percentage of flow area. A gradually

varied flow profile of increasing flow depth downstream of the control gate was formed from the vena contracta ($h_0$) to the toe before the hydraulic jump ($h_1$). The hydraulic jump was recorded by a video camera at a speed of 30 frames per second and a resolution of $1920 \times 1080$ pixels for 30 s to determine the average distance from the jump toe to the pipe outlet ($L_p$) using an image processing tool as described below. A visual measurement using a tapeline from outside of the pipe was also made to validate $L_j$.

A vertical air vent of a diameter ($d_0$) of 50 mm was placed downstream of the control gate. Different sizes of nozzles were placed on the top of the air vent ($d = 7 - 25$ mm) to study the influence of constrained air supply on the characteristics of the hydraulic jump. Experiments were first conducted without a nozzle under 30% or 40% gate openings (Exp. A and Exp. B, respectively). Then various nozzle sizes ($d$) were placed on the top of the air vent with 30% gate opening (Exp. C). Details of these experiments are shown in Table 4-1.

Water was supplied by a pump, and flow rate ($Q_w$) was controlled by a gate valve and measured by a magnetic flow transmitter (Foxboro, I/A series, Schneider Electric Systems, France) with an accuracy of $\pm0.5\%$ of the full scale. The air velocity was measured on the top of the air vent using a hotwire air velocity transmitter (Omega, FMA 1000 series). Two points were selected when measuring the air velocity, one at the center, and the other at the half radius away from the center. Air velocities were recorded at a frequency of 2 Hz for more than 180 seconds. The air pressure inside the air vent was measured using a pressure transducer (Model 264 Differential Pressure Transducer, Setra Systems, Massachusetts) at the top, center, and bottom of the air vent (see Figure 4-1) at a frequency of 4 Hz for more than 300 seconds. The air pressure was then used to calculate the mean air velocity $U_{avg}$ and the air flow rate using the energy equation. The point air velocity measurements were used to compare with $U_{avg}$.

If a hydraulic jump was partially submerged and the air entrainment rate was low, a high-speed camera (Phantom v211, Vision Research, Wayne, New Jersey) was placed near the downstream end of the pipe to record the bubble movement and bubble size distribution for calculating the air demand. High-speed videos were taken at a speed of 200 frames per second for approximately 5 s with a resolution of 1280 × 800 pixels. Because it was difficult to directly capture every single bubble due to its overlap using the image processing tool, some bubbles were traced manually in Fiji (Fiji Is Just ImageJ, https://imagej.net/Fiji), which is a Java-based open source image processing program. The bubble shape was considered to be ellipsoidal, of which the major axis in the horizontal direction and minor axis in the vertical direction were measured directly from the image. The third axis perpendicular to the image plane (also in the horizontal direction) was assumed to equal the major axis, because the difference between the two horizontal axes is less than 10% (Liu et al. 2015).

## 4.3. Results and Discussions

### 4.3.1.  *Hydraulic Jumps in Circular Conduits*

Five flow regimes can be defined following the classification proposed by Sharma (1976) as illustrated in Figure 4-2. In Regime 1, the flow downstream of the control gate is free surface flow and no hydraulic jump is formed when the outlet depth $H$ (water depth above the invert of the pipe outlet) is sufficiently small. In Regime 2, a hydraulic jump is formed and followed by free surface flow with $H$ no more than $1D$. Under this flow regime, the jump is similar to a classical hydraulic jump with a surface roller and a bottom forward flow axially concentrated as a surface jet (Hager 1992). As $H$ increases, the hydraulic jump with a flow recirculation is followed by pressurized full-pipe flow, under which the downstream end of the roller is not confined within a closed

conduit (Regime 3a) or the roller is completely confined within a closed conduit (Regime 3b). In Regime 4, the hydraulic jump is partially submerged when the conjugate depth is larger than the pipe diameter. The flow characteristics and air demand of Regimes 3 and 4 need further investigation since they have not been fully investigated. When the hydraulic jump is fully submerged, the water level rises into the air vent pipe, and the flow in Regime 5 has no air entrainment.

The effects of the outlet depth ($H$) on the flow regime for Exp. A with $a/D = 30\%$ are shown in Figure 4-3(a). The Froude number of the flow is calculated at the vena contracta with $\mathsf{F}_0 = 8.5$, where $\mathsf{F}_0 = V_0/(gh_{0e})^{0.5}$, $h_{0e}$ = hydraulic depth at the vena contracta which is the division of the cross-sectional flow area by the water surface width, and $V_0$ = average water velocity at the vena contracta. When $H/D = 0.8$, a hydraulic jump was observed but the flow remained free surface within the pipe, indicating Regime 2 flow. When $H/D$ increased to between 1.0 and 1.75, a hydraulic jump was followed by pressurized flow in the pipe (Regime 3). In Regime 3a, under which $H/D = 1.0$ and 1.25, the downstream end of the return roller was not observed within the conduit as shown in Figure 4-3(b). When the distance from the toe of the hydraulic jump to the pipe outlet ($L_j$) increased and was longer than the roller length ($L_r$ in Figure 4-3b), a full turbulent roller was developed inside the pipe (Regime 3b), with $H/D = 1.5$ and 1.75. The measurements of $L_r$ were in the range of 4-4.5$D$, which were close to those of Mortensen et al. (2012) with a similar Froude number. Additionally, $L_r$ could also be reasonably predicted by the method of Stahl and Hager (1999) using the approach flow Froude number. When $H/D$ was 2.0 and 2.25, hydraulic jumps were partially submerged (Regime 4). The hydraulic jump is fully submerged without air entrainment for $H/D \geq 2.5$. Note that $L_j$ and $L_r$ are not only influenced by the pipe length, but also by the outlet depth, and the Froude number.

Downstream of the control gate, the water depth increased towards the hydraulic jump as a gradually varied flow. With increasing outlet depth $H$, the hydraulic jump was pushed towards the control gate, thus the depth at the toe of the hydraulic jump $h_1$ (see Figure 4-1) would increase. When $h_1$ equaled the depth at the vena contracta $h_0$, the jump was no longer a free jump (i.e., the flow regime was transferred from Regime 3b to Regime 4). The mean air pressure $P_1$ at the bottom of the air vent could drop below atmospheric pressure.

The depth at the toe of the hydraulic jump ($h_1$) in a circular horizontal closed conduit can be calculated by applying the momentum equation across the hydraulic jump when the downstream outlet is submerged for Regimes 3 and 4, the friction is assumed to be negligible compared to other terms in the equation (Chow, 1959):

$$\rho g A_1 \bar{h}_1 + \rho \frac{Q_w}{A_1} Q_w = \rho g A_2 \bar{h}_2 + \rho \frac{Q_w}{A_2} Q_w - P_1 A_2 \quad (4-1)$$

where $A_1$ is the cross-sectional flow area at the toe of the jump; $A_2 = \pi D^2/4$ is the flow area at the downstream end of the pipe; $\bar{h}_1$ and $\bar{h}_2$ are the distance from the water surface to the centroid of the up- and downstream sections of the hydraulic jump, respectively with $\bar{h}_2 = H - D/2$.

When $h_1 = h_0$, the critical Froude number at the vena contracta ($\mathsf{F}_{0c}$) can be used to determine whether the hydraulic jump is partially submerged using Eq. (4-1) by dividing with $gh_{e0}$:

$$\mathsf{F}_{0c}^2 = \left[ A_0 \bar{h}_0 - A_2 \left( \bar{h}_2 - \frac{P_1}{\rho g} \right) \right] \Big/ \left[ \left( \frac{A_0^2}{A_2} - A_0 \right) h_{e0} \right] \quad (4-2)$$

Under a specific outlet depth, the hydraulic jump will be partially submerged (Regime 4) if $\mathsf{F}_0$ is less than the critical value $\mathsf{F}_{0c}$ as shown in Figure 4-4(a, c). Otherwise, the hydraulic jump is not

submerged. The calculated $F_{0c}$ along with various outlet depths has a good agreement with the experimental data, as shown in Figure 4-4(a, c). Note that $F_{0c}$ increases with $H$, indicating that a hydraulic jump with a higher outlet depth needs a larger flow rate to remain unsubmerged.

Furthermore, a fully submerged hydraulic jump in a circular pipe can also be determined by applying the momentum equation (Eq. 4-1) between the control gate and the downstream end of the pipe. For a fully submerged hydraulic jump in a circular pipe, the hydrostatic pressure at the control gate can be calculated using the full-pipe flow depth $D$. The critical Froude number at the control gate $F_{ac}$, and the corresponding critical outlet depth, above which the hydraulic jump would be fully submerged, have a good agreement with the measurements as shown in Figure 4-4 (b, d). Therefore, the flow regimes can be determined using the momentum equation along with Figure 4-4.

### 4.3.2.  *Air Demand of Different Flow Regimes*

The air demand was determined by the vent pipe area and the mean air velocity, $U_{avg}$, which was calculated from the air pressure measured inside the air vent ($d_0$ = 50 mm) using the energy equation. The instantaneous air velocity ($U_a$) was calculated using the energy equation between the atmosphere and the point inside the air vent: $-P_i = \frac{1}{2}(1+K)\rho_a U_a^2$, where $P_i$ is the instantaneous air pressure at the top of the air vent, $\rho_a$ is the air density, and $K = 1$ is the local loss coefficient of the inward-projecting (re-entrant) entrance (Mott, 1994). The mean air velocity was calculated from $U_{avg} = (\int_0^T U_a dt)/T$, where $T$ = 300 s is the total measuring duration, and $dt$ is the time interval. A number of measurement duration $T$ were examined and the influence of $T$ on $U_{avg}$ can be neglected when $T > 240$ s. From the measurement of hotwire air velocity transmitter, the air velocity at the center of the air vent was about 3% - 22% higher than that at the half radius away

from the center, and the average velocity of these two points was about 7% - 14% less than $U_{avg}$. Overall, the mean air velocity $U_{avg}$ calculated from the air pressure is considered reasonable. Thus it was subsequently used to calculate the air flow rate ($Q_a$) and the relative air demand ($\beta = Q_a/Q_w$) in this study.

The air pressure behaviors were different at different locations in the air vent, as shown in Figure 4-5. When the Froude number at the vena contracta $F_0 = 8.5$ with $H/D = 1.5$, the mean air pressure was between -4.2 Pa and -3.8 Pa at different locations. However, the pressure transducer had an accuracy of $\pm 0.6$ Pa. The measured mean air pressure was similar at different locations, whereas the pressure fluctuation at the bottom of the air vent was much larger than that at the top. For instance, when the Froude number at the vena contracta $F_0 = 8.5$ with $H/D = 1.5$, the mean air pressure was between -4.2 Pa and -3.8 Pa at different locations, but the root mean square (RMS) of the air pressure was 6.8 Pa, 12.4 Pa, and 20.5 Pa at the top, center and bottom of the air vent, respectively. To exam the air pressure fluctuation difference on the top and bottom of the air vent, a CFD model was developed using a commercial code ANSYS CFX to solve the Reynolds-averaged Navier-Stokes (RANS) equations closed with standard $k$-$\varepsilon$ turbulence model. The size of the air vent in the computational domain was identical to that in the lab. At the inlet boundary (Figure 4-6a), the air pressure was specified as sinusoidal with a 50 Pa amplitude and a 2 Hz frequency. A box was added on the top of the air vent so that the atmospheric pressure specified on the box was far from the air inlet. Boundaries on the box were defined as opening at atmospheric pressure where air can move into or out of the domain. Other boundaries of the pipes and box were set as no-slip walls. The element size and node number were determined by mesh sensitivity that adapts and refined the meshes until no significant changes in the air velocity profile. The final number of the node used in the model simulation was 255 thousand. In the CFD model, the

pressure in the air vent was driven by the pressure fluctuation at the bottom with an amplitude of 50 Pa and a mean pressure of 0 Pa. Similar to the experimental measurements, the modeled air pressure on the bottom of the air vent has a much greater amplitude than that in the top (Figure 4-6b). The amplitude of the air pressure was damped to about 8% on the top of the air vent compared to that on the bottom. Similarly, the measured maximum positive pressure at the bottom of the air vent decreased from about 80 Pa to 9 Pa at the top (Figure 4-5). Thus, air pressure fluctuation at the bottom of the air vent was damped towards the top of the air vent, and the influence of air pressure fluctuation caused by the hydraulic jump can be neglected on the top of the air vent.

The measured air pressure was sometimes positive, as shown in Figure 4-5, indicating flow out to the atmosphere. A few tufts were placed on the top of the air vent during the experiment to indicate that the flow direction of the air was upward or downward. For instance, the direction of tuft became upward about every 2.2 s and stayed about 0.2 s before it changed downwards for $H = 1.5D$ with $F_0 = 8.5$, which was close to the cycle time (about 1.9 s) of air pressure changed from negative to positive (Figure 4-5). Note that the value of the upward air velocity was about 45% of the downward velocity, and the duration of the outward air flow was short (Figure 4-5). Overall, the measurements of pressure fluctuation compared reasonably with the tuft movement.

From the measurements with the air vent size $d_0 = 50$ mm, the relative air demand $\beta$ was found to be influenced by the outlet depth as well as the flow regime in the pipe, as shown in Figure 4-7. Note that for Regime 4, the air flow rate is small and individual air bubbles in the submerged pipe can be measured. Calculated from the bubble sizes and movements, the relative air demand was between 0.03% and 0.63%, which was in the similar range ($\beta = 0.03$-0.72%) with that obtained from the air velocity ($U_{avg}$) and the vent tube area. Thus, the measurement of air demand is reliable. Air demands in the experiments at various Froude number and outlet depths were compared with

the previous air demand prediction models in the literature, as shown in Figure 4-7(a). Previous models could only predict the air demand for free surface flow with or without hydraulic jump (e.g. Kalinske and Robertson, 1943; Sharma, 1976; and Hohermuth et al., 2020), but these equations could not reasonably predict the air demand at different outlet depths under the same $F_0$ (e.g., Regimes 3 and 4). Figure 4-7(b) indicates that for a low-level outlet the air demand in a free surface flow is higher than that of a submerged outlet at the same $F_0$. Clearly, $F_0$ is not the only governing parameter influencing the air demand in a closed conduit with a submerged outlet (Figure 4-7b). Therefore, it is necessary to improve the existing air demand prediction under various flow regimes.

In Regime 1 (supercritical free surface flow without a hydraulic jump), the free surface produces a drag force on the air mass above the water surface (Valero and Bung 2016). Because of the drag force on the air, the water velocity has a significant influence on the air velocity (Campbell and Guyton 1953). Although the air demand in Regime 1 was not measured in this study, Sharma (1976) proposed a linear curve to predict its relative air demand in Regime 1 ( $\beta = 0.09F_0$) based on the Froude number at the vena contracta. Hohermuth et al. (2020) also proposed an equation for estimating the air demand in Regime 1 ($\beta_1$) incorporating effects of tunnel length and air vent loss coefficient:

$$\beta_1 = 0.037{F_0}^{1.3} \left( \frac{A_d}{A_D(\zeta + 1)^{0.5}} \right)^{0.8} \left( \frac{L}{D} \right)^{0.25} \quad (4-3)$$

where $A_d$ = cross-section area of the air vent, and $A_D$ = cross-section of the pipe, $\zeta$ is air vent loss coefficient. Figure 4-8(a) compares the air demand for Regimes 1 and 2 with the existing equation proposed by Sharma (1976), Hohermuth et al. (2020), and Kalinske and Robertson (1943). Note

that the significantly larger air demand in Regime 1 calculated from Sharma (1976) is likely due to its larger air vent and longer tunnel.

In Regime 2, there is a hydraulic jump followed by free surface flow, and the relative air demand $\beta_2$ can be well predicted by the equation proposed by Kalinske and Robertson (1943), as shown in Figure 4-8(a).

$$\beta_2 = 0.0066(F_0 - 1)^{1.4} \quad (4-4)$$

However, Eq. (4-4) only applies in predicting the relative air demand in a closed conduit with a free surface outlet ($H < D$). The relative air demand in a free surface low-level outlet (Regime 2) is higher than that of a submerged outlet (Regime 3 and 4), as illustrated in Figure 4-7(b).

When the outlet depth $H$ is greater than $1D$ (Regime 3), the hydraulic jump is followed by pressurized pipe flow ($H > D$ and $F_0 > F_{0c}$). It is found that the relative air demand in Regime 3a $\beta_3$ starts decreasing from $H = D$ until the flow becomes Regime 3b, under which the air demand is independent of the outlet depth. Therefore, the relative air demand in Regime 3a can be calculated from Eq. (4-4) by adding a new term determined by $F_0$ and $H/D$:

$$\beta_3 = \beta_2 - \frac{K_1 \left(\frac{H}{D} - 1\right)}{F_0 - 1} \quad (4-5)$$

where $K_1$ is the dimensionless coefficient for Regime 3a. If $L_r < L_j$, the flow is in Regime 3b, and the relative air demand is not changed by $H$. At $K_1 = 0.294$, the calculated relative air demands have a good agreement with the experimental data of Regime 3, as shown in Figure 4-8(b). The physics of the air demand will be discussed later in this section.

For Regime 4 where the hydraulic jump is partially submerged ($H > D$ and $\mathsf{F}_{ac} < \mathsf{F}_0 < \mathsf{F}_{0c}$), air bubbles are mainly entrained by the breaking of the surface roller instead of by the advective diffusion region (Rajaratnam 1967; Takahashi and Ohtsu 2017). Therefore, the relative air demand is significantly decreased compared with the other two regimes, as shown in Figure 4-7(b). In this case, a correction factor $K_2/(\mathsf{F}_0 - 1)^2$ was added to develop the prediction equation. Therefore, the prediction equation for the relative air demand in Regime 4 $\beta_4$ can be written as:

$$\beta_4 = \frac{K_2\beta_3}{(\mathsf{F}_0 - 1)^2} \quad (4-6)$$

where $K_2 = 4$ is model coefficient fitted from the experimental data. Figure 4-8(c) compares the predicted and measured air flow rates in Regime 4. Note that the relative air demand in Regime 4 was very low, which can be neglected in many predictions and applications. However, even a small amount of relative air demand can lead to a severe air supersaturation and fish kills as discussed in Li et al. (2020), where about 0.4% relative air demand generates harmfully high air supersaturation in the water downstream of a low-level outlet. Therefore, the relative air demand prediction in Regime 4 is still important even at a small value of less than 1%.

The physics of the air entrainment and bubble transport in various flow regimes are discussed here. From experimental measurements, $L_j$ and $L_r$ are strongly affected by the outlet depth ($H$). When air is entrained in the jump, it is subsequently either transported downstream or detrained in the roller, as shown in Figure 4-9. As suggested by Takahashi and Ohtsu (2017), the air concentration distribution in the return roller is nearly independent of the hydraulic jump location if the jump is unsubmerged. When the outlet depth is relatively low (e.g., $H = 1.25D$ and $\mathsf{F}_0 = 8.5$, Regime 3a), the downstream roller end is not within the conduit as illustrated in Figure 4-9a, indicating that the roller is not fully developed in the pipe. Entrained air bubbles that typically recirculate within the

roller are released immediately at the pipe outlet to the water tank rather than being detrained to the upstream air pocket. As the outlet depth increases, the jump moves upstream. The length of the roller in the pipe also increases, causing more entrained air bubbles to recirculate within the roller rather than being released downstream. Bubbles recirculated in the roller would eventually be released upstream through the roller front (Skartlien et al. 2012). Therefore, more entrained air is detrained as the outlet depth increases.

When the outlet depth increases, e.g., to $H = 1.75D$, $L_j$ is sufficiently long for a fully developed roller to form, as shown in Figure 4-9(b). For flow conditions in Regime 3b, the whole return roller is formed within the pipe and $L_r$ barely changes, the same phenomenon is also observed by Mortensen et al. (2012). Thus, there is no major difference in the amount of entrained air transported upstream and terminated with detrainment under Regime 3b with various $H$ (Figure 4-7b). Additionally, flow with a high Froude number entrains more air, and creates smaller bubbles due to more energetic rollers, results in reduced air detrainment (Schulz et al. 2020). Flow characteristics and hydraulic jump locations are influenced by the pipe diameter, length, and slope, which suggests the measured air demand and proposed prediction equation are likely specific to the geometry used in this study. Scale effects will be discussed in later section. Overall, increasing the high outlet depth leads to the increase of the length of both $L_j$ and $L_r$, which would enhance the air detrainment and lead to a smaller $\beta$.

### 4.3.3. *Hydraulic Jump with Limited Air Supply*

Sufficient air supply through air vents is needed to maintain the air pressure and to reduce potential structural damage or operational issues. To investigate the effects of constrained air inflow on the characteristic of a hydraulic jump in the submerged conduit, a nozzle of various sizes was placed

on the top of the air vent ($d$ = 7, 10, 15, 20, and 25 mm) in the experiments to control the air supply. The submerged outlet depth was $H$ = 1.5$D$ and $\mathsf{F}_0$ = 8.5 with a gate opening $a/D$ of 30% (Exp. C in Table 4-1). Figure 4-10 illustrates the hydraulic jump under a different amount of air supply. The hydraulic jump characteristics appeared to be identical when $d/d_0$ was larger than 0.3, below which the jump moved upstream. Due to the reduced sub-atmospheric air pressure $P_1$ as shown in Fig 4-11(a), the jump was pushed upstream. From Eq. (4-1), a negative $P_1$ can be regarded as an increase in the outlet depth $H$. The effect of $P_1$ can be accommodated by adjusting $\bar{h}_2$ (the distance from the water surface to the centroid of the water flow cross-section at the pipe outlet, defined in Eq. 4-1) by an amount of $-P_1/(\rho g)$ in the tailrace: $\bar{h}_2{'} = \bar{h}_2 - P_1/(\rho g)$. Note that $-P_1/(\rho g)$ increases with decreasing $d_0$, as shown in Figure 4-11 (a). The roller length with limited air supply ($d/d_0$ = 0.2, $L_r$ = 4.9$D$) was longer than that with unconstrained air supply ($L_r$ = 4.0$D$). As $d/d_0$ was reduced to 0.14, the bubbly flow became more transparent compared to that with unconstrained air supply as shown in Figure 4-10(d), indicating that the quantity of bubbles in the water was reduced.

Similarly, the relative air demand decreased dramatically when $d/d_0$ was less than 0.3 as illustrated in Figure 4-11(b). This is because the air supply was restricted by the high air vent loss and a small air vent opening. When the air supply was limited, the magnitude of the negative air pressure $P_1$ further increased and the hydraulic jump was pushed upstream or became partially submerged, which was similar to that of increasing outlet depth. $\beta$ can be predicted using the developed equation in this study using the modified outlet depth ($\bar{h}_2{'}$). Figure 4-11(b) illustrates that the measured and predicted $\beta$ have a good agreement at different $d/d_0$, which indicates modified outlet depth $\bar{h}_2{'}$ can be used to predict $\beta$ when the air supply is constrained.

Air removed by the hydraulic jump results in a sub-atmospheric pressure in the air pocket upstream

72

of the jump, and the air demand through the air vent. The air pressure inside the pipe can be assessed based on the air demand, air vent diameter and loss coefficient. Air vent loss coefficient $\zeta$ (based on the air velocity at the nozzle) for various relative nozzle size $d/d_0$ is shown in Figure 4-11(c). Note that the loss coefficient for an orifice plate is determined by the orifice opening size, which can reach about 20 when the orifice opening is 30% of the pipe size (Potter and Wiggert 2016; Hohermuth et al. 2020). In this study, a nozzle of different sizes was placed on the top of the air vent. The energy loss was mainly caused by the re-entrant loss and the sudden expansion loss following the nozzle. When there was no nozzle placed on the top of the air vent ($d/d_0 = 1$), the air vent loss coefficient is 1.0, reflecting only re-entrant loss as reported in Mott (1994). With a nozzle, the flow at the nozzle expands into the air vent pipe ($d_0$), leading to an additional sudden expansion loss. The pipe sudden expansion loss can be estimated analytically as $(1-d^2/d_0^2)^2$. Thus there is no expansion loss when $d/d_0 = 1$, and it increases to 1.0 when $d/d_0 = 0$. The air vent loss coefficient $\zeta$ (based on the air velocity at the nozzle), which can be considered as the summation of the re-entrant loss and the sudden expansion loss, increased from 1.0 to about 2.0 when $d/d_0$ decreased from 1 to 0.14 (Figure 4-11c). The above estimate of the loss coefficient is used to calculate the air velocity at the nozzle. The calculated air velocity has a good agreement with the anemometer measurements (Figure 4-11c), indicating the reliable prediction of the loss coefficient.

The air velocity at the nozzle also changes with decreasing nozzle size, and eventually became stable around 25 m/s for $d/d_0 = 0.14$, as shown in Figure 4-11(c). In this study, whistling started when the air velocity exceeded 25 m/s ($d \leq 1$ cm). Note that the nozzle and its expansion is likely one of the reasons enhanced the whistling. Falvey (1980) proposed that the whistling sound occurs when air velocity exceeds 30 m/s. Thus it is recommended that special attention should be paid to whistling noise when the air velocity in an air vent is larger than 25 m/s. Note that an air velocity

higher than the recommended limit without whistling noise has been reported in prototypes and larger models. Associated with a high air velocity, one should also pay attention to possible sub-atmospheric pressure, significant compressibility effects or damage of hydraulic structures.

The characteristics of the hydraulic jump and air pressure inside the pipe was also monitored when the air vent was suddenly sealed ($d/d_0 = 0$). When the air vent was fully sealed at $t = 10$ s, the air pressure oscillated and decreased from about zero to about -1400 Pa (Figure 4-12a), which caused the hydraulic jump to move upstream. The mass of the air pocket at different times was estimated from the images of the air pocket size and the measured pressure assuming the ideal gas law. After the air vent was sealed, $\beta$ is calculated from the estimated decrease of the mass of the air pocket as shown in Figure 4-12(b). $\beta$ kept between 5% to 8% in the first 10 s after sealing the air vent ($t = 10 - 20$ s), and then decreased significantly to about 0.1%. After the air vent was sealed, the reduction of $\beta$ from normal to about zero would take about 20 s (Figure 4-12b). The hydraulic jump flow regimes at different times after sealing the air vent are illustrated in Figure 4-12(c). Due to the closed air vent, air mass in the air pocket was entrained into the hydraulic jump and transported downstream, contributing to the decreased air mass in the air pocket. The air pocket volume and pressure kept falling until $t = 31$s, as shown in Figure 4-12(a). Later, the white water in the pipe became relatively clear ($t = 150$ s), suggesting that less air was transported downstream.

Although the air vent was sealed, some air bubbles were observed to be continuously transported downstream, and the flow did not transit to a completely drowned hydraulic jump even after the experiment ran 20 minutes, as shown in Figure 4-12(c). One possible reason for the source of this small amount of air is that the low air pressure results in the decreased dissolved gas concentration from 100% saturation to about 98% with some air bubbles released into water. Using the air-water mass transfer model (Li et al. 2020) and assuming the mass of dissolved air could be fully

transferred to the gas phase due to the decreased solubility, the calculated air void ratio (0.042%) was close to the measurement data (0.063%).

### 4.3.4. *Prototype Application and Scale Effects*

It was reported that the low-level outlets at the Hugh L. Keenleyside Dam (HLK), British Columbia, Canada, can cause supersaturation of total dissolved gases (TDG). To investigate its reason and evaluate the generation of TDG from the operation of the rectangular low-level outlet gates, fieldwork was carried out from July 13 – 16, 2020. The length of the closed conduit is 17.1 m with a width of 6.1 m and a height of 8.0 m. The slope of the closed conduit is 14.8°. The air entrainment into the low-level outlet mainly comes from the gate hoist room, which is connected with the atmosphere through windows as shown in Figure 4-13(a). Spot measurements of air velocity were taken on the top of the gate well using a hotwire velocity meter (TSI Alnor 9535-A) in the low-level machinery room during the fieldwork. The size of the gate well is 5.9 m × 2.7 m, and a platform equipped with ropes for lifting the gate was placed on the edge of the top of the gate well. Spot measurements of air velocity were taken at four different points. The air velocity was recorded for one minute with a one-second interval at each measurement point. Additionally, five SmartReaders (Plus 4, 2-channel pressure and temperature data logger, ACR Systems) were used to continuously measure the differential pressure between the top of the gate well and inside at different depths (2 m, 4 m, 6 m, 8 m, and 10 m) in the low level machinery room. However, the pressure difference was too small to be accurately measured.

In the low-level outlet of the HLK dam, the flow is in Regime 4 and $\beta$ can be calculated using the developed Eq. (4-6) based on lab measurements. Overall, the predicted $\beta$ has a similar trend as the field measurements, and both give relative low air demands ($\beta < 1\%$) as illustrated in Figure 4-

13(b). The difference between the prediction and the measurement is noticeable at small gate openings. This is likely caused by the measurement uncertainties due to the low velocity in Regime 4 in both the lab and the field measurements. Additionally, there could be scale effects, but likely not significant. In general, the air demand prediction using Eq. (4-6) in Regime 4 can provide a reasonable estimate for the air demand in the prototype.

Sakhuja et al. (1984) and Hohermuth et al. (2020) studied scale effects for a model with a scale of 5-20 of a prototype low-level outlet and reported an underestimation of 4-19% for the relative air demand in free-surface flows (Regime 1). In Regime 2 (free surface flow with a hydraulic jump), Chanson and Gualtieri (2008) reported that the relative air demand in a small-scale model (1:2) was underestimated by about 45-60%. When a hydraulic jump is completely confined within a closed conduit (Regime 3b), Mortensen et al. (2011) found that the air demand is independent of the pipe size. Note that the pipe diameter used in their study was between 76 and 591 mm, whereas the pipe diameter in this study is 200 mm. Additionally, our air demand in Regime 3a-b ($\beta = 2$ - 14%) is similar to that measured in Mortensen et al. (2012) with $\beta = 0$ - 20%. Thus, air demand is not sensitive to the pipe sizes in Regime 3 for the tested size range. From the comparison between the field measurement at the HLK Dam and model prediction of the air demand in Regime 4 (Figure 4-13b), the air demand model prediction appears to provide a good estimate for the prototype.

In Regime 1, the air demand is directly affected by the surface turbulence of the water flow, which likely has scale effects. The relative air demand in Regime 2 is influence by both the water surface turbulence and turbulent shear layer generated by the hydraulic jump at the air-water interface. When the outlet of the conduit is submerged and the hydraulic jump is fully developed, the relative air demand is not sensitive to the water surface turbulence. The turbulence will be damped when

the hydraulic jump is submerged, leading to the relative insignificant scale effects on the relative air demand. Therefore, the scale effects appear to exist in Regimes 1 and 2, likely not sensitive to the pipe sizes in Regime 3 in the test range. From field measurement, the scale effect appears to be unimportant in Regime 4.

## 4.4. Conclusions

Regimes of supercritical flow with and without a hydraulic jump in a closed conduit were investigated in order to predict air demand for different outlet depths. Regime 1 is the free surface flow without a hydraulic jump, in which the relative air demand ($\beta = Q_a/Q_w$) was estimated to be $\beta$ = 36 - 90% with Froude number upstream of the jump $\mathsf{F}_0$ = 4 − 10. Regime 2 represents a hydraulic jump followed by free surface flow, for which the relative air demand depends only on Froude number $\mathsf{F}_0$. Regime 3 describes the hydraulic jump followed by pressurized pipe flow with an undeveloped or fully-developed return roller. The relative air demand is between 3% and 14%, and decreases with increasing roller length until the return roller is fully developed in the pipe. Regime 4 gives an air demand significantly smaller than 1% due to the partially submerged hydraulic jump. The air demand was also measured in a prototype low-level outlet of a dam with a partially submerged hydraulic jump, which was consistent with the developed prediction equation based on experimental measurements.

It was found that the mean air pressure was similar at different locations in the air vent, but the pressure fluctuation at the bottom of the air vent was much larger than that at the top. Additionally, various sizes of nozzles on the top of the air vent were tested to investigate the influence of air demand on the hydraulic jump. Limited air supply caused a negative air pressure, and the magnitude of the sub-atmospheric pressure significantly increased after sealing the air vent. The

hydraulic jump was pushed upstream with decreasing air demand due to the reduced air pressure in the closed conduit. Furthermore, the air vent loss coefficient increased with the decreasing nozzle size, and can be simplified as the addition of the re-entrant loss and the sudden expansion loss when the relative nozzle size $d/d_0$ is less than 1. The scale effects appear to exist in Regimes 1 and 2 due to the surface turbulence of the water flow. From laboratory and field measurement, the scale effect appears to be unimportant in Regime3 and 4. This study improves the general understanding of the air demand of a hydraulic jump with a submerged outlet to ensure the proper design and operations of urban sewer system and hydropower facilities. In the future study, the influence of pipe diameter, length, and slope on flow characteristics and air demand in a submerged closed conduit will be investigated.

## Notation

The following symbols are used in this paper:

$A_1$ = cross-sectional flow area at the toe of the jump;

$A_2$ = cross-sectional flow area at the downstream end of the pipe

$a$ = gate opening (linear travel distance);

$D$ = pipe diameter;

$d$ = nozzle diameter;

$d_0$ = air vent diameter;

$F_0$ = Froude number at the vena contracta;

$F_{0c}$ = critical Froude number at the vena contracta;

$F_{ac}$ = critical Froude number at the control gate;

$g$ = gravity acceleration

$H$ = water depth above the invert of the pipe outlet;

$h_0$ = water depth of the vena contracta;

$h_1$ = water depth of the toe before the hydraulic jump;

$h_{0e}$ = hydraulic depth at the vena contracta;

$K$ = local loss coefficient of the re-entrant entrance;

$K_{1, 2, 3}$ = dimensionless coefficient;

$L$ = pipe length;

$L_j$ = distance from the jump toe to the pipe outlet;

$L_r$ = roller length;

$P_i$ = instantaneous air pressure;

$P_1$ = mean air pressure at the bottom of the air vent;

$Q_a$ = air flow rate;

$Q_w$ = water flow rate;

$T$ = total measuring duration;

$U_a$ = instantaneous air velocity;

$U_{avg}$ = mean air velocity;

$V_0$ = average water velocity;

$\beta$ = relative air demand $Q_a/Q_w$;

$\zeta$ = Air vent loss coefficient;

$\rho_a$ = air density

Table 4-1 List of experiments of the hydraulic jump in the pipe.

| Experiments | $D$ (m) | $d$ (mm) | $a/D$ | $Q_w$ (L/s) | $F_0$ | $H/D$ |
|---|---|---|---|---|---|---|
| A | 0.2 | 50 | 30% | 15 - 30 | 5.1 - 10.2 | 0.6 - 3.0 |
| B | 0.2 | 50 | 40% | 15 - 30 | 2.9 - 5.8 | 0.7 - 2.25 |
| C | 0.2 | 0 - 50 | 30% | 25 | 8.5 | 1.5 |
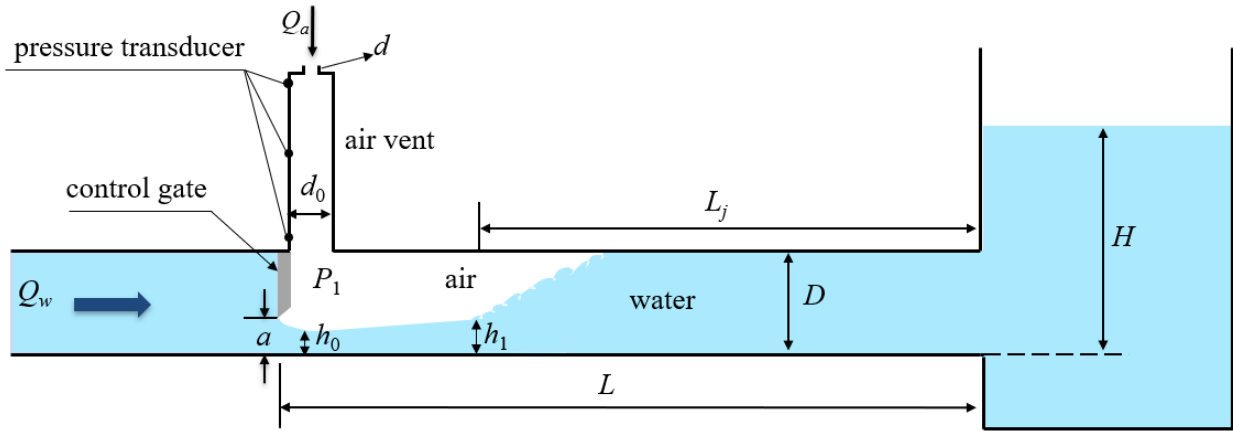
Figure 4-1 Schematic of the experimental setup.
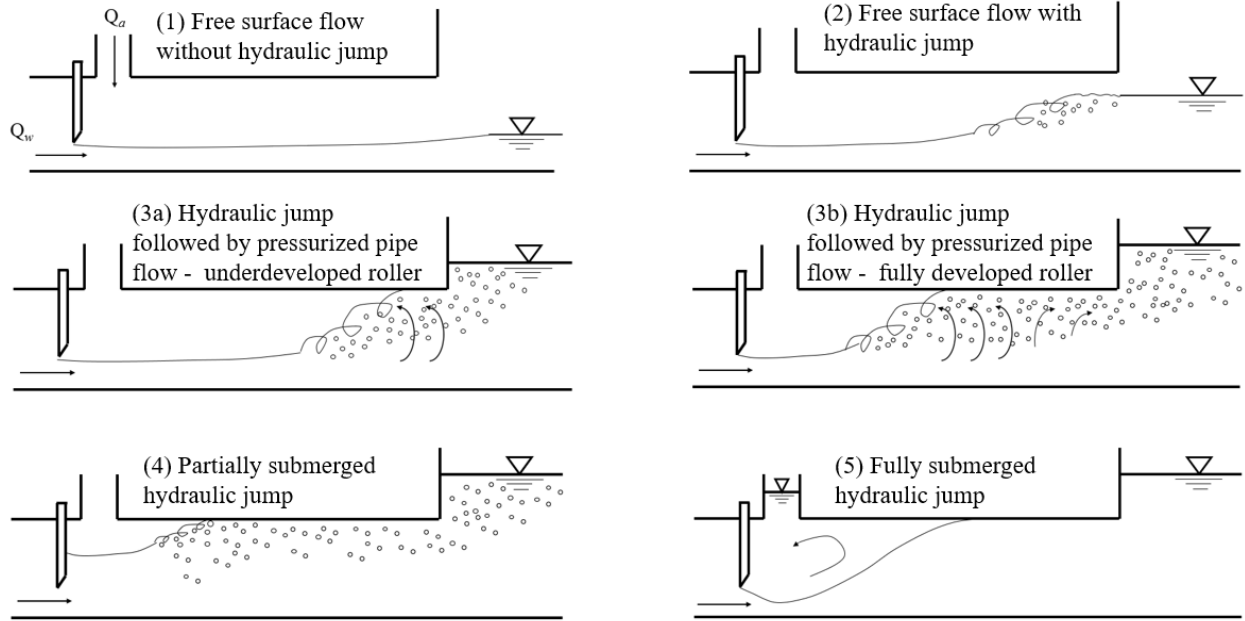
Figure 4-2 Different flow regimes in the pipe.
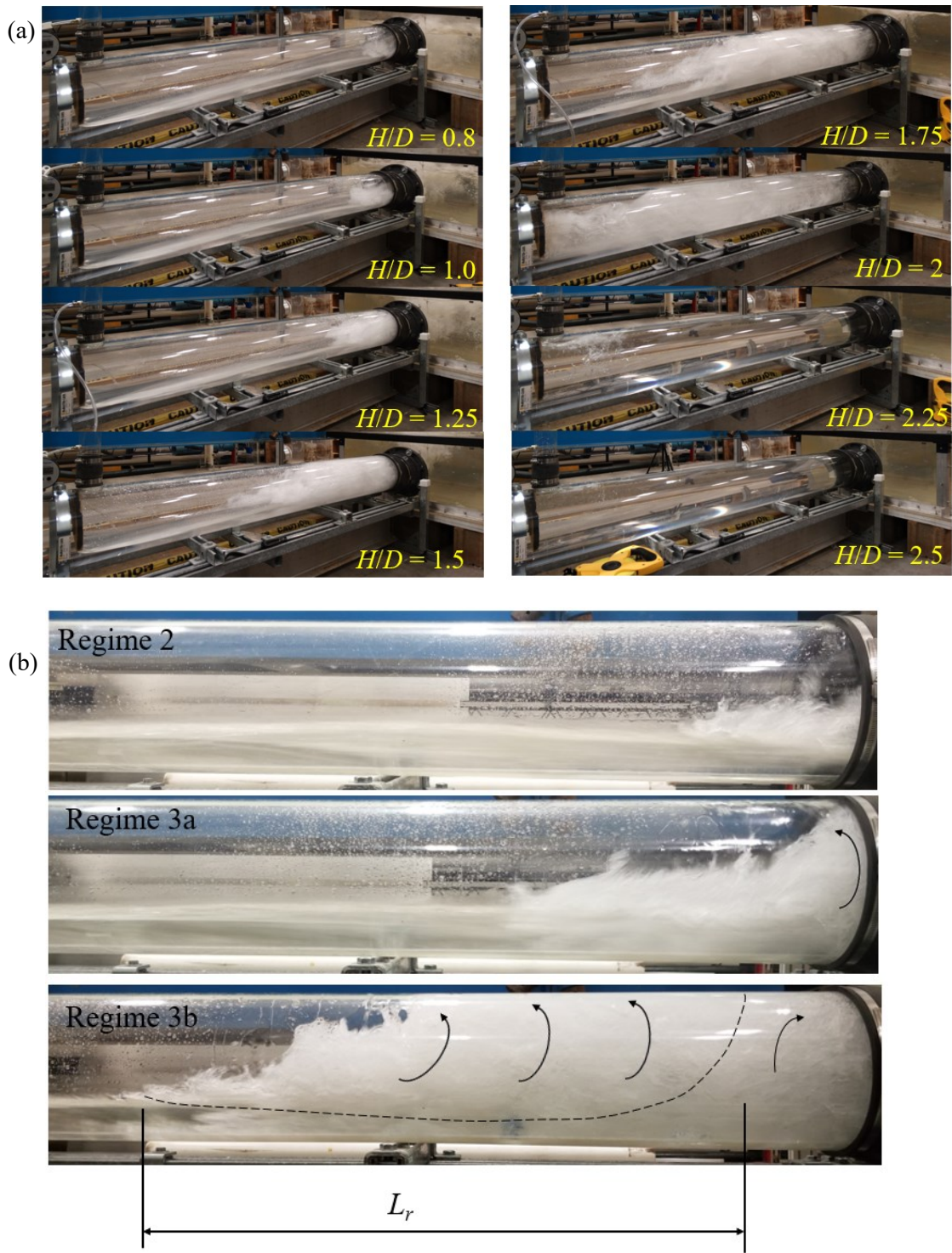
Figure 4-3 (a) Hydraulic jumps with various tailwater depths with $F_0 = 8.5$ and $a/D = 30\%$; (b) photos of Regime 2 and Regime 3.
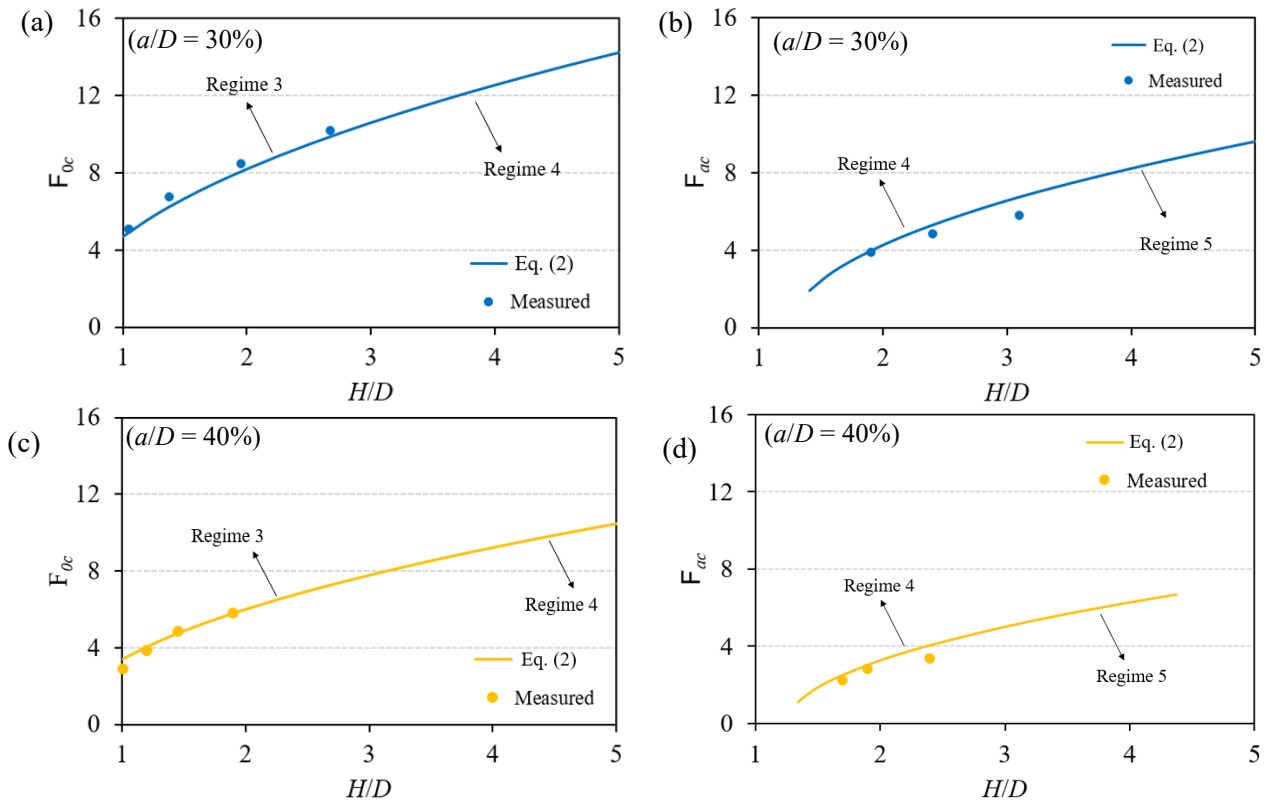
Figure 4-4 Froude number under a specific submerged water depth in a circular closed conduit with (a, b) $a/D = 30\%$, and (c, d) $a/D = 40\%$ (assuming $P_1$ is neglected).
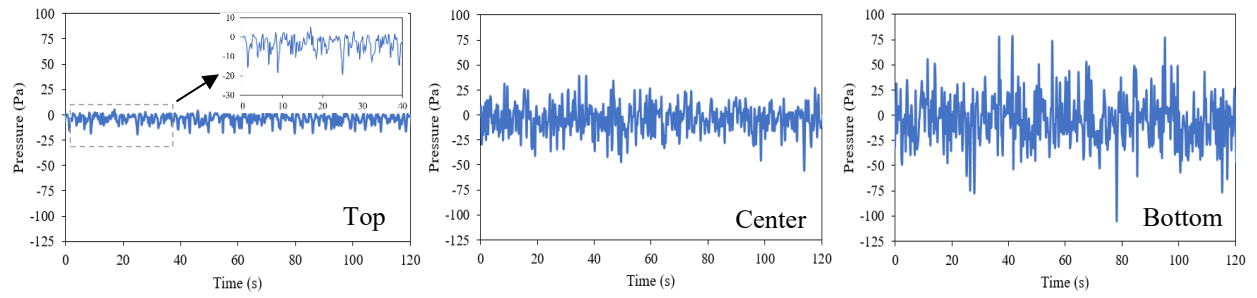
Figure 4-5 Measured air pressure at different locations of the air vent with $F_0 = 8.5$ under $H/D = 1.5$.
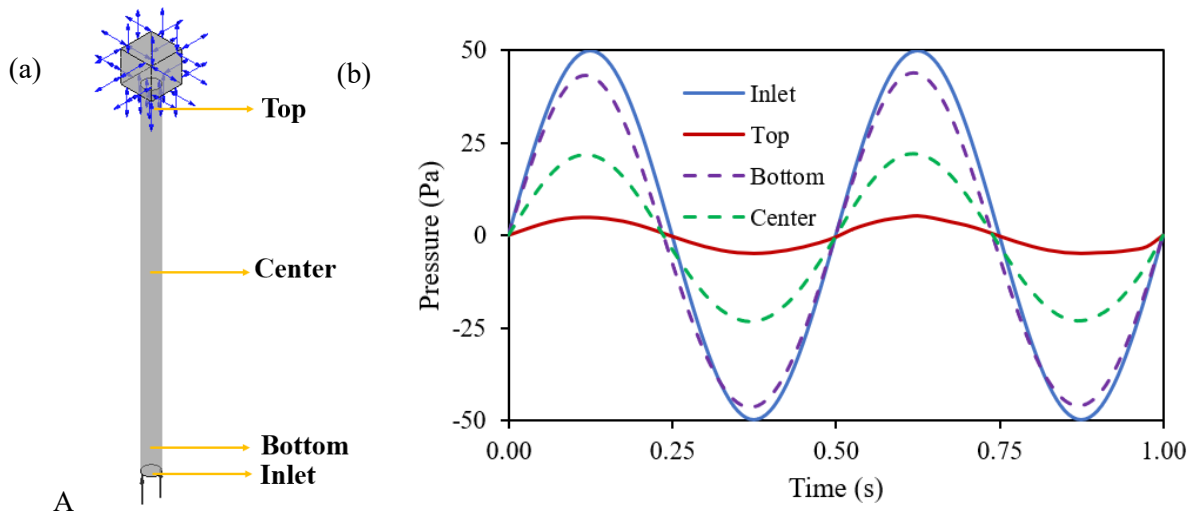
Figure 4-6 (a) CFD model setup for the air vent; and (b) modeled air pressure at different locations

of the air vent.
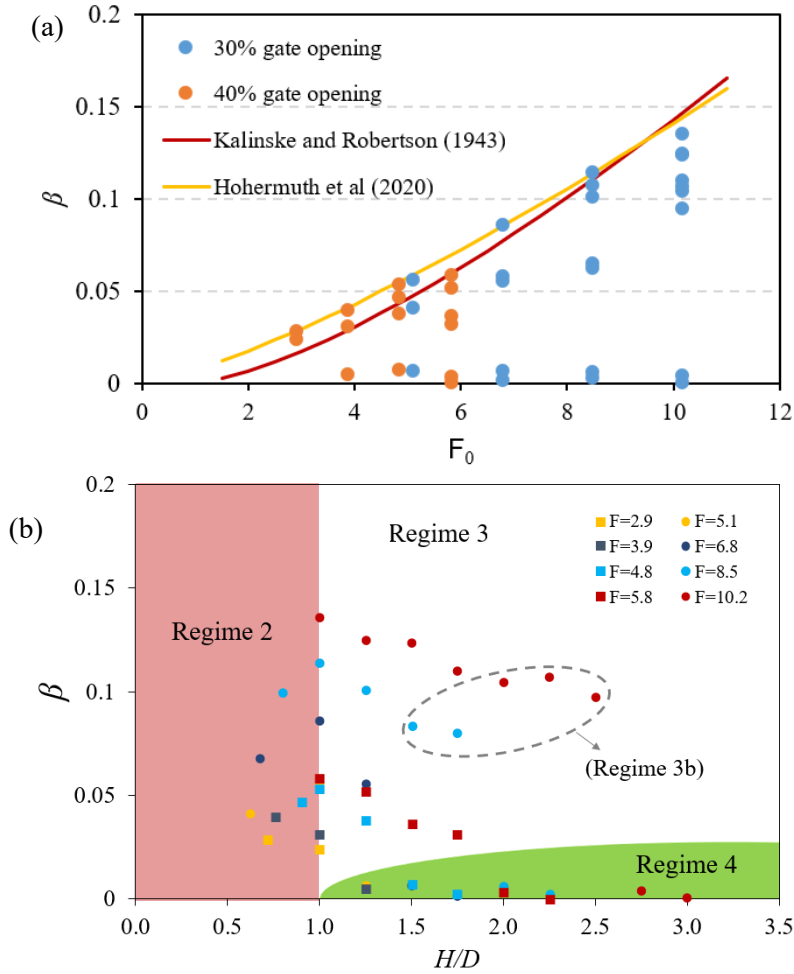
Figure 4-7 (a) Comparison of the measured air demand $\beta$ for Regimes 2-4 as a function of Froude number with previous prediction equations; and (b) effects of tailwater depth on $\beta$ with 30% gate opening (circle) and 40% gate opening (square) for Regimes 2-4 (Regime 5 has no air demand).
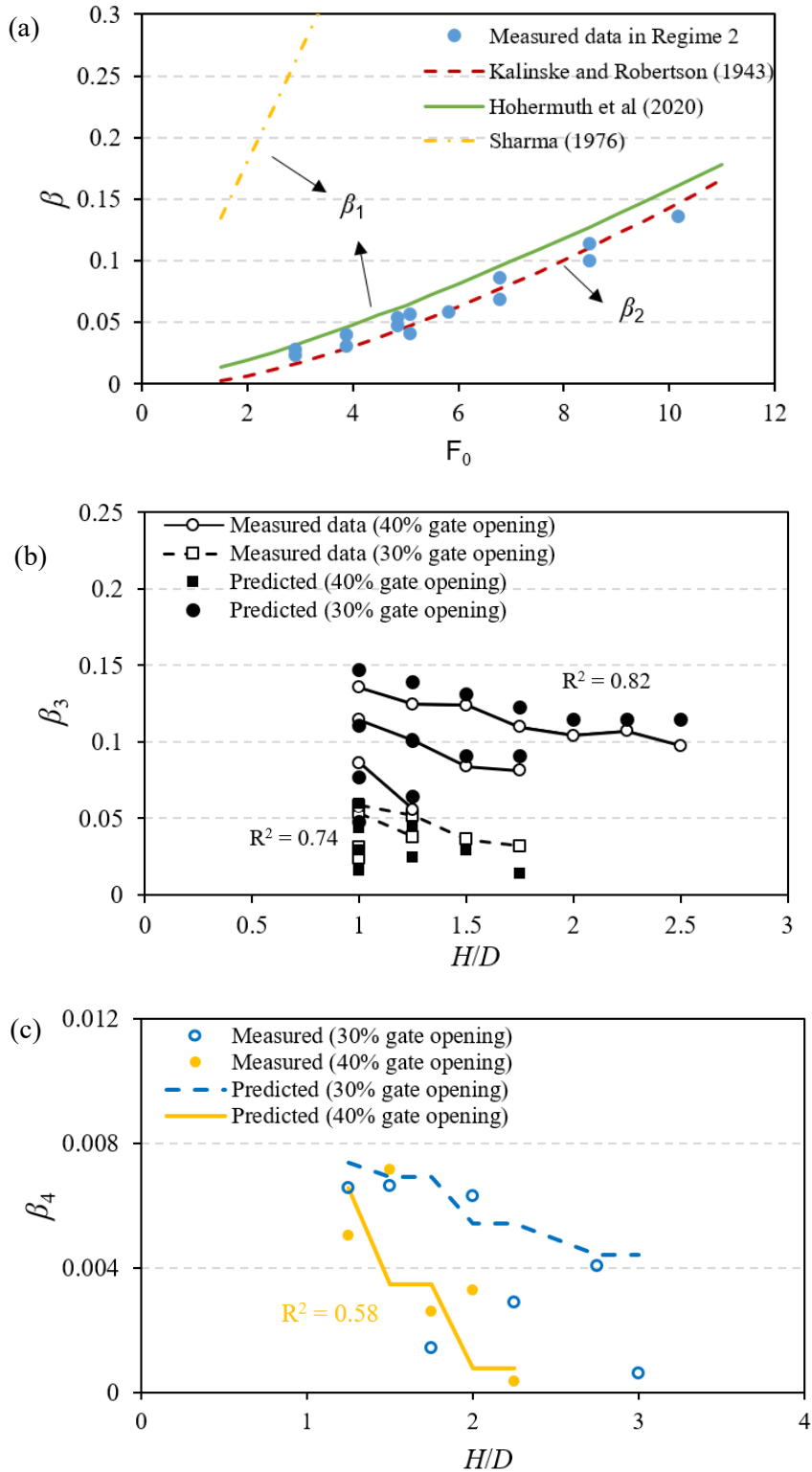
Figure 4-8 Relative air demand under (a) Regime 1 and 2; (b) Regime 3; and (c) Regime 4.
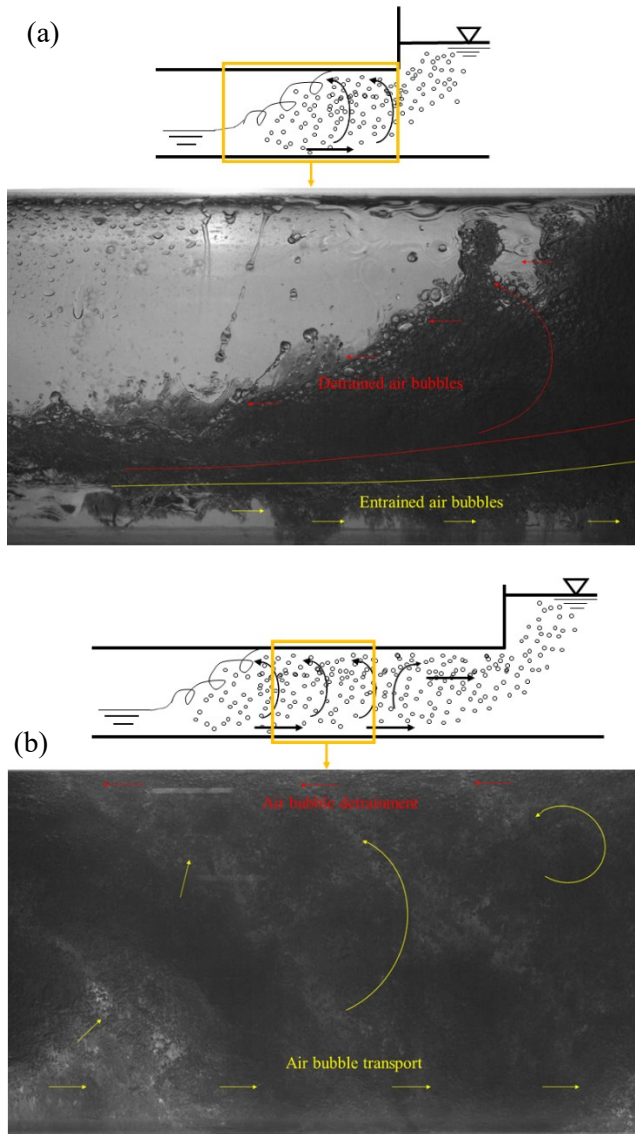
Figure 4-9 Entrained air bubble transport with (a) $H = 1.25D$; and (b) $H = 1.75D$. Data for $F_0 = 8.5$ and $a/D = 30\%$.
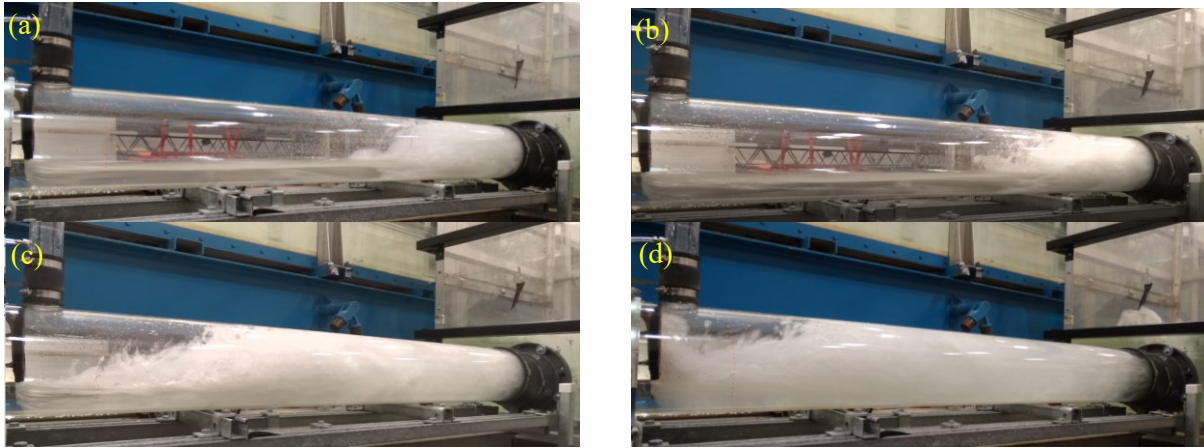
Figure 4-10 Hydraulic jumps with different air supply: (a) $\beta = 8.7\%$ ($d/d_0 = 0.5$); and (b) $\beta = 8.2\%$ ($d/d_0 = 0.3$); (c) $\beta = 5.9\%$ ($d/d_0 = 0.2$); and (d) $\beta = 2.1\%$ ($d/d_0 = 0.14$). Data for $F_0 = 8.5$, $a/D = 30\%$, and $H = 1.5D$.
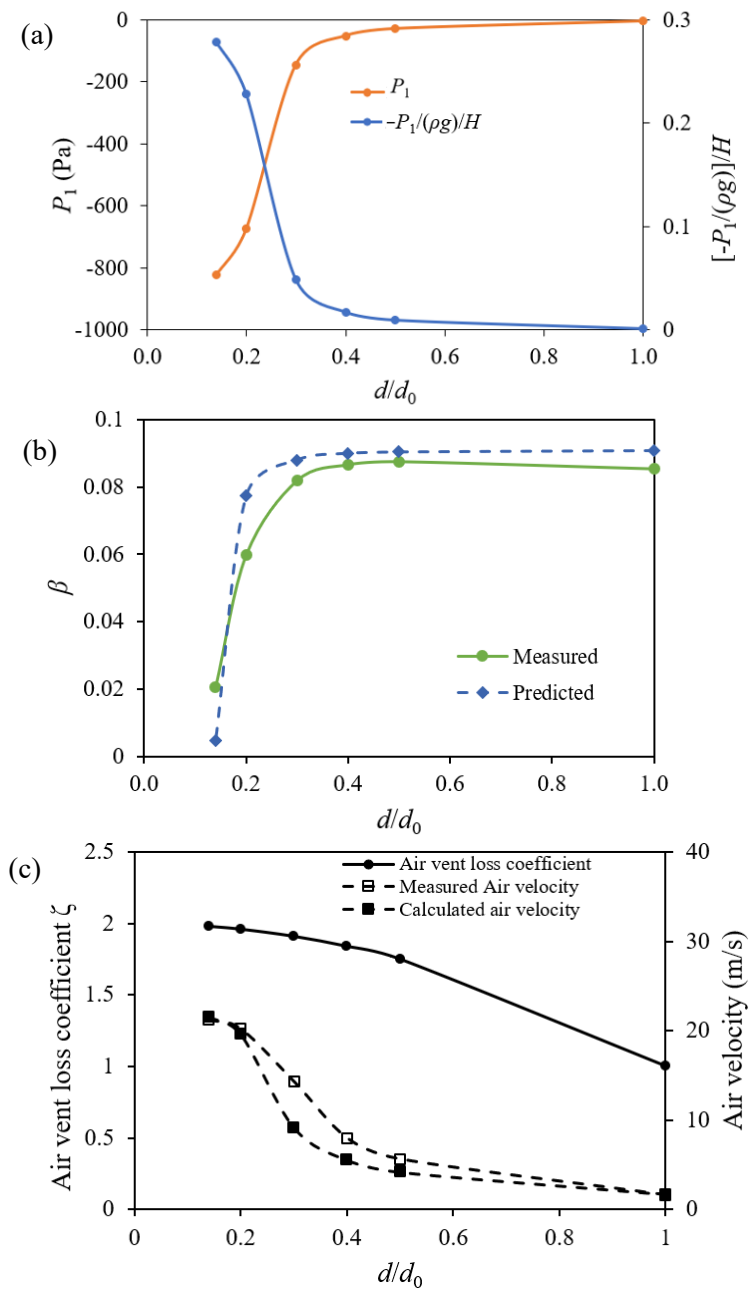
Figure 4-11 (a) air pressure; (b) relative air demand $\beta$; and (c) air vent loss coefficient $\zeta$ with various nozzle sizes. Data for $F_0 = 8.5$, $a/D = 30\%$, and H = 1.5D.
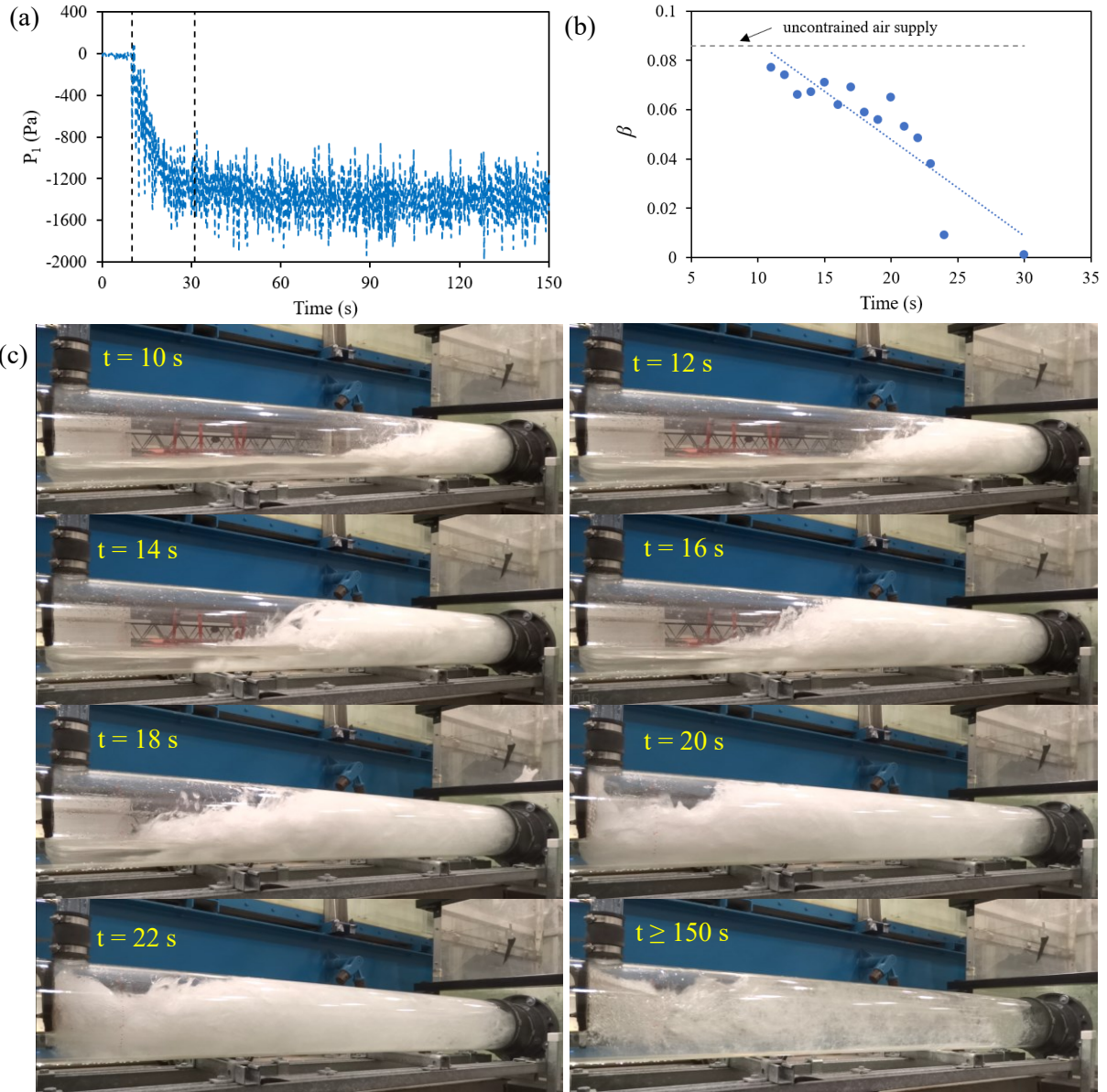
Figure 4-12 (a) Air pressure; (b) air demand; and (c) hydraulic jump patterns after sealing the air vent. Data for $F_0 = 8.5$, $a/D = 30\%$, and $H = 1.5D$.

(a)

hot wire anemometer

Gate hoist room

window

air

Forebay

Operating Gate

water

$H = 12.1$ m

Tailrace

8.0 m

17.1 m

$\theta = 14.8°$

(b)
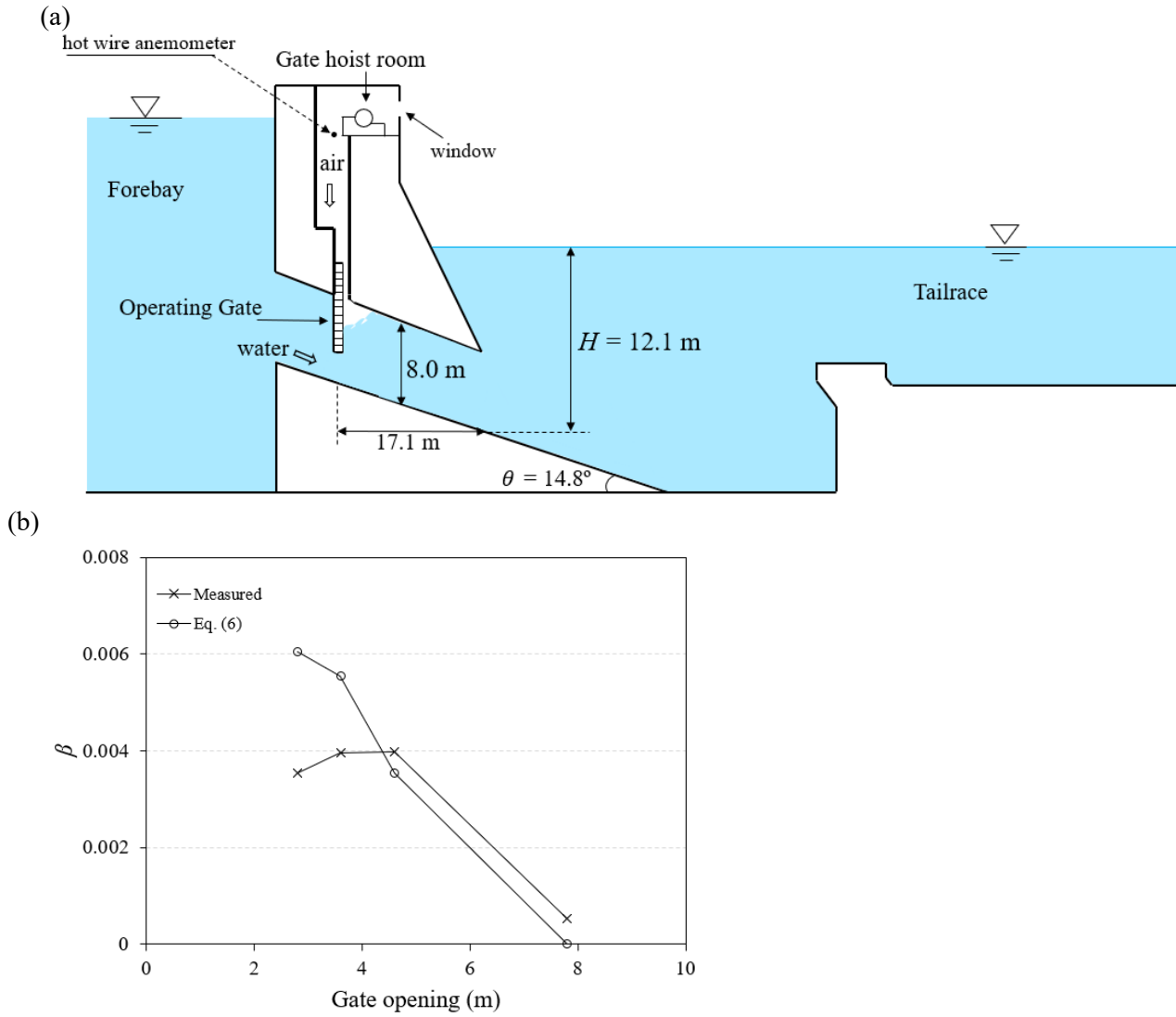
Figure 4-13 (a) Cross-section of the low-level outlet in Hugh Keenleyside Dam; (b) relative air demand $\beta$ under fieldwork conditions.

# 5. Generation of Supersaturated Total Dissolved Gases of Low-level Outlets[*]

## 5.1. Introduction

Supersaturation of total dissolved gases (TDG) can be generated during hydropower spills primarily by the entrainment of air in the form of bubbles by the spill water plunging into deep stilling basins. The supersaturated TDG water downstream of hydropower facilities can be harmful to fish. Gas supersaturation may result in a disease called gas bubble disease, which results from the formation of gas bubbles in the blood and tissues of aquatic animals (Weitkamp and Katz 1980). The US Environmental Protection Agency (EPA) established a TDG criterion for allowable water quality standard of 110% to prevent fish mortality (USEPA 1986), but spill operations in hydraulic facilities often exceed this criterion (Weitkamp and Katz 1980). The prediction of TDG generation at plunge pools or stilling basins is an important issue for hydropower utilities and environmental regulators.

During spill events, bubbles can be entrained into deep zones in the stilling basin where pressure is high and the gases within these bubbles are forced into solution. As water depth increases, the gas solubility increases with a higher ambient pressure, and more air can be dissolved from bubbles into water. The mass transfer rate from bubble to ambient water is affected by the bubble size, turbulent intensity, pressure, etc. (Li et al. 2020). TDG generation is therefore determined by the operation conditions of hydropower facilities and the geometry of the stilling basins.

To protect the aquatic habitat and optimize operational conditions, it is necessary to predict TDG under different operational conditions. The relationship among mass transfer coefficient, bubble

---

[*] The content of this chapter is being prepared and will be submitted as a journal manuscript.

size distribution, flow pattern, and effective saturation concentration are the basics to build the TDG prediction model. Roesner and Norton (1971) proposed an early analytical model for predicting TDG generation where TDG downstream of hydraulic facilities is related to upstream TDG, effective saturation concentration, mass transfer coefficient, and bubble residence time in water. Johnson and King (1975) improved mass transfer coefficient and bubble residence time based on field data. Another important improvement to the TDG prediction model was made by Geldert et al. (1998), taking mass transfer across the bubble-water interface and at the free surface into account. However, these models can only be used on some specific spillways and highly dependent on field data since the mass transfer coefficient is calibrated with field data and varies with dam geometry and operational conditions.

With the development of numerical modelling, computational fluid dynamics (CFD) models have been widely applied to predict TDG generation to reduce the reliance on experimental or field measurement of hydrodynamics data (Orlins and Gulliver 2000; Weber et al. 2004). In recent years, CFD models have been improved by including bubble number density and transport to predict bubble and TDG distribution in the tailrace (Schierholz et al. 2006; Urban et al. 2008; Politano et al. 2009; Wang et al. 2019). These models provide a good basis for TDG generation and transportation simulation, which can be applied in optimizing operational strategies to minimize TDG (Politano et al. 2012) and designing spillway deflectors (Politano et al. 2014). All of these CFD models assumed a known entrained air volume fraction and bubble size to calibrate the measured TDG level.

Most of the studies on the process and mechanism of TDG generation are from surface jet (Gulliver et al. 1997; Wilhelms et al. 2005; Li et al. 2009; Politano et al. 2007) and plunging jet (Ma et al. 2016; Lu et al. 2019; Kamal et al. 2020). This study investigated TDG generation at submerged

low-level outlets (LLO) at Hugh Keenleyside Dam (HLK), British Columbia, Canada. It has been observed that the LLO could generate higher than 130% TDG. The stilling basin bottom elevation at the north LLO is about 8 m deeper than that in the south LLO. Typically, gas transfer is increased by the hydrostatic pressure of the water column in the stilling basin. However, the dam frequently generates higher TDG in the south LLO than that generated in the north LLO (Kamal et al. 2018), which provides a unique opportunity to study TDG generation downstream of low-level outlets with various geometries. Previous studies lack the understanding of such phenomenon, and were not able to predict TDG generation of the low-level outlets.

The objective of this study is to understand the mechanisms of TDG generation at LLOs as traditionally these facilities are believed to be immune from air entrainment and supersaturated TDG generation. An analytical model was developed to predict TDG generation at LLOs to investigate the influencing factors such as the turbulence level and bubble size distribution in the stilling basin. This study also investigates the mechanisms and predicts the amount of air entrainment at LLOs. The models were then validated using the predicted air demand and TDG levels and comparing them against field data for the LLOs in Hugh Keenleyside Dam under various operational conditions.

## 5.2. Methodology

### 5.2.1. Field Measurement

The Hugh Keenleyside Dam (HLK) is a 52 m high storage facility constructed under the Columbia River Treaty located on the Columbia River approximately 60 km upstream from the BC-Washington border (Bruce and Plate 2013). There are two styles of outlet gates at HLK: four radial spill gates in between two sets of four low-level outlet gates (LLOs) as shown in Figure 5-1(a).

Note that all LLOs are fully submerged as shown in Figure 5-1(b). All the gates have a total discharge capacity of 10,500 m$^3$/s. These flows are passed in accordance with the Columbia River Treaty between Canada and the United States. These two sets of LLOs are identified by their location relative to the spillways: the north LLOs (N-LLOs) and the south LLOs (S-LLOs). Most of the characteristics of LLOs between south and north are the same, except the two main differences shown in Figure 5-1(b) and Table 5-1: (1) the bottom elevation of the south stilling basin is 399.9 m, which is about 8.2 m higher than that of the north stilling basin at 391.7 m; (2) the end sills in the south basins have an elevation of 413 m, which is 11.9 meters higher than the north sills. A variety of combinations of LLOs can be operated at any time.

The fieldwork was conducted during July 26-30, 2016, July 14-16, and November 5-6, 2020. In 2016, the fieldwork was carried out for different combinations of operations of the south and north LLOs to investigate the potential of TDG generation for different LLOs. A total of 4 scenarios with the operation of LLOs were observed during the period of the fieldwork. Out of the 4 scenarios, 2 scenarios were conducted with 3 north or south LLOs, and the other 2 scenarios were conducted with the combination of south and north LLOs. In July 2020, the fieldwork was carried out for different gate openings for a single north LLO or a south LLO. The radial gate spillway was also operated during the fieldwork to keep the same total flow rate. A single south or north LLO was operated with various gate openings and flow rates in November 2020. During the monitoring period of these field measurements, the tailrace elevation was between 420.0 m and 421.5 m, and the height of water intake ($H_f$) was between 21.8 and 28.0 m. Details about the operational conditions are shown in Table 5-2.

During the survey, stationary continuous monitoring using fixed platforms was adopted to collect the measurements of TDG. Total gas pressure (TGP), barometric pressure (BP), and water

temperature were measured by Lumi4 DO-TGP and PT4 Smart TGP probes (manufactured by Pentair Aquatic Eco-Systems, Apopka, Florida). These probes measure the gas pressure using membrane diffusion technique and are capable of recording TGP and BP with an accuracy of $\pm 2$ mmHg. The accuracy of temperature measurement was 0.2 ºC. Prior to the fieldwork the probes were calibrated in the air locally. During the field observation, one monitoring station was installed about 250 meters downstream of LLO at the end of a rock berm and held probes submerged about 1 meter below the surface (Figures 5-2a, 5-2b). In 2016, TDG was also measured by taking spot measurements from a boat across the river at 550 m downstream of the dam (Figure 5-2a), which is the closest transect with boat access. The collection of spot measurements was conducted by maintaining at a single position in the river by anchoring. The probe was lowered approximately 1 – 1.5 m into the water for a period of about 10 – 20 minutes which allowed to stabilize the TDG reading. Approximately five measurements were taken at one transect. A handheld GPS device was used to record the location of the measurement.

Upstream reservoir TDG levels were collected at approximately 1.6 km upstream of the dam in 2016. Three measurements were taken from the forebay and ranged from 108% to 111% supersaturation. These measurements were taken 1–1.5 m below the surface, one other measurement was taken at a depth of 15 m and resulted in 107% TDG. These differences in measurements within the forebay were small and an average constant value of 109% was adopted for later analysis. In July and November 2020, TDG was monitored continuously in the forebay (about 150 m upstream of the dam) on the floating platforms as shown in Figure 5-2(a).

The air was entrained into the LLOs flows through the gate hoist room which was connected with the atmosphere through windows as shown in Figure 5-1. Spot measurements of air velocity were taken on the top of the gate well in the low-level machinery room during the fieldwork from July

14 – 16, 2020. A hotwire velocity meter (TSI Alnor 9535-A) was used to measure the air velocity on the top of the gate well (Figure 5-2c). The size of the gate well is 5.9 m × 2.7 m, and a platform equipped with ropes for lifting the gate was placed on the edge of the top of the gate well. Spot measurements of air velocity were taken at four different points. The air velocity was recorded for one minute with a one-second interval at each measurement point.

The spill flow from the low-level outlets will mix with the flow from the generating station (Figure 5-2a) approximately 300 m downstream of the dam, and it has been observed that TDG in the spill flow is not diluted with the generation flow until far downstream of the confluence (Kamal et al. 2019). To obtain a detailed description of gas transfer in the dam, additional TDG data were collected for spill events in 1992-1994. All the operational conditions are shown in Table 5-2.

### 5.2.2. *Analytical Modeling of TDG Generation*

Downstream of the south LLOs, water depth in the stilling basin is about 11 m deeper than that downstream of the end sill, and thus the flow field and turbulence level are significantly different in these two regions. In this case, the flow is divided into two different regions: the stilling basin (Region I) and tailwater downstream of the end sill (Region II) as illustrated in Figure 5-1 (b). In a stilling basin, there are two types of interfaces for gas transfer: the air-bubble interface, and air-water free surface. The entrained air bubbles in a stilling basin are forced to dissolved into water due to the acted hydrostatic pressure, and the gas transfer occurs across the air-water interface of these bubbles. Gas transfer can also occur across the air-water interface of the free water surface. In each region, the change in concentration of TDG ($C$) due to the flux across bubble-water interface and river free surface can be written as:

$$dC = K_b a_b (C_{se} - C) dt_b + K_s a_s (C_s - C) dt_b \quad (5-1)$$

where $K_b$ and $K_s$ are the mass transfer coefficient at the bubble-water interface and free surface, respectively, $a_b$ and $a_s$ are the specific area of bubble-water interface and free surface, respectively, $t_b$ is the time over which bubble mass-transfer takes place (seconds), $C_{se}$ is the effective saturation concentration (mg/L) within the region, and $C_s$ is the air saturation concentration (mg/L) at atmospheric pressure. The effective saturation concentration $C_{se}$ can be estimated as (Hibbs and Gulliver, 1997):

$$C_{se} = C_s \left( 1 + \frac{H_{eff} \gamma}{P_{atm}} \right) \quad (5-2)$$

where $C_s$ is the air saturation concentration at atmospheric pressure (mg/L), which is a function of pressure and temperature, $P_{atm}$ is the local atmospheric pressure (Pa), and $H_{eff}$ is an effective depth that bubbles experience. An equation for the bubble penetration depth was derived by Hibbs and Gulliver (1997):

$$\frac{1}{\left( \frac{d_{eff}}{H} \right)} = \frac{1}{\alpha_1 \left( \frac{H_p}{H} \right)} + \frac{1}{\left( \frac{H_{eff}}{H} \right)_{max}} \quad (5-3)$$

where $(H_{eff}/H)_{max} = 2/3$, $H_p$ is the maximum bubble penetration depth given by Eq. 5-4, and $\alpha_1$ is the fraction of the distance from the water surface to the centroid of the bubble swarm and is approximately 0.32 based on an empirical fit of field observations (Hibbs and Gulliver, 1997).

$$\frac{H_p}{d_j} = \left( \frac{v_j}{v_b} + \sqrt{ \left( \frac{v_j}{v_b} \right)^2 - \frac{41.73 \tan \alpha_2}{\sin^2 \theta} } \right)^2 \Bigg/ \left( \frac{6.46 \tan \alpha_2}{\sin^{1.5} \theta} \right)^2 \quad (5-4)$$

Here, $d_j$ and $v_j$ are the jet thickness and velocity at the basin plunge point respectively, $v_b$ is the bubble rise velocity ($\sim$0.25 m/s), and $\alpha_2$ is the angle of outer jet spread, which is about 14° (Ervine

et al. 1997). Solving Eq. 5-3, allows the penetration depth of bubbles to be estimated under both low and high discharge conditions, which is always significantly greater than the stilling basin depth at the HLK dam. From Eq. 5-4, the larger penetration depth, the closer the effective depth approaches 2/3 of the water depth. Thus, in this study, the effective depth is assumed to be 2/3 of the tailwater depth ($H_{eff} = \frac{2}{3}H$). In turbulent flow, the mass transfer coefficient at the interface of bubble-water can be calculated using the equation proposed by Lamont and Scott (1970):

$$K_b = 0.4(v/D_m)^{-1/2}(v\varepsilon)^{1/4} \quad (5-5)$$

where $v$ is the kinetic viscosity of the air-water mixture, $D_m$ is the molecular diffusivity, and $\varepsilon$ is the turbulent kinetic energy dissipation rate. Although Eq. (5-5) may might not able to accurately predict the mas transfer coefficient in different stilling basins with various geometry, it can reflect the influence of turbulence level and has been commonly used in predicting TDG generation downstream of spillways (Urban et al. 2008; Politano et al. 2009; Wang et al. 2019). The key part of the model development is to calculate the turbulence. The turbulent dissipation rate can be determined by following Launder and Spalding (1974): $\varepsilon = C_\mu{}^{3/4}k^{3/2}/l$, where $C_\mu$ is an empirical constant specified in the turbulence model; $k$ is the turbulence kinetic energy (TKE); and $l$ is the turbulence length scale. Nezu and Nakagawa (1993) proposed that the macroscale eddy can be determined by the curve for the wall region and free surface region. The average macroscale turbulence length for the entire depth can be calculated by integrating over depth in both regions (Urban et al. 2008): $l = 0.62H$, where $H$ is the water depth in Region 1 ($H_I$) or Region 2 ($H_{II}$). The turbulence length increases as water depth grows. The turbulence kinetic energy can be represented by velocity and turbulence intensity: $k = 1.5(UI)^2$, where $U$ is the water velocity; and $I$ is the turbulence intensity. Experiments have been conducted on the open channel flow to investigate

the estimation of turbulence intensity (Nezu and Nakagawa 1993):

$$I = \frac{2.3e^{-y/H}}{\kappa^{-1}\ln\left(\frac{y}{H}\right) + w\left(\frac{y}{H}\right) + \left(-\kappa^{-1}\ln\left(\frac{k_s}{H}\right) + A_r\right)} \quad (5-6)$$

where $\kappa$ is von Karman constant; $y$ is vertical position; $k_s$ is the sand roughness height; and $A_r$ is constant of integration, here $A_r = 8.5$. The turbulence intensity was found relatively independent with Reynolds number if $y/h > 0.1$. In this study, the turbulence intensity will be obtained from the average value of turbulence intensity at $y/h = 0.2$ and $0.8$. Note that Eq. (5-6) was obtained from the measurements in open channel flow and would have some difference with that in the stilling basin. In this case, the calculated turbulence kinetic energy will be compared with the that obtained from CFD model. The mass transfer coefficient at the free surface $K_s$ represents the air flux across the free surface to the atmosphere, which was measured to be 0.001 m/s for tanks and bubble columns in a lab scale (DeMoyer et al. 2003). In this study, the mass transfer coefficient at the free surface is obtained from the method used in a field scale proposed by Geldert et al. (1998) and Ma et al. (2016) :

$$K_s = 0.00243 U_s{}^{-5/3} k^{4/3} \quad (5-7)$$

where $U_s$ is the water surface velocity.

Bubble-water interfacial area is determined by the amount of entrained air void ratio and bubble size. The bubble size changes with different flow patterns, and greatly affects bubble-water interfacial area and TDG generation. Hinze (1955) and Gulliver et al. (1990) found that the bubble size that exists in the flow is relevant with surface tension and shear forces, and can be represented as:

$$D_{in} = \left(\frac{\sigma}{\rho}\right)^{3/5} (\frac{k^{3/2}}{l})^{-2/5} \quad (5-8)$$

where $D_{in}$ is the bubble size in the closed conduit; $\sigma$ is the surface tension; and $\rho$ is the water density. $k$ and $l$ are the turbulence kinetic energy and turbulence length in the closed conduit. Note that the bubble size estimation was based on the experimental study in rotating concentric cylinders rather than the field measurements. Further bubble size measurements are expected in the field condition to validate the estimation of bubble sizes. The bubble number per unit volume $N_0$ (bubble number density) at the inlet can be calculated by the entrained air void ratio $\beta$ divided by the single bubble volume, which is:

$$N_0 = \frac{6\beta}{\pi D_{in}^3} \quad (5-9)$$

Bubble size changes with different turbulence conditions, therefore the bubble number also varies due to bubble breakup and coalescence. However, bubble breakup is neglected in previous studies (Politano et al. 2017; Wang et al. 2019), which would be acceptable in a relatively mild tailrace. In this study, the outlet flow in the south LLO was observed to be extremely turbulent due to shallower water depth and high water flow rate, higher TDG was also measured in the south LLO. Therefore, the bubble breakup should not be neglected. Chen et al. (2005) proposed that the bubble breakup rate in bubble column flow is determined by turbulent dissipation rate, air-bubble size, eddy size, air volume fraction, bubble number density, etc. Following Chen et al. (2005), the bubble breakup rate is influenced by the bubble size and turbulence level:

$$S_N = \eta N_0 (\frac{\varepsilon}{D_{in}^2})^{1/3} \quad (5-10)$$

where $S_N$ is the bubble breakup rate (s$^{-1}$), $\eta$ is a dimensionless constant. Similar to the estimation of bubble sizes, the bubble breakup calculation proposed by Chen et al. (2005) was obtained from the study in a lab scale, but it can still reflect the effects of turbulence level. Bubble coalescence also contributes the bubble size distribution in the stilling basin, which needs to be investigated in the future study. The new bubble number density is then written as:

$$N = N_0 + S_N t_b \quad (5-11)$$

The mean bubble diameter then becomes $D = \sqrt[3]{6\beta/(\pi N)}$. Therefore, the interfacial area between air bubbles and water is:

$$a_b = N\pi D^2 \quad (5-12)$$

Bubble residence time in the stilling basin is determined by bubble rise velocity, as well as flow velocity. The estimation of bubble residence time is difficult because bubbles may stay in the stilling basin for a long time if trapped in a return roller. Even the bubbles are transported downstream, they are unlikely to move in a simple horizontal or vertical trajectory. In this study, the entrained air bubbles are assumed to move linearly in the upward and forward directions. The bubble residence time with the effects of buoyancy can be: $t_r = H/v_r$, where $H$ is the water depth in the stilling basin ($H_I$) or tailrace ($H_{II}$), $v_r$ is bubble rise velocity, which is determined by bubble size and drag coefficient (Gulliver et al. 1990; McGinnis and Little 2002; Li et al. 2020). The bubble residence time also depends on the geometry of stilling basin and flow velocity: $t_s = L/U$, where $L$ is the length of stilling basin or the tailwater. The bubble residence time in the stilling basin is then obtained from the smaller one from these two different residence times.

### 5.2.3. Numerical Modeling

ANSYS CFX 16.2 was employed for the numerical simulation to obtain turbulence and flow field downstream of the LLOs. In the computational domain, TDG is calculated depends on bubble size distribution. The presence of bubbles in the stilling basin would affect the properties of the flow field and liquid properties, such as the density, viscosity, and velocity of bubble-water mixture flow. The buoyancy and slip velocity of air bubbles also generate the force on the liquid phase. Simulating individual bubbles in a prototypical scale model is beyond the most powerful computers available so far. To overcome this issue, an Algebraic Slip Model (Manninen et al. 1996) is applied to calculate air-bubble volume fraction and bubble velocity. This method is a simplified true multiphase model that assumes the dispersed phase is fairly diluted.

The two-fluid model is applied which calculates the continuity and momentum equations for the mixture phase by adding the continuity and momentum equations for gas and liquid phases (Drew and Passman 1999):

$$\frac{\partial \rho_m}{\partial t} + \nabla \cdot \left( \rho_m \vec{U}_m \right) = 0 \quad (5-13)$$

$$\frac{\partial \left( \rho_m \vec{U}_m \right)}{\partial t} + \nabla \cdot \left( \rho_m \vec{U}_m \vec{U}_m \right) = -\nabla P + \nabla \cdot (\tau_m + \tau_D) + \rho_m \vec{g} \quad (5-14)$$

where $\rho_m \vec{U}_m = \sum_{k=g,l} \beta_k \rho_k \vec{U}_k$, with $\beta_k$, $\rho_k$, $\vec{u}_k$ the volume fraction, density and velocity for phase $k$. Subscripts $g$, $l$, and $m$ indicate gas, liquid and mixture phase, respectively. Here, bubble density $\rho_g$ calculated with the ideal gas law: $\rho_g = \frac{MP}{RT}$, where $M$ is the average molar mass of air, and $T$ is the temperature. $\tau_m = \sum_{k=g,l} \beta_k \tau_k$ is the molecular shear stress, and $\tau_D = -\sum_{k=g,l} \beta_k \rho_k (\vec{U}_k - \vec{U}_m) \vec{U}_k$. Here $\vec{u}_k - \vec{u}_m$ defined as the drift velocity. $P$ is the pressure, and $\vec{g}$ is the gravity acceleration.

The air-bubbles are dissolved into water during the process of TDG generation, and therefore some mass of air bubbles is transferred to water body. Therefore, there is a source term for gas phase continuity equation to present the mass transfer between air bubbles and water:

$$\frac{\partial \beta \rho_g}{\partial t} + \nabla \cdot \left( \beta \rho_g \vec{U}_g \right) = -S \quad (5-15)$$

where $\vec{u}_g$ is the bubble velocity vector, $S$ represents the mass transfer source term.

The momentum equation for the gas phase can be simplified since the inertia and viscous shear stress are relatively much smaller compared to body forces and pressure (Hibiki and Ishii 2003; Manninen et al. 1996):

$$0 = -\beta \nabla P + \beta \rho_g g + M_g \quad (5-16)$$

where $M_g$ is the interfacial momentum transfer between air bubbles and water. In this study, the interphase momentum transfer is only depended on drag. Additionally, air bubbles in the stilling basin are assumed to be spherical. The momentum transfer vector between air-bubbles and water is then write as:

$$M_g = -\frac{3}{4} \frac{\beta \rho_g}{D} C^D |\vec{U}_r| \vec{U}_r \quad (5-17)$$

where $\vec{U}_r$ is the air-bubble slip velocity defined as the bubble velocity relative to the water velocity. The drag coefficient $C^D$ is determined by the bubble Reynolds number $Re_b$, which is written as (Ishii and Zuber 1979):

$$C^D = \begin{cases} \dfrac{24(1 + 0.15Re_b^{0.687})}{R_b} \quad \dots \dots \ D \geq 2 \times 10^{-4} \ \text{m} \\[4mm] \dfrac{24}{Re_b} \ \dots \dots \ D < 2 \times 10^{-4} \ \text{m} \end{cases} \qquad (5-18)$$

The interfacial momentum transfer is derivative from combining the gas momentum equation and bulk momentum equation to eliminate the pressure gradient term (Ishii 1977). The air bubble is assumed to reach its terminal velocity instantaneously, which means that the transient term of the drift velocity is neglected. The viscous stress and apparent diffusion stresses are also neglected. Thus the closed relationship for the slip velocity can be presented as:

$$|\vec{U}_r|\vec{U}_r = -\frac{4}{3}\frac{D}{\rho_l}(\rho_g - \rho_m)\left[\frac{\partial \vec{U}_m}{\partial t} + (\vec{U}\nabla)\vec{U}_m - \vec{g}\right] \qquad (5-19)$$

The TDG concentration is calculated from the transport equation as shown below:

$$\frac{\partial C}{\partial t} + \nabla \cdot (\vec{U}_m C) = \nabla \cdot \left[\left(v + \frac{v_t}{S_c}\right)\nabla C\right] + S \qquad (5-20)$$

where $v$ is the molecular kinetic viscosity of the water-air mixture, $v_t$ is the turbulent eddy viscosity; $S_c$ is the turbulent Schmidt number. The mass transfer rate between air-bubbles and water can be written as (Politano et al. 2009):

$$S = \pi D^2 N K_L (C_{se} - C) \qquad (5-21)$$

Bubble number density source term is added in the transport equation to express the bubble breakup and it will have some influence on TDG generation. Bubbles coalescence is neglected in this simulation, which will be investigated in future study. The new transport equation for bubble number density is then:

$$\frac{\partial N}{\partial t} + \nabla \cdot \left( \vec{U}_g N \right) = S_N \qquad (5-22)$$

where $S_N$ is the source term for bubble breakup.

The submerged outlet in the LLO discharge the spill flow into the bottom of stilling basin, and the free water surface is relatively flat on the stilling basin. In this study, a rigid lid approach enforcing zero normal fluctuation is implemented in the water free surface. Reynolds-averaged Navier-Stokes models (RANS) are commonly used in hydraulic simulation, the standard $k$-$\varepsilon$ model is chosen for turbulent closure in the numerical simulation.

In this study, only part of the LLOs is simulated to minimize the computational resources. It has been found that the dissipation rate of TDG and mixing rate from lateral flow near tailrace is very small and will not change the maximum TDG generated from the LLOs (Kamal et al. 2019; Wang et al. 2019). The computational domain is selected 700 meters downstream of the HLK dam, including both south and north LLOs. Engineering drawings of LLOs, baffles, end sills and bathymetry data are collected from BC Hydro and applied in this study. Structured mesh is generated in the computational domain. After mesh sensitivity analysis, the computational domain of south LLO containing about 1.1 million nodes, and 1.3million nodes is generated for north LLOs.

Two sets of scenarios operated in November 2020 were simulated in both south and north LLOs. Boundary conditions applied in the numerical model are shown in Figure 5-3. Flow discharges were set to be 150 and 350 m³/s in the inlet of the single gate in the south or north LLO, in which the gate openings were 2.0 and 4.6 m, respectively. TDG concentration in the inlet was set to the same level as in the forebay. The implicit assumption is that the mass of air bubbles is replaced by

an equal mass of water. Additionally, the mass transfer coefficient ($K_s$) across the free surface is set as 0.0001 m/s at the top of the computational domain, which was measured by DeMoyer et al. (2003) for bubble columns and also applied in other TDG prediction models (Politano et al. 2009). In most cases, the contribution of the free surface mass transfer is small, which is about between 0.00007 and 0.0006 time of the mass transfer in the bubble-water interface (Kamal et al. 2020). A no-slip condition and zero flux for all other variables are used at the river bed and walls. Following Meselhe and Odgaard (1998) and Wang et al. (2019), the effect of roughness is neglected in this numerical model. Symmetry conditions with zero stress and zero flux for all variables are applied on the lateral sides of the computational domain. Hydrostatic pressure is used at the outlet based on the measured tailwater depth, other variables are set with zero gradient. Pressure in the computational domain was set to be the hydrostatic pressure which is the same as the corresponding tailrace water depth. Entrained air volume fraction and bubble size were obtained from the analytical calculation as discussed in the previous section.

## 5.3. Results and Discussions

Under a similar operational condition, the south LLO always generated higher TDG than that in the north. For instance, the spot measurements in 2016 showed that the south LLO can generate about 123% TDG, whereas at the same discharge the north LLO can only generate about 112% TDG with a much deeper stilling basin. Marked differences in concentrations were observed between the spill and generation flows, with spill releases containing about 123% TDG near the south bank (Figure 5-4a). TDGs near the north bank (corresponding to generation flow) were in the range 108%–110%. Figure 5-4(b) illustrates the continuous TDG level downstream of LLOs with the combined operation of the south/north LLO and the radial gate spillway. Note that the

110

operated spill gate was close to the south LLO, continuous station could only record the TDG level of mixed water from the south LLO and spill gate. The TDG generated from the spill gate could be estimated using the empirical equation proposed by Bruce and Plate (2013), and then the TDG generated from LLO can be estimated, which also showed that the south LLO generated higher TDG (115 – 120%) than that generated in the north LLO (110 - 113%). In the fieldwork conducted in November 2020, TDG generated in the S-LLO was about 7-11% higher than that generated in the N-LLO, as illustrated in Figure 5-4(c). To have a better understanding of the TDG generation in different LLOs with various tailrace conditions, it is necessary to develop a general TDG generation prediction model for LLOs.

### 5.3.1.  *Flow Field in the Tailrace*

The geometry of stilling basin in HLK is complicated and not a typical forced hydraulic jump-type basin. The different elevations of stilling basin floors and end sills are a result of the dam being built to conform to the bedrock foundation. Thus, the basin geometry between the north and south low-level outlets is significantly different as discussed above. With a shallower and more closed-off stilling basin, the south low-level outlets may produce much more turbulent flow conditions, and thus break up the entrained air bubbles into smaller sizes, increasing the interfacial area available for gas transfer to occur. It is believed that the water level and the turbulence in the stilling basin have a significant influence on the TDG generation.

Applying the rigid lid approach, the suppression of the actual surface deformation may lead an error in the continuity equation, but the influence can be neglected if the surface deviation is less than 10% of the local water depth (Ramos et al. 2019). From the free surface simulation (VOF method), the maximum surface deviation is about 7% compared with the local water depth.

111

Additionally, the rigid lid simulation computes similar turbulence kinetic energy (TKE) compared with the free surface simulation, suggesting the influence of the suppression of the actual surface deformation in rigid lid simulation is small.

Figure 5-5(a) shows the simulated flow field and turbulence kinetic energy (TKE) distribution in both the south and north LLOs with 350 $m^3$/s water discharge. The return roller in the south stilling basin is relatively stronger than the north, which indicates the stronger turbulence and bubble would stay a longer time in the stilling basin. In the north stilling basin, the flow jet is deflected upward by the end sills at the end of the stilling basin and most of the flow is remaining around the water surface. Even though the water depth in the north tailrace is much deeper than the south, most of the water with entrained air bubbles will not flow downward after passing through the north end sills. In this case, high-level TDG is not expected to be generated despite a larger water depth in the north tailrace. Note that the mean TKE in the stilling basin (Region I) simulated by the CFD model has a good agreement with that calculated using the method proposed by Nezu and Nakagawa (1993) as shown in Figure 5-5(b), indicating the turbulence intensity calculated in the analytical model is reasonable. The calculated TKE is also in the range of that in the plunge pool downstream of a plunging jet (about $1 - 8$ $m^2/s^2$) as reported by Xu et al. (2002). Under the same operation condition, both CFD and analytical models showed the TKE in the stilling basin of south LLO is larger than that in the north.

The turbulence dissipation rate in the south LLO is significantly higher than that in the north LLO as shown in Figure 5-6(a-b). In Region I, the generated TDG increased with turbulence dissipation rate, which suggests the turbulence dissipation rate plays an important role in TDG generation. In the tailrace downstream of the end sill (Region II), the water depth in the N-LLO is about 3 times that in the S-LLO, the turbulence dissipation rate of N-LLO was no more than 0.005 $m^2s^{-3}$, which

was significantly less than that in the S-LLO (between 0.01 and 0.5 $m^2s^{-3}$). Due to the energy dissipation, the turbulence dissipation rate in Region II was smaller than that in Region I.

The mass transfer coefficient across bubble-water interface $K_b$ is influenced by the turbulence dissipation rate as shown in Eq. (5-5). In both Regions I and II, $K_b$ of south LLO was larger than that of north LLO (Figure 5-6c-d). Due to the larger turbulence dissipation rate in Region I, $K_b$ in Region II was less than that in Region I for both S-LLO and N-LLO. Although the mass transfer coefficient in Region II was smaller than that in Region I, TDG could still be generated in Region II. The mass transfer coefficient $K_b$ is between $2\times10^{-5}$ and $5\times10^{-4}$ m/s, which is higher than that in a flume with a lab scale ($1 - 2\times10^{-5}$ m/s) reported by Li et al. (2002). Below prototype spillway plunge pools in the Columbia and Snake rivers, the mass transfer coefficient $K_b a_b t_b$ was between 0.03 and 1.04 (Geldert et al. 1998), which was a little larger than that downstream of LLOs in HLK dam (0.006 – 0.11). Thus the mass transfer coefficient used in this study is in an acceptable range compared with previous studies.

### 5.3.2. *Air Demand Prediction*

The air entrainment into the LLOs flows is mainly comes from the gate hoist room which is connected with the atmosphere through windows as shown in Figure 5-1. Although some empirical equations have been developed to predict air entrainment in closed conduits, these equations are not applicable in submerged outlets (Falvey 1980; Hohermuth et al. 2020). Li et al. (2021) developed a model for predicting air demand in a submerged closed conduit and found that the air demand is significantly influenced by the flow regime downstream of the control gate and outlet condition. They proposed prediction models for various outlet conditions and flow regimes downstream of the control gate. During the field measurement, the hydraulic jump was partially

submerged in the low-level outlet of the HLK dam. Air bubbles are mainly entrained by the breaking of the surface roller instead by the advective diffusion region. Therefore, the relative air demand was significantly smaller than that of an unsubmerged hydraulic jump. In such flow condition, the relative air demand could be estimated using the developed equation proposed by Li et al (2021):

$$\beta = \frac{4}{(\mathsf{F}-1)^2}\left(\beta_K - 0.294\frac{H_o/D - 1}{\mathsf{F}-1}\right) \quad (5-23)$$

where $\mathsf{F}$ is the Froude number at vena contracta of the operating gate, $H_o$ is the water depth above the invert of the closed conduit outlet (Figure 5-1), and $\beta_K = 0.0066(\mathsf{F}-1)^{1.4}$ is the air demand in a closed conduit with a free surface outlet proposed by Kalinske and Robertson (1943).

Overall, the predicted $\beta$ has a similar trend as the field measurements conducted in July 2020, and both give relatively low air demands ($\beta < 1\%$) as shown in Figure 5-7(a). The difference between the prediction and the measurement is noticeable at small gate openings. This is likely caused by the measurement uncertainties due to the low air velocity in the field measurements. Additionally, there could be scale effects, but likely not significant. In general, the air demand prediction using Eq. (5-23) can provide a reasonable estimate for the relative air demand. Note that the engineering design and outlet depth ($H_0$) of south and north LLOs are similar, so that very close air demands were observed in the field measurement (Figure 5-7a). In this study, the air demand in south and north LLOs were regarded as identical under the same operational conditions.

### 5.3.3. TDG Prediction

The only adjustable coefficient in the TDG prediction model is $\eta$ in Eq. (5-10), which influences the bubble breakup in the stilling basin. Calibrated with the field data in 1993, $\eta$ is 0.17. After that,

the model was validated with the field data measured in 2016 and 2020, which has a good agreement with the prediction with 3% error, as shown in Figure 5-7(b). From the field measurements, as well as the predictions, the TDG generated in the south low-level outlets was mostly between 110 - 120%, which was larger than that in the north low-level outlets (100 - 112%).

Figure 5-8 illustrates the TDG distribution along the stilling basin in the south and north LLOs with the discharge of 350 $m^3$/s simulated by the CFD model. The percentage of TDG is calculated by the simulated TDG divided by the equilibrium TDG concentration at atmospheric pressure. The mean TDG level in the south stilling basin is about 10% higher than that in the north due to the stronger turbulence as discussed above. When the flow passes over the end sills of the south LLOs, TDG levels around the tailrace bottom are increasing with streamwise direction, which indicates that the TDG keeps being generated downstream of the stilling basin. However, no more TDG was generated downstream of the end sills of the north LLOs.

Figure 5-9 illustrates the TDG difference between stilling basin and tailrace, which shows that about 1 - 7 % more TDG could be generated in the tailrace under various flow conditions. Under the same unit discharge, more TDG will be generated in Region II of south LLO than that in the north. Therefore, Region II also contributes TDG generation in south LLO. Due to the shallower water depth, the return roller in the south stilling basin is relatively stronger than the north, which explains stronger turbulence and greater TDG in the stilling basin. In this case, even though water depth is large in the north tailrace, high-level TDG is not expected to be generated. Another reason for this could be the smaller bubble generated in the south tailrace which will be analyzed in the next section.

### 5.3.4. Bubble Size Effects

Previous studies of predicting TDG generation always neglect bubble breakup or coalescence. These prediction models fail to predict high level TDG in shallower stilling basins of LLOs. One of the main reasons is that the bubble breakup was neglected in the previous study, which will be included in this study. In this study, two different types of LLOs are investigated with varying depths and end sills.

Figure 5-10 (a) shows smaller bubbles have more mass transfer and generates higher TDG in the stilling basin of south and north LLOs. Due to the stronger turbulence in the stilling basin, more bubbles in the S-LLO were potentially broken up. Thus, the south LLO generated smaller size bubbles (1.1-2.2 mm) with a higher TDG level compared with that of north LLO (1.6-4.3 mm). With the same upstream and downstream water elevation and temperature (operational condition in November 2020), the predicted bubbles in Regions I and II of the south LLO were all smaller than that in the north LLO with a similar unit discharge as shown in Figure 5-10 (b). Smaller bubble sizes indicate that the total bubble-water interface area is larger and more air will be dissolved into the water given the same air demand and mass transfer coefficient. CFD model also shows a smaller bubble size in the south LLO with the same flow discharge and air demand (Figure 5-10c). When the water discharges into the stilling basin (Region I), the bubble diameter in south LLO (0.8-1.8 mm) becomes significantly smaller than that in the north LLO (1.8-3.2 mm), which indicates more bubbles are broke up in the south LLO. In previous studies, Politano et al. (2009) reported that the bubble diameter was between 0.12 mm and 0.8 mm in their CFD model of the tailrace of Wanapum Dam, USA with the operation of spill gates. Wang et al. (2019) simulated a similar bubble diameter range (0.6 – 0.8 mm) downstream of McNary Dam, USA. Ma et al. (2016) proposed a relatively larger mean bubble diameter in the plunge pool of a high dam, which was about 4 mm. Overall, the bubble sizes calculated in this study were in a reasonable range compared

116

with the previous studies.

The calculated bubble sizes are obtained from empirical equations for turbulence level and bubble breakup rate, uncertainties in these equations would cause differences between the actual and predicted bubble sizes. Additionally, measurements of bubble size distribution in the stilling basin or tailrace have been rarely reported in previous studies due to high turbulent flow conditions. To validate the predicted bubble size distribution and to provide referable data to the relevant studies, the bubble size distribution downstream of the low-level outlet will be measured in the future study. For instance, a drone carried with a camera can be controlled to take photos of water free surface downstream of the low-level outlets. A GoPro can also be placed underwater to capture the bubble size distribution. Additionally, microbubbles and nanobubbles are likely to be generated in the tailrace due to the high turbulent condition, and these bubbles can make a great contribution to the mass transfer between bubbles and water (Alheshibri et al. 2016). In the future study, the effects of nanobubbles and microbubbles will be discussed.

Since the air demand and air volume fraction in stilling basins does not have an obvious difference, one of the main reasons for bubble size difference is the air-bubble number density in the stilling basins. Bubbles in the south stilling basin are easy to be broken up due to their high velocity and turbulence. Turbulence difference enhances the bubble breakup and TDG generation. Additionally, the mass transfer coefficient between air bubbles and water is also higher in the south stilling basin due to the high turbulence. Both bubble diameter and mass transfer coefficient make the larger TDG generation. With a smaller size and larger breakup rate, the whole bubble-water interface area in the south tailrace is supposed to be greater than that in the north, and the south tailrace can generate more TDG downstream of the stilling basin.

117

### 5.3.5. *Discussion of Air Dissolution*

To investigate the dissolution of the entrained air, mass transfer efficiency ($E$) is defined:

$$E = \frac{C_d - C_u}{\beta \rho_g} \quad (5-24)$$

where $\rho_g$ is the density of air in the atmospheric pressure, $C_u$ is the TDG concentration in the forebay, and $C_d$ is the concentration of the TDG generated in Region I or Region II. Figure 5-11 illustrated the mass transfer efficiency in both North and South LLOs in the field measurement in November 2020. In the south LLO, mass transfer efficiency increased significantly from 41 – 60% to 56 – 87% after the water in Region I flowed to Region II. However, the mass transfer efficiency was hardly growing in the north LLO, and kept around 25 – 45 % in both Regions I and II. Thus, much more air was dissolved into water and more TDG was generated in Region I of south LLO. Region II in the south LLO also plays an important role in the TDG generation, whereas the tailrace in the north LLO rarely contributes to the increase of TDG.

With the same upstream and downstream flow conditions, the mass transfer efficiency in the south LLO is significantly larger than that in the north LLO, which also explained the high TDG generated in the south LLO. In this case, higher turbulence and mass transfer efficiency, as well as smaller bubble size contributed to the significantly high mass transfer efficiency. Additionally, Ma et al. (2016) and Wang et al. (2019) showed that up to 46.1% and 67.6% of the entrained air were dissolved downstream of the plunging jet or surface jet in their TDG study, respectively, which were in the range of this study. Overall, the mass transfer efficiency of the submerged low-level outlet (HLK Dam) was consistent with that of a surface jet or plunging jet.

## 5.4. Conclusions

Traditionally, low-level outlets are designed to avoid air entrainment and TDG issues. However, field measurements in Hugh Keenleyside Dam in British Columbia, Canada observed more than 130% supersaturated TDG with the operations of low-level outlets. Less than 1% volume fraction air was entrained into the low-level outlets flows through the gate hoist room which connected with the atmosphere. Significant TDG difference between south and north low-level outlets was detected, where the depth in the south stilling basin is about 8.2 m shallower and the top of end sill height is 11.2 m higher than the north. Deeper water typically generate more TDG since it has higher hydrostatic pressure enforcing air dissolved into water with longer residence time. However, field measurements show that there is greater potential for the south low-level outlets to generate TDG.

In this study, a mechanistic model was developed to predict air demand and TDG generation of the low-level outlets. Model results had a good agreement with the air demand and TDG data collected in the field measurement. The inflow and tailrace conditions of the low-level outlets played a crucial role in the air demand. TDG generation downstream of low-level outlets was evaluated by analytical and numerical modeling including turbulence and bubble breakup effects. The bubble breakup is relevant to the turbulent eddy dissipation, which is quite different between south and north low-level outlets. Because of the shallower depth in the south stilling basin and tailrace, there is strong turbulence downstream of south low-level outlets with a similar flow rate as north. Therefore, the bubble breakup rate is much larger in the south part of HLK Dam. In this case, the bubble size of 1.1-2.2 mm is generated in the south low-level outlet, which is smaller than that in the north low-level outlet with 1.6-4.3 mm. Smaller bubble size indicates a larger bubble-water interfacial area under the same amount of air entrainment, and will enhance the TDG generation in south low-level outlets. The high turbulence in south low-level outlets also

contributes to the high mass transfer coefficient, which is about 1.5-4.2 times that in the north low-level outlets. Thus, the stronger turbulence in the south stilling basin can substantially and efficiently enhance gas transfer with larger bubble-water interfacial area and mass transfer coefficient, even though the shallower water has less potential to generate high-level TDG.

Overall, the developed model was able to predict air demand and TDG generation with different stilling basin designs in the low-level outlets, which contributes a good understanding to the TDG generation of different types of hydraulic facilities.

Table 5-1 Geometry of the northern and southern low-level outlet and stilling basin.

| | Inlet Crest (m) | Conduit Slope (˚) | Basin Floor (m) | Top of End Sill (m) | End Sill Height (m) |
|---|---|---|---|---|---|
| NLLO | 411.5 | 19.61 | 391.7 | 401.1 | 9.4 |
| SLLO | 411.5 | 14.76 | 399.9 | 413 | 13.1 |

Table 5-2 Conditions of the HLK low-level outlets field tests of TDG studies

| Date | Operated LLO* | No. of cases | Tailwater elevation (m) | $H_f$ (m) | $Q$ (m³/s) | $C_u$ (%) | $C_d$ (%) |
|---|---|---|---|---|---|---|---|
| November 29, 1992 – June 3, 1994 | N | 22 | 418.1-421.3 | 11.9-22.4 | 188.8-545.6 | 97.0-110.6 | 100.4-110.9 |
| April 4 – May 12, 1994 | S | 8 | 418.0-419.0 | 11.6-16.1 | 141.7-283.2 | 107.0-110.9 | 112.3-122.4 |
| July 26 – 29, 2016 | N or S | 2 | 421.6 | 21.8-22.1 | 186.1-650.0 | 109.0 | 111.8-112.7 |
| July 27 – 28, 2016 | N and S | 2 | 421.6 | 21.8-22.0 | 277.4-311.6 | 109.0 | 115.8-122.1 |
| July 14 – 15, 2020 | S | 5 | 421.5 | 28.0 | 84.1-800.3 | 107.0-107.9 | 111.0-118.5 |
| July 14 – 16, 2020 | N | 3 | 421.5 | 28.0 | 228.2-813.9 | 109.2 | 110.4-113.1 |
| November 5, 2020 | N | 5 | 420.0 | 23.7 | 72.8-339.2 | 98.9-100 | 101.5-103.6 |
| November 6, 2020 | S | 3 | 420.0 | 23.7 | 48.4-351.2 | 98.8-99.5 | 106.6-115.1 |

Note: * N = north LLO; S = south LLO.

(a)



(b)
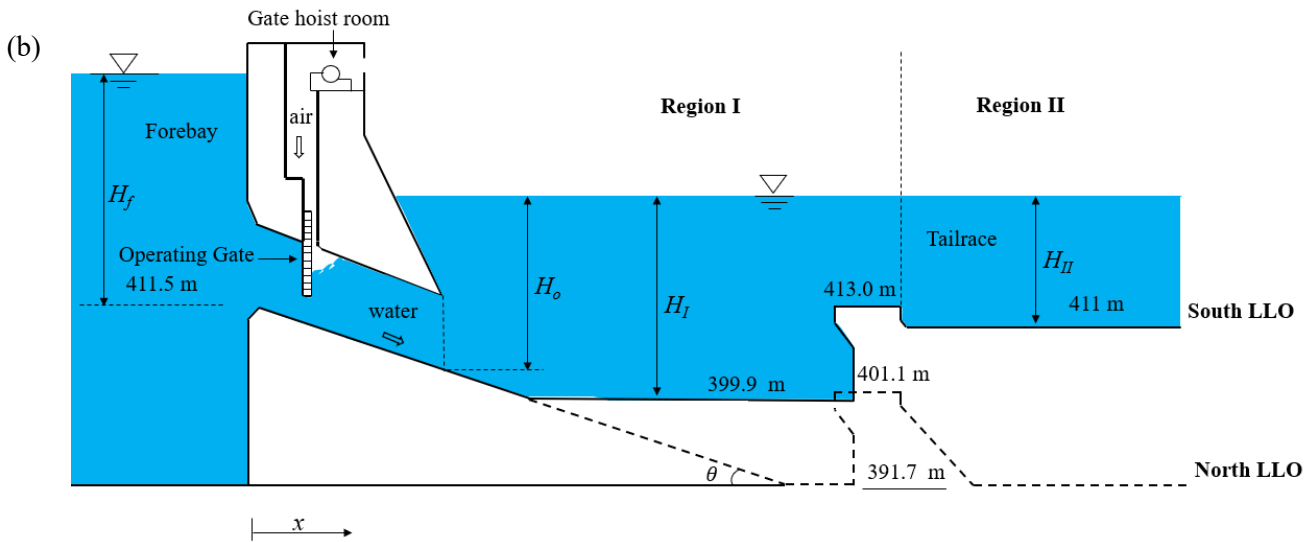


Figure 5-1 (a) Site layout of Hugh L. Keenleyside Dam (Image by James Crossman); and (b) cross-section of north low-level outlet and south low-level outlet.
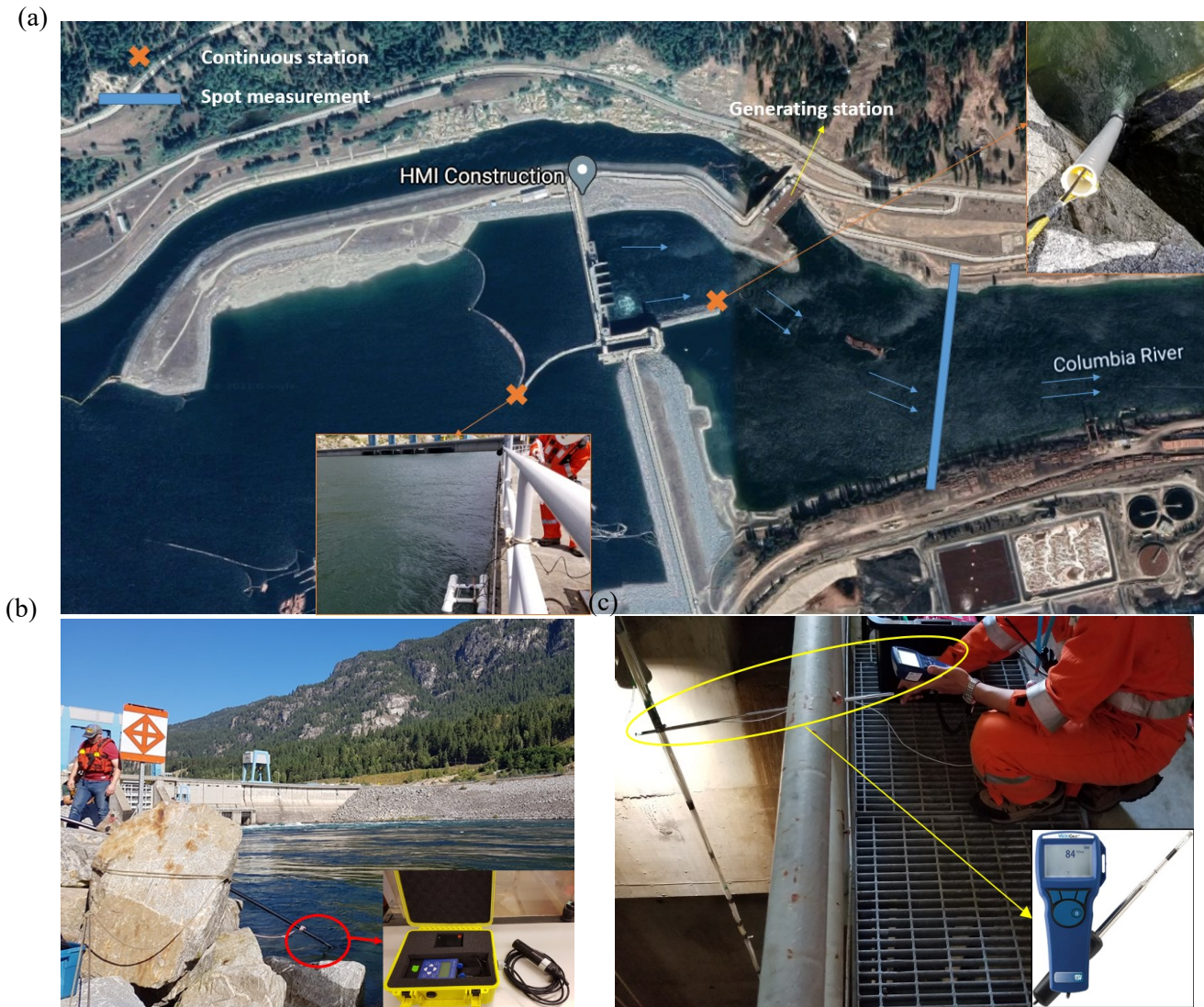
Figure 5-2 (a) Installed fixed monitoring platforms at HLK tailrace and forebay (adapted from map data, Google 2021); (b) installed fixed monitoring platforms at HLK tailrace in 2016; (c) air velocity measurement at the top of the gate well of the LLO.
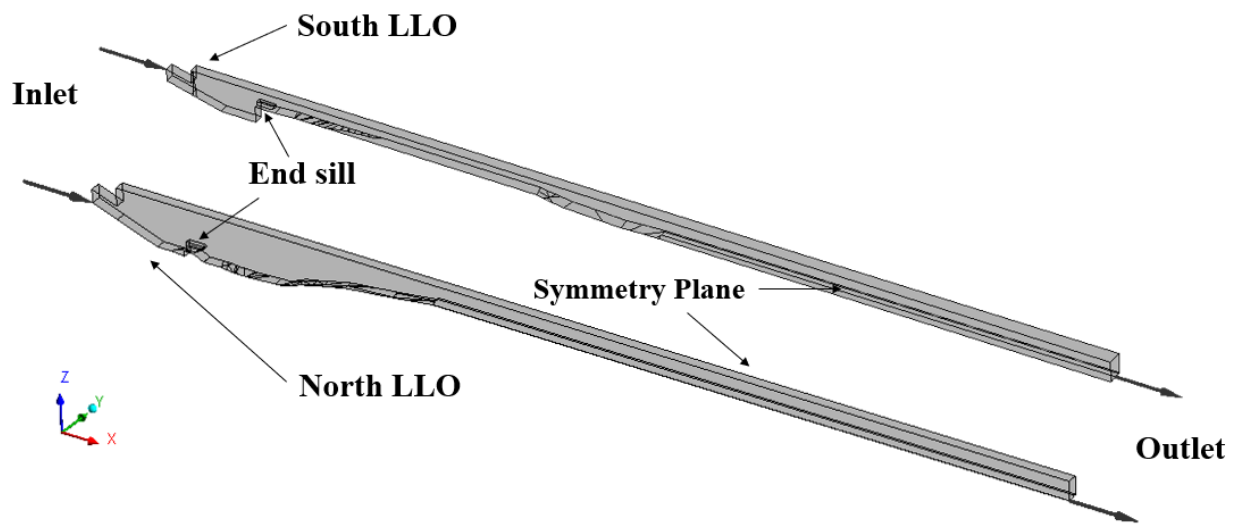
Figure 5-3 Computational domain and boundary conditions in CFD model.
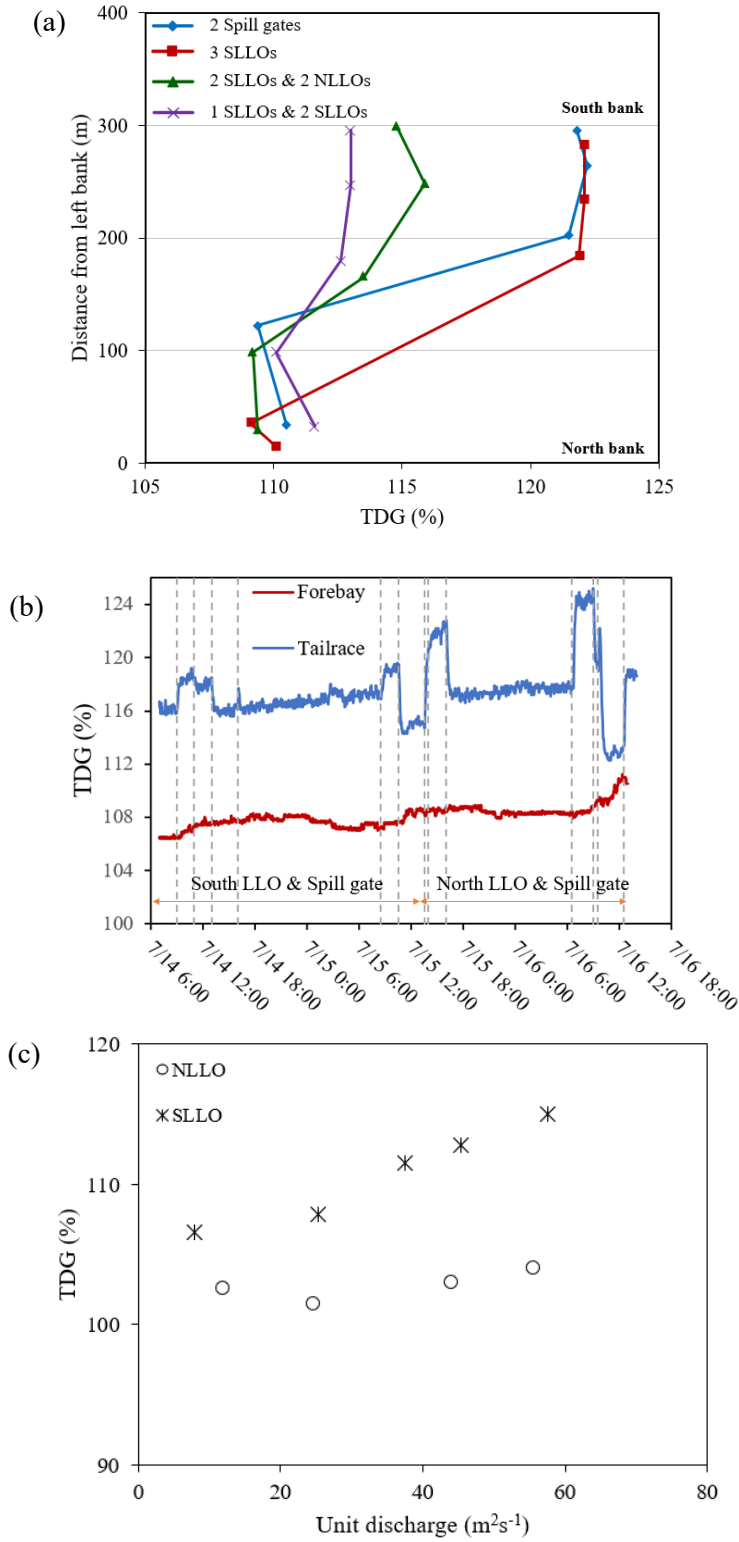
Figure 5-4 TDG measurements downstream of LLOs in (a) July, 2016; (b) July, 2020; and (c) November, 2020.

(a)



(b)
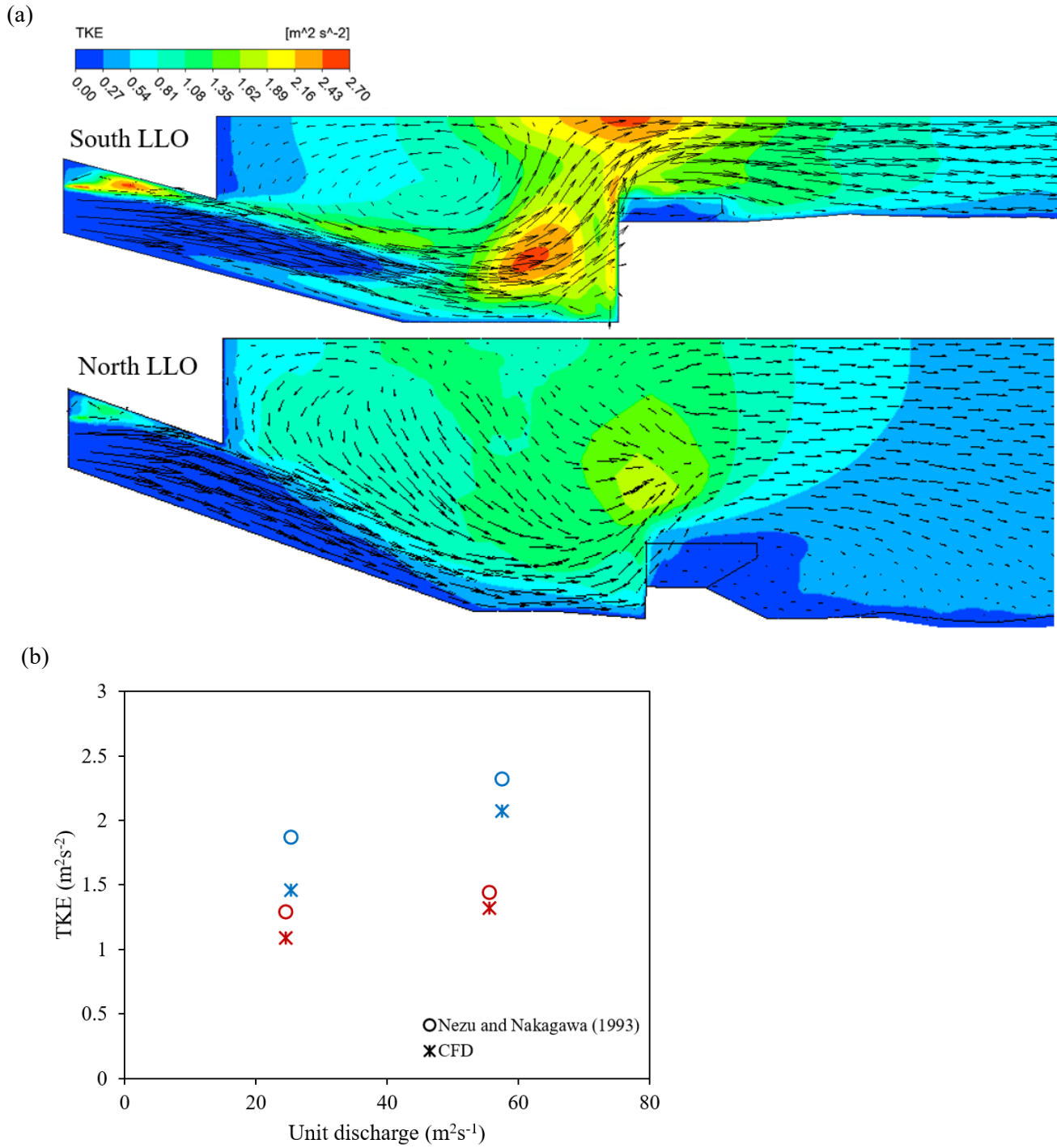


Figure 5-5 (a) Simulated TKE downstream of the south and north LLO with $Q = 350$ m$^3$/s; (b) comparison of the mean turbulence kinetic energy (TKE) between the analytical model and CFD in the stilling basin.
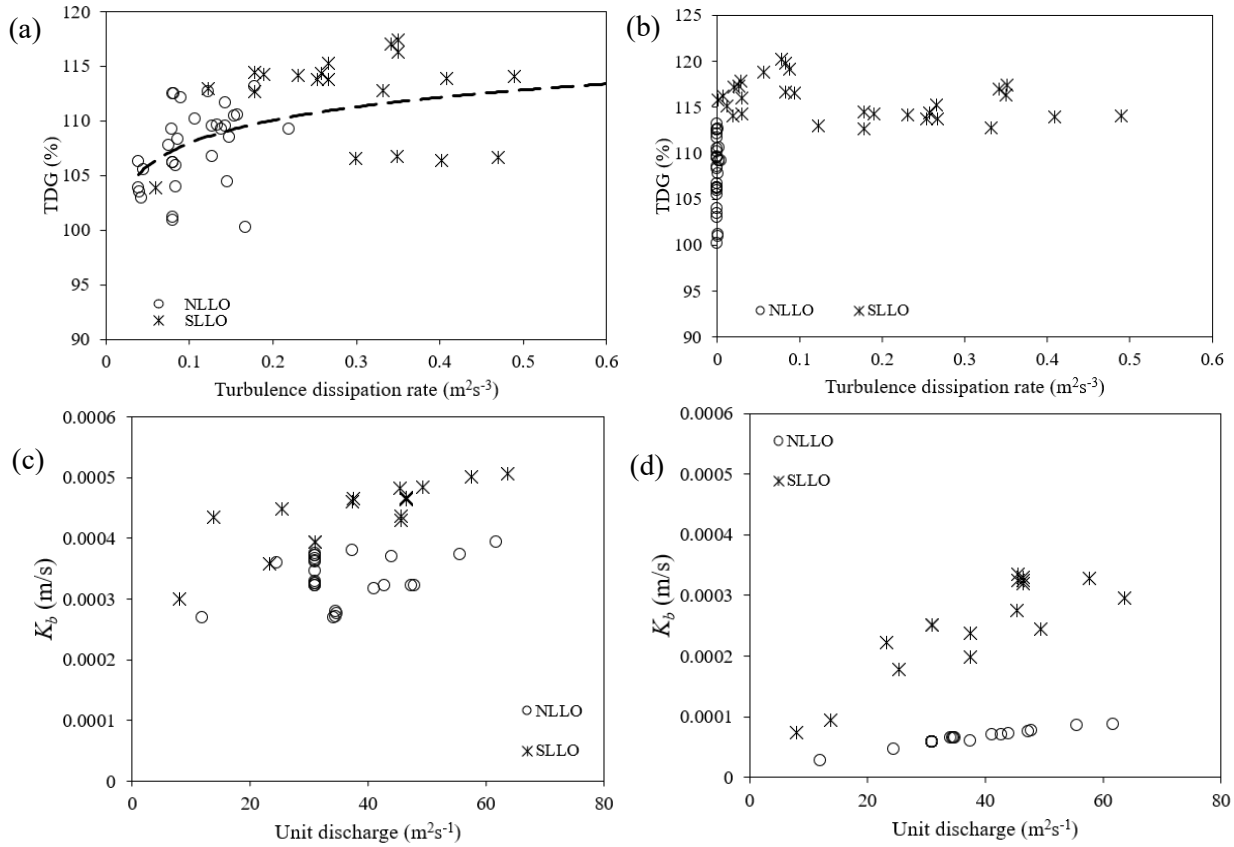
Figure 5-6 Turbulence dissipation rate in (a) Region I; and (b) Region II; mass transfer coefficient

in (c) Region I; and (d) Region II.
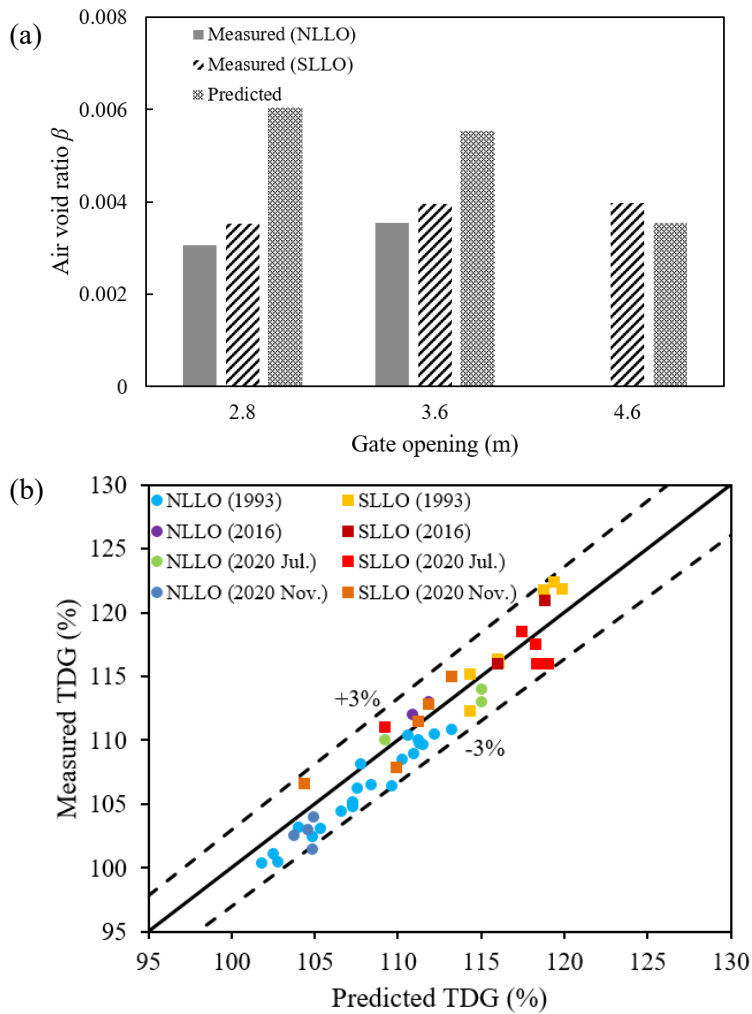
Figure 5-7 Comparison between the measured and predicted (a) air void ratio and (b) TDG at the tailrace of the HLK dam.
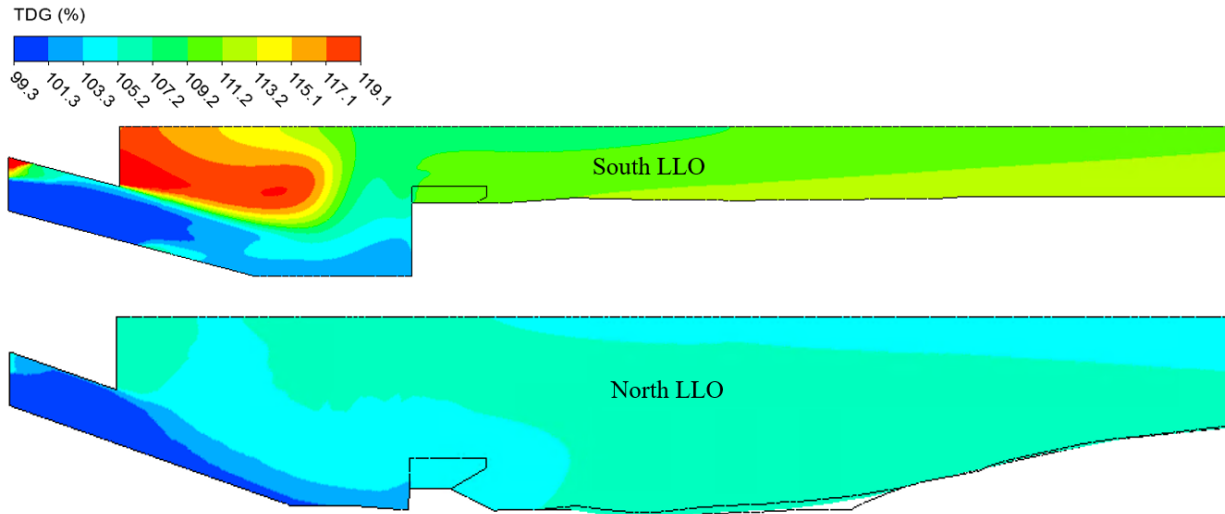
Figure 5-8 TDG distribution downstream of south and north LLOs with water discharge of 350 m$^3$/s.
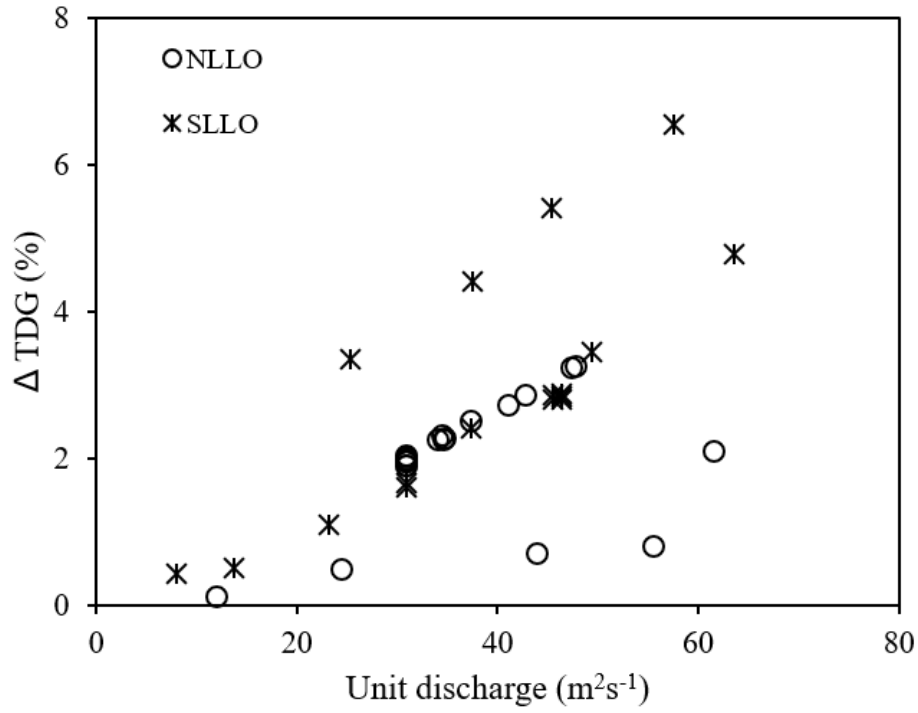
Figure 5-9 Change in TDG level between Region I and II based on model results.
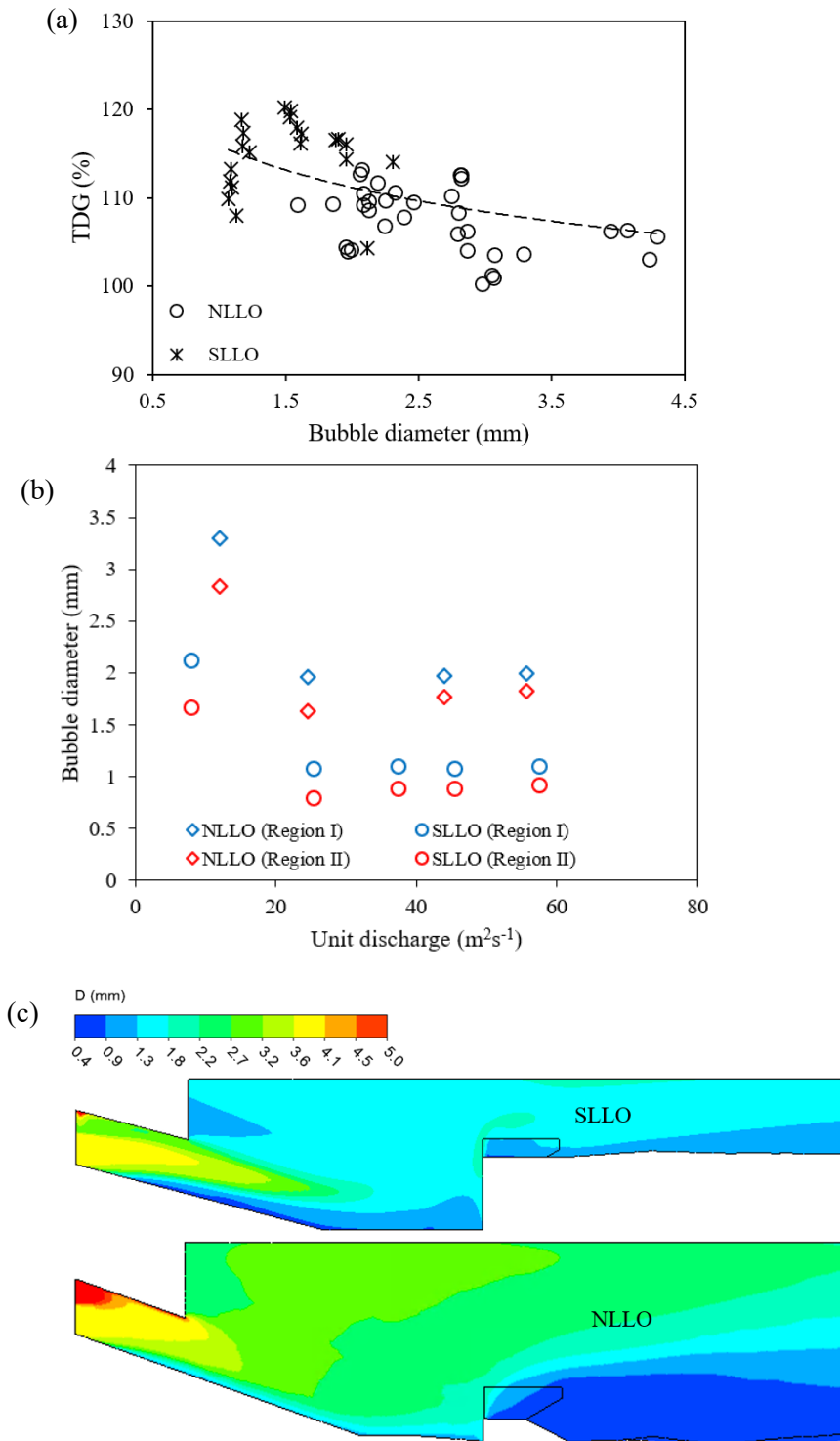
Figure 5-10 Bubble diameter for (a) all operational conditions in stilling basin; (b) operational conditions in November 2020; and (c) bubble diameter distribution with water discharge of 350 m³/s.
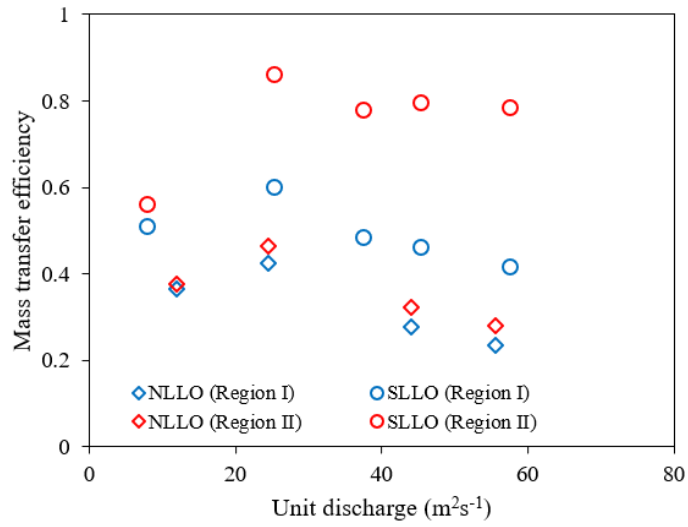
Figure 5-11 Transfer efficiency of LLOs in Region I and II in the field condition of November

2020.

# 6. Conclusions and Recommendations

## 6.1. Conclusions

In this thesis, the process of total dissolved gas (TDG) generation at low-level outlets has been studied: (1) the mass transfer of rising bubbles in water; (2) the air demand of a hydraulic jump in a closed conduit with a submerged outlet; and (3) the generation of supersaturated total dissolved gases of low-level outlets. Some general conclusions are listed below:

1. The mass transfer from a single bubble rising in stagnant water and its size variation could be successfully modeled by an analytical model. The bubble size changed along the rising path in response to both the mass transfer and the local hydrostatic pressure, whereas their relative importance varied under different conditions. The critical depth was proposed to measure the bubble size change as rising. The bubble size kept decreasing when it was beneath the critical depth, where the effect of the mass transfer on the bubble size was more significant than the hydrostatic pressure. Additionally, the mass transfer efficiency decreased with the initial bubble size and background dissolved gas concentration. The developed model was able to predict the mass transfer of different gases and mass transfer of a bubble within bubble swarms, which can be applied in aeration system management, TDG prediction, and other engineering applications.

2. Physical experiments are described to study flow regimes and the air demand of a hydraulic jump in a closed conduit with various submerged outlet depths. Flow characteristics and air demand are influenced by outlet depths. Specifically, free surface supercritical flow without a hydraulic jump can induce a relative air demand (air flow rate to water flow rate) of about 36 - 90% when the Froude number is between 4 and 10, which decreases to about

3 - 14% for a free surface flow with a hydraulic jump. If the hydraulic jump is followed by pressurized pipe flow, the air demand decreases with increasing outlet depth until the return roller is fully developed in the pipe. If the hydraulic jump is partially submerged, the relative air demand is significantly reduced to less than 1%. The air demand was also measured in a prototype low-level outlet of a dam with a partially submerged hydraulic jump, which was consistent with the developed prediction equation based on experimental measurements. Additionally, it was found that the pressure fluctuation at the bottom of the air vent is much larger than that at the top. Limited air supply caused a sub-atmospheric pressure, and the magnitude of the sub-atmospheric pressure significantly increased after sealing the air vent.

3. Supersaturated TDG was observed through field measurements at low-level outlets of a dam, which are typically considered to be free from air entrainment and TDG issues. However, from the field observation, air entrained through the gate well of low-level outlets can potentially induce supersaturated TDG generation. Despite being 8 m deeper, significantly lower TDG levels were measured in the stilling basin of the north LLO's ($\leq$ 110%) compared to the south LLO's (up to 130%). Stronger turbulence in the stilling basin can generate smaller bubbles and increase the mass transfer coefficient across bubbles, which will substantially enhance gas transfer and TDG generation. Deeper tailrace water depth with high pressure typically enforces more air dissolved into water and could promote TDG generation. Thus, higher level TDG generated in shallower water was attributed to its stronger turbulence flow, with more efficient gas transfer and TDG generation compared with the deeper low-level outlets.

## 6.2. Recommendations

This research covers the process of total dissolved gas generation and a wide range of hydraulic engineering topics including the bubble movement and mass transfer in water, air entrainment of a hydraulic jump, and total dissolved gas generation in the stilling basin. However, some aspects still exist for further studies. Some recommendations on further studies are listed below:

1. The movement and mass transfer model of the rising bubbles can be tested in the turbulent flow, which typically occurs in engineering applications. Experimental measurements on the rising bubble sizes and mass transfer in turbulent water could be used to validate the model by using the mass transfer coefficient in turbulent flow condition.

2. Spectral analysis of the air pressure fluctuation needs to be investigated in further study and compared with the previous studies about hydraulic jump fluctuation frequency. The air pressure fluctuation was likely induced by the turbulent oscillations of the hydraulic jump. The measurement frequency of the pressure transducer was not high enough to measure the frequency of air pressure fluctuations in current study.

3. The actual bubble size distribution in the stilling basin or tailrace could be investigated through field measurement or lab experiments with similar flow conditions in the field. Because the bubble size in the field has not been measured. Understanding the actual bubble size distribution would be helpful to improve studies on total dissolved gases generation. Additionally, the contributions of microbubbles and nanobubbles on TDG generation will likely be of interest for future studies.

# Bibliography

Alheshibri, M., Qian, J., Jehannin, M., and Craig, V. S. J. (2016) "A history of nanobubbles." *Langmuir*, 32, 11086−11100.

Alves, S. S., Orvalho, S. P., and Vasconcelos, J. M. T. (2005). "Effect of bubble contamination on rise velocity and mass transfer." *Chemical Engineering Science*, 60(1), 1–9.

Anderson, J., Beer, N., Frever, T., Hayes, J., and Iltis, S. (2000). *Columbia River Salmon Passage Model. Columbia Baisn Reseach*.

Ansys. (2015). "ANSYS CFX 16.0." *ANSYS Inc.*

Arntzen, E. V, Geist, D. R., Murray, K. J., Vavrinec, J., Dawley, E. M., Schwartz, D. E. (2009). "Influence of the Hyporheic Zone on Supersaturated Gas Exposure to Incubating Chum Salmon." *North American Journal of Fisheries Management*, 29, 1714–1727.

Aybers, N. M., and Tapucu, A. (1969). "The motion of gas bubbles rising through stagnant liquid." *Wärme- und Stoffübertragung*, 2(2), 118–128.

Beiningen, K. T., and Ebel, W. J. (1970). "Effect of John Day Dam on Dissolved Nitrogen Concentrations and Salmon in the Columbia River , 1968." *Transactions of the American Fisheries Society*, 99(4), 664–671.

Bentzen, T.R., Østertoft, K.K., Vollertsen, J., Fuglsang, E.D., Nielsen, A.H., 2016. Airflow in gravity sewers - determination of wastewater drag coefficient. Water Environ. Res. 88 (3), 239–256.

Bosman, A., Basson, G. R., and Bosman, D. E. (2016). "Hydraulic model study of the blowback behaviour of the bottom outlet of the Berg River Dam, South Africa." *Journal of the South African Institution of Civil Engineering*, 58(1), 43–52.

Botello-Álvarez, J. E., Baz-Rodríguez, S. A., González-García, R., Estrada-Baltazar, A., Padilla-Medina, J. A., González-Alatorre, G., and Navarrete-Bolaños, J. L. (2011). "Effect of electrolytes in aqueous solution on bubble size in gas-liquid bubble columns." *Industrial and Engineering Chemistry Research*, 50(21), 12203–12207.

Bruce, J, and Plate, E. 2013. Total Dissolved Gas Supersaturation Downstream of Hugh Keenleyside Dam: A Model-Based TGP Risk Assessment of Facility Operations That Reduce on Low Level Ports for Water Conveyance. Report Prepared for BC Hydro, Burnaby BC. Creekside Aquatic Sciences. Report No. CAQ-001:

Bruce, J., and Smith, J. (2016). *Fate Modeling of Air Supersaturated Waters in the Columbia River : Phase 1 – Model Development and Information Gap Analysis*. Robert Creek.

Calderbank, P. H., and Moo-Young, M. B. (1961). "The continuous phase heat and mass-transfer properties of dispersions." *Chemical Engineering Science*, 16, 39–54.

Campbell, F. B., and Guyton, B. (1953). "Air demand in gated outlet works." Proc., 5th IAHR and ASCE Joint Conf., 529–533.

Chanson, H. (1992). "Air entrainment in Chute and Tunnel Spillways." *11th Australasion Fluid Mechanics Conference*, Hobart, 83–86.

Chanson, H. (1993a). "Self-Aerated flows on Chutes and spillways." *Journal of Hydraulic*

*Engineering*, 120(6), 778–782.

Chanson, H. (1993b). "Stepped spillway flows and air entrainment." *Canada Journal of Civil Engineering*, 20, 422–435.

Chanson, H. (1995). "Air bubble diffusion in supercritical open channel flows." *Twelfth Austrilian Fluid Mechanics Conference*, Sydney, 707–710.

Chanson, H. (1996). *Air bubble entrainment in free-surface turbulent shear flows*. Academic Press, San Diego.

Chanson, H. (1997). "Air bubble entrainment in open channels: flow structure and bubble size distributions." *International Journal of Multiphase Flow*, 23(1), 193–203.

Chanson, H. (2004). "Air entrainment in hydraulic engineering." *Fluvial, Environmental and Coastal Developments in Hydraulic Engineering*, Bari, Italy, 17–64.

Chanson, H., Aoki, S., and Hoque, A. (2004). "Physical modelling and similitude of air bubble entrainment at vertical circular plunging jets." *Chemical Enginerring Science*, 59, 747–758.

Chanson, H., and Carosi, Æ. G. (2007). "Turbulent time and length scale measurements in high-velocity open channel flows." *Experiments in Fluids*, 42, 385–401.

Chanson, H., and Cummings, D. (1992). *Aeration of the ocean due to plunging breaking waves*. Brisbane.

Chanson, H., and Gualtieri, C. (2008). "Similitude and scale effects of air entrainment in hydraulic jumps." Journal of Hydraulic Research, 46(1), 35–44.

Chanson, H., and Toombes, L. (2003). "Energy Dissipation and Air Entrainment in Stepped

    Storm Waterway : Experimental Study." *Journal of Irrigation and Drainage Engineering*,

    128(5), 305–315.

Chapman, G. (1986). Ambient Water Quality Criteria for Dissolved Oxygen. U.S.

    Environmental Protection Agency, Office of Water, Washington DC.

Chen, P., Duduković, M. P., and Sanyal, J. (2005). "Three-dimensional simulation of bubble

    column flows with bubble coalescence and breakup." *AIChE Journal*, 51(3), 696–712.

Clift, R., Grace, J. R., and Weber, N. E. (1978). *Bubble, Drops, and Particles*. *Academic Press*,

    Academic Press, New York.

Colt, J. (2012). *Dissolved Gas Concentration in Water Computation as Functions of

    Temperature , Salinity and Pressure*. American Fisheries Society, Maryland.

Colt, J. (1984). Computation of dissolved gas concentrations in water as functions of

    temperature, salinity and pressure. American Fisheries Society Special Publication No. 14,

    Bethesda Maryland.

Chow, V. T. (1959). Open-Channel Hydraulics. New York, NY: McGraw Hill.

Dani, A., Guiraud, P., and Cockx, A. (2007). "Local measurement of oxygen transfer around a

    single bubble by planar laser-induced fluorescence." *Chemical Engineering Science*, 62(24),

    7245–7252.

Dawley, E. M., and Ebel, W. J. (1975). "Effects of various concentrations of dissolved

    atmospheric gas on juvenile chinook salmon and steelhead trout." *Fishey Bulletin*, 73(4),

787–796.

Deen, N. G., van Sint Annaland, M., and Kuipers, J. A. M. (2004). "Multi-scale modeling of dispersed gas-liquid two-phase flow." *Chemical Engineering Science*, 59(8), 1853–1861.

DeMoyer, C. D., Schierholz, E. L., Gulliver, J. S., and Wilhelms, S. C. (2003). "Impact of bubble and free surface oxygen transfer on diffused aeration systems." *Water Research*, 37(8), 1890–1904.

Drew, D. A., and Passman, S. L. (1999). *Theory of Multicomponent Fluids*. (J. E. Marsden and L. Sirovich, eds.), Springer-Verlag Berlin Heidelberg.

Dvorak, J. (2013). "Computational fluid dynamics (CFD) modeling to support the reduction of fish passage exposure to elevated total dissolved gas and predator habitats at McNary Dam." The University of Iowa.

Ebel, W. J. (1969). "Supersaturation of nitrogen in the columbia river and its effect on salmon and steelhead trout." *Fishery Bulletin*, 68(1), 1–11.

Edwini-Bonsu, S., and Steffler, P. M. (2004). "Air flow in sanitary sewer conduits due to wastewater drag: A computational fluid dynamics approach." J. Environ. Eng. Sci., 3(5), 331–342.

Ellingsen, K., and Risso, F. (2001). "On the rise of an ellipsoidal bubble in water: oscillatory paths and liquid-induced velocity ´." *J. Fluid Mech.*, 440, 235–268.

Epstein, P. S., and Plesset, M. S. (1950). "On the stability of gas bubbles in liquid-gas solutions." *Journal of Chemical Physics*, 18(11), 1505–1509.

Ervine, D. A., Falvey, H. T., Withers, W., and Lecturer, S. (1997). "Pressure fluctuations on plunge pool floors." *Journal of Hydraulic Research*, 35(2), 257–279.

Ervine, D. A., McKeogh, E., and Elsawy, E. M. (1980). "Effects of turbulence internsity on the rate of air entrainment by plunging water jets." *Proc. Instn Civ. Engrs*, 69(2), 425–445.

Escarameia, M. (2007). "Investigating hydraulic removal of air from water pipelines." *Proceedings of the Institution of Civil Engineers: Water Management*, 160(1), 25–34.

Falvey, H. (1980). *Air-water flow in hydraulic structure*. USBR Engrg. Monograph, No. 41, Denver, CO.

Fan, L., and Tsuchiya, K. (1990). *Bubble Wake Dynamics in Liquids and Liquid–Solid Suspensions*. *Bubble Wake Dynamics in Liquids and Liquid–Solid Suspensions*, Butterworth-Heinemann, Boston.

Felder, S., and Chanson, H. (2013). "Air – water flow measurements in a flat slope pooled stepped waterway." *Canadian Journal of Civil Engineering*, 40(4), 361–372.

Francois, J., Dietrich, N., Guiraud, P., and Cockx, A. (2011). "Direct measurement of mass transfer around a single bubble by micro-PLIFI." *Chemical Engineering Science*, 66(14), 3328–3338.

Geldert, D. A., Gulliver, J. S., and Wihelms, S. C. (1998). "Modeling dissolved gas supersaturation below spillway plunge pools." *Journal of Fluids Engineering*, 124(5), 513–521.

Gulliver, J. S., Hibbs, D. E., and McDonald, J. P. (1997). "Measurement of effective saturation

concentration for gas transfer." *Journal of Hydraulic Engineering*, 123(2), 86–97.

Gulliver, J., Thene, J., and Rindels, A. (1990). "Indexing gas transfer in self-aerated flows." *Journal of Environmental Engineering*, 116(3), 503–523.

Haberman, W. L., and Morton, R. K. (1953). *An experimental investigation of the drag and shape of air bubbles rising in various liquids*. Washington, D.C.

Hager, W. H. (1992). *Energy dissipators and hydraulic jump*. Kluwer Academic Publishers, Dordrecht, The Netherlands.

Hager, W. H. (2010). Wastewater hydraulics: Theory and practice. Springer, Berlin.

Hanyu, K., and Saito, T. (2010). "Dynamical mass-transfer process of a CO2 bubble measured by using LIF/HPTS visualisation and photoelectric probing." *Canadian Journal of Chemical Engineering*, 88(4), 551–560.

Harlow, F. (1985). "Well-Posed Two-Phase Flow Equations with Turbulence Transport." *Letter in Mathematical Physics*, 10, 161–166.

Hewitt, G.F., Hall-Taylor, N.S. (1970). Annular Two-Phase Flow. Pergamon Press Ltd., Oxford, UK.

Hibbs, D. E., and Gulliver, J. S. (1997). "Prediction of effective saturation concentration at spillway plunge pools." *Journal of Hydraulic Engineering*, 123(11), 940–949.

Hibiki, T., and Ishii, M. (2003). "One-dimensional drift-flux model and constitutive equations for relative motion between phases in various two-phase flow regimes." *International Journal of Heat and Mass Transfer*, 46(25), 4935–4948.

Higbie, R. 1935. "The rate of absorption of a pure gas into still liquid during short periods of exposure." Trans. Am. Inst. Chem. Eng. 31 (2): 365–390.

Hinze, J. (1955). "Fundamentals of the Hydrodynamic Mechanism of Splitting in Dispersion Processes." *AIChE Journal*, 1(3), 289–295.

Hohermuth, B., Schmocker, L., and Boes, R. M. (2020). "Air Demand of Low-Level Outlets for Large Dams." *Journal of Hydraulic Engineering*, 146(8), 1–11.

Hoschek, S. S., Carrica, P. M., and Weber, L. J. (2008). "Bubble Entrainment and Distribution in a Model Spillway with Application to Total Dissolved Gas Minimization." *Journal of Hydraulic Engineering*, 134(6), 763–771.

Huang, H. (2002). "Computational model of total dissolved gas downstream of a spillway." The University of Iowa.

Huang, W., Wu, C., and Xia, W. (2009). "Oxygen Transfer in High-Speed Surface Aeration Tank for Wastewater Treatment: Full-Scale Test and Numerical Modeling." *Journal of Environmental Engineering*, 135(8), 684–691.

Huang, X., Li, K., Li, R., Li, J., and Du, J. (2010). "Experimental system for the simulation of total dissovled gas supersaturated water of high dams." *Journal of Sichuan University*, 42(4), 25–28.

Ishii, M. (1977). *One-Dimensional Drift Flux Model and Constitutive Equations for Relative Motion Between Phases in Various Two-Phase Flow Regimes*. *Argone National Laboratory Anl-77-47*.

Ishii, M., and Zuber, N. (1979). "Drag coefficient and relative velocity in bubbly, droplet or particulate flows." *AIChE Journal*, 25(5), 843–855.

Jamialahmadi, M., C. Branch, and H. Muller-Steinhagen. 1994. "Terminal bubble rise velocity in liquids." Trans. Inst. Chem. Eng. 72 (Part A): 19–122.

Jimenez, M., Dietrich, N., Grace, J. R., and Hébrard, G. (2014). "Oxygen mass transfer and hydrodynamic behaviour in wastewater: Determination of local impact of surfactants by visualization techniques." *Water Research*, 58, 111–121.

Johnson, P. L., and King, D. L. (1975). "Prediction of dissolved gas at hydraulics structures." *Proc. Symp. Reaeration Res.*, ASCE, New York.

Kalinske, A. A., and Robertson, J. M. (1943). "Closed conduit flow." *Trans. ASCE 108*, 1435–1447.

Kamal, R., Li, P., and Billay, G. (2017). *TDG Monitoring in the Columbia River System : Field Study at the Brilliant , Seven Mile and Waneta Dams Department of Civil and Environmental Engineering October 2016*. Edmonton.

Kamal, R., Zhu, D. Z., Crossman, J. A., and Leake, A. (2020). "Case Study of Total Dissolved Gas Transfer and Degasification in a Prototype Ski-Jump Spillway." *Journal of Hydraulic Engineering*, 146(9), 1–10.

Kamal, R., Zhu, D. Z., Leake, A., and Crossman, J. (2018). "Decay of Supersaturated Total Dissolved Gases in the Intermediate Mixing." *World Environmental and Water Resources Congress*, 452–460.

Kamal, R., Zhu, D. Z., Leake, A., and Crossman, J. A. (2019). "Dissipation of Supersaturated Total Dissolved Gases in the Intermediate Mixing Zone of a Regulated River." *J. Environ. Eng.*, 145(2).

Khan, A. A., Gaur, R. Z., Lew, B., Mehrotra, I., and Kazmi, A. A. (2011). "Effect of aeration on the quality of effluent from UASB reactor treating sewage." *Journal of Environmental Engineering*, 137(6), 464–471.

Klohn-Crippen Integ. 1994. Total Gas Pressure (TGP) Reduction Study 1994 Status Report. Prepared for BC Hydro. Report No. KCI-173.

Koynov, A., Khinast, J. G., and Tryggvason, G. (2005). "Mass transfer and chemical reactions in bubble swarms with dynamic interfaces." *AIChE Journal*, 51(10), 2786–2800.

Kusabiraki, D., Murota, M., Ohno, S., Yamagiwa, K., Yasuda, M., and Ohkawa, A. (1990). "Gas entrainment rate and flow pattern in a plunging liquid jet aeration system using inclined nozzles." *Journal of Chemical Engineering of Japan*.

Lamont, J., and Scott, D. (1970). "Eddy Cell Model of Mass Transfer Into the Surface of a Turbulent Liquid." *AIChE Journal*, 16(4), 513–519.

Launder, B. E., and Spalding, D. B. (1974). "The numerical computation of turbulent flows." *Computer Methods in Applied Mechanics and Engineering*, 3(2), 269–289.

Li, P., Ma, Y., and Zhu, D. Z. (2020). "Mass Transfer of Gas Bubbles Rising in Stagnant Water." *Journal of Environmental Engineering*, 146(8), 1–11.

Li, P., Zhu, D. Z., Xu, T., and Zhang, J. (2021). "Air Demand of a Hydraulic Jump in a Closed

Conduit." *Journal of Hydraulic Engineering*, ASCE, Manuscript ID HYENG-12849, under review

Li, R., Li, J., Li, K. F., Deng, Y., and Feng, J. J. (2009). "Prediction for supersaturated total dissolved gas in high-dam hydropower projects." *Science in China, Series E: Technological Sciences*, 52(12), 3661–3667.

Li, R., Luo, L., Fu, X., and Huang, W. (2002). "Effect of hydrodynamic characteristics on reaeration process." *Journal of Environmental Sciences*, 04(3), 393–398.

Liu, L., Yan, H., and Zhao, G. (2015). "Experimental studies on the shape and motion of air bubbles in viscous liquids." *Experimental Thermal and Fluid Science*, 62, 109–121.

Lochiel, A. C., and Calderbank, P. H. (1964). "Mass transfer in the continuous phase around axisymmetric bodies of revolution." *Chemical Engineering Science*, 19(7), 471–484.

Long, D., Rajaratnam, N., Steffler, P. M., and Smy, P. R. (1991). "Structure of flow in hydraulic jumps." Journal of Hydraulic Research, 29(2), 207–218.

Longdoz, B., Yernaux, M., and Aubinet, M. (2000). "Soil CO2 efflux measurements in a mixed forest: Impact of chamber disturbances, spatial variability and seasonal evolution." *Global Change Biology*, 6(8), 907–917.

Lu, J., Li, R., Ma, Q., Feng, J., Xu, W., Zhang, F., and Tian, Z. (2019). "Model for Total Dissolved Gas Supersaturation from Plunging Jets in High Dams." Journal of Hydraulic Engineering, 145(1), 1–10.

St. Louis, V. L., Kelly, C. A., Duchemin, E., Rudd, J. W. M., and Rosenberg, D. M. (2000).

"Reservoir surfaces as sources of greenhouse gases to the atmosphere : A global estimate." *BioScience*, 50(9), 766–774.

Lu, J., Li, R., Ma, Q., Feng, J., Xu, W., Zhang, F., and Tian, Z. (2019). "Model for Total Dissolved Gas Supersaturation from Plunging Jets in High Dams." *Journal of Hydraulic Engineering*, 145(1), 1–10.

Ma, Q., Li, R., Zhang, Q., Hodges, B., Feng, Ji., and Yang, H. (2016). "Two phase flow simulation of supersaturated total dissolved gas in the pool of a high dam." *Environmental Progress & Sustainable Energy*, 35(4), 1139–1148.

Maneri, C. C., and Vassallo, P. F. (2000). *Dynamics of Bubbles Rising in Finite and Infinite Media*. Honolulu, Hawaii, USA.

Manninen, M., Taivassalo, V., and Kallio, S. (1996). *On the mixture model for multiphase flow*. *Vtt Publications*, Finland.

McGinnis, D. F., and Little, J. C. (1998). "Bubble dynamics and oxygen transfer in a Speece Cone." *Water Science and Technology*, 37(2), 285–292.

McGinnis, D. F., and Little, J. C. (2002). "Predicting diffused-bubble oxygen transfer rate using the discrete-bubble model." *Water Research*, 36(18), 4627–4635.

Meselhe, E. A., and Odgaard, A. J. (1998). "3D numerical flow model for fish diversion studies at Wanapum Dam." *Journal of Hydraulic Engineering*, 124(12), 1203–1214.

Mortensen, J. D., Barfuss, S. L., and Johnson, M. C. (2011). "Scale effects of air entrained by hydraulic jumps within closed conduits." Journal of Hydraulic Research, 49(1), 90–95.

Mortensen, J. D., Barfuss, S. L., and Tullis, B. P. (2012). "Effects of hydraulic jump location on air entrainment in closed conduits." *Journal of Hydraulic Research*, 50(3), 298–303.

Motarjemi, M., and Jameson, G. J. (1978). "Mass transfer from very small bubbles—the optimum bubble size for aeration." *Chem Eng Sci*, 33, 1415–1423.

Mott, R.L., 1994. Applied Fluid Mechanics, Fourth Edition. Prentice-Hall, Inc., Upper Saddle River, New Jersey.

Nakasone, H. (1987). "Study of Aeration at Weirs and Cascades." *Journal of Environmental Engineering*, 113(1), 64–81.

Nezu, I., and Nakagawa, H. (1993). *Turbulence in Open-Channel Flows*. A.A. Balkema Publishers, Rotterdam, Netherlands.

Nielsen, K. D., Weber, L., and Haug, P. E. (2000). *Hydraulic model study for fish diversion at Wanapum/Priest Rapids development*.

Nock, W. J. (2015). "An investigation into gas transfer from bubbles into water." Thesis for the degree of Doctor of Philosophy. University of Southampton.

Nock, W. J., Heaven, S., and Banks, C. J. (2016). "Mass transfer and gas-liquid interface properties of single CO2 bubbles rising in tap water." *Chemical Engineering Science*, 140, 171–178.

Orlins, J., and Gulliver, J. (2000). "Dissolved gas supersaturation downstream of a spillway II: Computational model." *Journal of Hydraulic Research Research*, 38(2), 151–159.

Ozkan, F., Tuna, M. C., Baylar, A., and Ozturk, M. (2014). "Optimum air-demand ratio for

maximum aeration efficiency in high-head gated circular conduits." *Water Science and Technology*, 70(5), 871–877.

Parker, W.J., Ryan, H., 2001. A Tracer Study of Headspace Ventilation in a Collector Sewer. J. Air Waste Manag. Assoc. 51 (4), 582–592.

Pescod, M.B., Price, A.C., 1982. Major factors in sewer ventilation. J. Water Pollut. Control Fed. 54 (4), 385–397.

Politano, M., Amado, A. A., and Anderson, K. (2014). "Numerical modelling of the hydrodynamics and total dissolved gas downstream of Hells Canyon Dam." *Australian Journal of Water Resources*, 18(2), 162–179.

Politano, M., Arenas Amado, A., Bickford, S., Murauskas, J., and Hay, D. (2011). "Investigation into the Total Dissolved Gas Dynamics of Wells Dam Using a Two-Phase Flow Model." *Journal of Hydraulic Engineering*, 137(10), 1257–1268.

Politano, M., Arenas Amado, A., Bickford, S., Murauskas, J., and Hay, D. (2012). "Evaluation of operational strategies to minimize gas supersaturation downstream of a dam." *Computers and Fluids*, 68, 168–185.

Politano, M., Carrica, P., and Weber, L. (2008). "A Multidimensional Anisotropic Two-Phase Flow Model to Predict Total Dissolved Gas in Wanapum Dam." *World Environmental and Water Resources Congress*, (1), 1–10.

Politano, M., Carrica, P., and Weber, L. (2009). "A multiphase model for the hydrodynamics and total dissolved gas in tailraces." *International Journal of Multiphase Flow*, 35(11), 1036–

1050.

Politano, M., Castro, A., and Hadjerioua, B. (2017). "Modeling Total Dissolved Gas for Optimal Operation of Multireservoir Systems." *Journal of Hydraulic Engineering*, 143(6), 1–12.

Politano, M. S., Carrica, P. M., Turan, C., and Weber, L. (2007). "A multidimensional two-phase flow model for the total dissolved gas downstream of spillways." *Journal of Hydraulic Research*, 45(2), 165–177.

Potter, M. C., and Wiggert, D. C. (2016). Mechanics of Fluids, 4th edn. Prentice Hall, Boston, MA, USA.

Qian, Y., Shao, W., Zhu, D. Z., Mohamad, K. A. A., Steffler, P. M., Edwini-Bonsu, S., Yue, D., and Krywiak, D. (2020). "Modeling air flow in sanitary sewer systems: A review." *Journal of Hydro-Environment Research*.

Qian, Y., Zhu, D. Z., Zhang, W., Rajaratnam, N., Edwini-Bonsu, S., and Steffler, P. (2017). "Air movement induced by water flow with a hydraulic jump in changing slope pipes." *Journal of Hydraulic Engineering*, 143(4), 1–11.

Qu, L., Li, R., Li, J., Li, K., and Deng, Y. (2011). "Field observation of total dissolved gas supersaturation of high-dams." Science China Technological Sciences, 54(1), 156–162.

Rabben, S. L., H. Els, and G. Rouve. 1983. "Investigations on flow aeration at offsets downstream of high-head control structures." In Vol. 4 of Proc., 20th IAHR Congress, 354–360. USSR: Moscow.

Ramos, P. X., Schindfessel, L., Pêgo, J. P., and Mulder, T. De. (2019). "Flat vs. Curved rigid-lid

LES computations of an open-channel confluence." Journal of Hydroinformatics, 21(2), 318–334.

Rajaratnam, N. (1967). *Hydraulic Jumps. Advances in Hydroscience.*

Rajaratnam, N. (1976). *TurbuLent Jets*. Elsevier Scientific Publ. Co., Development in Water Science, New York, USA.

Roesner, L., and Norton, W. (1971). *A Nitrogen Gas Model for the Lower Columbia River, Final Report. North Pacific Division, U. S. Army Corps of Engineers*, Portland.

Sakhuja, V. S., T. C. Paul, and S. Singh. (1984). "Air entrainment distortion in free surface flows." In Proc., Int. Symp. on Scale Effects in Modelling Hydraulic Structures, 4.8.1–4.8.4. Esslingen, Germany: IAHR.

Sam, A., Gomez, C. O., and Finch, J. A. (1996). "Axial velocity profiles of single bubbles in water/frother solutions." *International Journal of Mineral Processing*, 47, 177–196.

Schierholz, E. L., Gulliver, J. S., Wilhelms, S. C., and Henneman, H. E. (2006). "Gas transfer from air diffusers." *Water Research*, 40(5), 1018–1026.

Schulz, H. E., Vasconcelos, J. G., Asce, M., and Patrick, A. C. (2020). "Air Entrainment in Pipe-Filling Bores and Pressurization Interfaces." *J. Hydraul. Eng.*, 146(2), 1–12.

Schulze, G., and Schlünder, E. U. (1985). "The effect of multicomponent diffusion on the mass transfer during absorption of single gas bubbles." *Chemical Engineering and Processing*, 19(5), 257–265.

Sene, K. J. (1988). "Air entrainment by Plunging jets." *Chemical Enginerring Science*, 43(10),

2615–2623.

Sharma, H. R. (1976). "Air-entrainment in high head gated conduits." *Journal of the Hydraulics Division*, 11, 1629–1646.

Shew, W. L., and Pinton, J.-F. (2006). "Dynamical Model of Bubble Path Instability." *Physical Review Letters*, 97, 6–9.

Singleton, V. L., Gantzer, P., and Little, J. C. (2007). "Linear bubble plume model for hypolimnetic oxygenation : Full-scale validation and sensitivity analysis." *Water Resources Research*, 43, 1–12.

Skartlien, R., Julshamn, J. A., Lawrence, C. J., and Liu, L. (2012). "A gas entrainment model for hydraulic jumps in near horizontal pipes." *International Journal of Multiphase Flow*, 43, 39–55.

Smiley, J. E., Drawbridge, M. A., Okihiro, M. S., and Kaufmann, R. S. (2011). "Transactions of the American Fisheries Society Acute Effects of Gas Supersaturation on Juvenile Cultured White Seabass Acute Effects of Gas Supersaturation on Juvenile Cultured." *Transactions of the American Fisheries Society*, 140, 1269–1276.

Stahl, H., and Hager, W. H. (1999). "Hydraulic jump in circular pipes." *Can. J. Civ. Eng.*, 26, 368–373.

Stefan, H. G., and Fang, X. (1994). "Dissolved oxygen model for regional lake analysis." Ecological Modelling, 71(1–3), 37–68.

Stöhr, M., Schanze, J., and Khalili, A. (2009). "Visualization of gas-liquid mass transfer and

wake structure of rising bubbles using pH-sensitive PLIF." *Experiments in Fluids*, 47(1), 135–143.

Takahashi, M., and Ohtsu, I. (2017). "Effects of inflows on air entrainment in hydraulic jumps below a gate." *Journal of Hydraulic Research*, 55(2), 259–268.

Takemura, F., and Yabe, A. (1998). "Gas dissolution process of spherical rising gas bubbles." *Chemical Engineering Science*, 53(15), 2691–2699.

Takemura, F., and Yabe, A. (1999). "Rising speed and dissolution rate of a carbon dioxide bubble in slightly contaminated water." *Journal of Fluid Mechanics*, 378, 319–334.

Thomas, J. A., Funk, W. H., Moore, B. C., and Budd, W. W. (1994). "Short term changes in Newman Lake following hypolimnetic aeration with the speece cone." *Lake and Reservoir Management*, 9(1), 111–113.

Tomiyama, A. (1998). "Struggle with computational bubble dynamics." *Multiphase Science and Technology*, 10, 369–405.

Toombes, L., and Chanson, H. (2005). "Air–Water Mass Transfer on a Stepped Waterway." *Journal of Environmental Engineering*, 131(10), 1377–1386.

Tripathi, M. K., Sahu, K. C., and Govindarajan, R. (2015). "Dynamics of an initially spherical bubble rising in quiescent liquid." *Nature Communications*, 6, 1–9.

Tsuge, H., and Hibino, S. (1971). "The motion of single gas bubbles rising in various liquids." *Kagaku Kogaku*, 35(65), 65–71.

Tullis, B. P., and Larchar, J. A. (2011). "Determining Air Demand for Small to Medium-Sized

Embankment Dam Low-Level Outlet Works." *Journal of Irrigation and Drainage Engineering*, 137(12), 793–800.

Tzvi, Y., and Y. Paz. 2019. "Highly efficient method for oxidation of dissolved hydrogen sulfide in water, utilizing a combination of UVC light and dissolved oxygen." J. Photochem. Photobiol., A 372 (Mar): 63–70.

Unsal, M., Baylar, A., Tugal, M., and Ozkan, F. (2008). "Increased aeration efficiency of high-head conduit flow systems." *Journal of Hydraulic Research*, 46(5), 711–714.

Urban, A. L., Gulliver, J. S., and Johnson, D. W. (2008). "Modeling total dissolved gas concentration downstream of spillways." *Journal of Hydraulic Engineering*, 134(5), 550–561.

USACE (United States Army Corps of Engineers). (1980). *Hydraulic design of reservoir outlet structures*. Washington, DC.

USEPA. (1986). *Quality criteria for water*. Washington, D.C.

Valero, D., and Bung, D. B. (2016). "Development of the interfacial air layer in the non-aerated region of high-velocity spillway flows. Instabilities growth, entrapped air and influence on the self-aeration onset." International Journal of Multiphase Flow, 84, 66–74.

Volkart, P. (1980). "The mechanism of air bubble entrainment in self-aerated flow." *International Journal of Multiphase Flow*, 6, 411–423.

Vos, A. (2011). "Unsteady Flow Conditions At Dam Bottom Outlet Works Due To Air Entrainment During Gate Closure : Berg River." University of Stellenbosch.

Wang, Y., Politano, M., and Weber, L. (2019). "Spillway jet regime and total dissolved gas prediction with a multiphase flow model." *Journal of Hydraulic Research*, 57(1), 26–38.

Weber, L., Huang, H., Lai, Y., and McCoy, A. (2004). "Modeling total dissolved gas production and transport downstream of spillways: Three-dimensional development and applications." *International Journal of River Basin Management*, 2(3), 157–167.

Weitkamp, D. E. (2008). *Total dissolved gas supersaturation biological effects , review of literature 1980-2007*. *Parametrix*, Washington.

Weitkamp, D. E., and Katz, M. (1980). "A Review of Dissolved Gas Supersaturation Literature." *Transactions of the American Fisheries Society*, 109(6), 659–702.

Wilhelms, S. C., and S. K. Martin. 1992. "Gas transfer in diffused bubble plumes." In Hydraulic engineering: Saving a threatened resource in search of solutions, edited by S. M. Jenning and N. G. Bhowmilk. New York: ASCE.

Wilhelms, S. C., Gulliver, J. S., Ling, J. T., and Ling, R. S. (2005). "Gas transfer, cavitation, and bulking in self-aerated spillway flow." *Journal of Hydraulic Research*, 43(5), 532–539.

Wisner, P. 1967. "Hydraulic design for flood control by high head gated outlets." In Proc., 9th ICOLD Congress, 495–507. Paris: International Commission on Large Dams.

Wisner, P. E., F. N. Mohsen, and N. Kouwen. (1975). "Removal of air from water lines by hydraulic means." J. Hydraul. Div. 101 (HY2): 243–257.

Wood, I. R. (1997). "Air bubble entrainment in free surface turbulent shear flows by hubert chanson." *Journal of Hydraulic Engineering*, Academic Press, UK, 123(12), 1176–1176.

Wright, N. W., and B. P. Tullis. (2014). "Prototype and laboratory low-level outlet air demand comparison for small to medium-sized embankment dams." *J. Irrig. Drain. Eng.* 140 (6): 04014013

Wunderlich, W. 1963. "Die Grundablässe an Talsperren, Teil 2 (Bottom outlets of dams, Part 2)." Wasserwirtschaft 53 (4): 106–114.

Xu, W., Liao, H., Yang, Y. Q., and Wu, C. (2002). "Turbulent flow and energy dissipation in plunge pool of high arch dam." *Journal of Hydraulic Research*, 40(4), 471–476.